



NATIONAL ADVISORY COMMITTEE FOR AERONAUTICS

TECHNICAL NOTE 4178

LOW-SPEED CASCADE INVESTIGATION OF COMPRESSOR BLADES
HAVING LOADED LEADING EDGES

By James C. Emery

Langley Aeronautical Laboratory
Langley Field, Va.



Washington

January 1958

AFMDC

TECHNICAL LIBRARY
JAN 23 1958

10517
NACA TN 4178



TECHNICAL NOTE 4178

LOW-SPEED CASCADE INVESTIGATION OF COMPRESSOR BLADES

HAVING LOADED LEADING EDGES¹

By James C. Emery

SUMMARY

Six-percent-thick NACA 63-series compressor-blade sections having a loaded-leading-edge A_4K_6 mean line have been investigated systematically in a two-dimensional porous-wall cascade over a range of Reynolds number from 160,000 to 385,000. Blades cambered to have isolated-airfoil lift coefficients of 0.6, 1.2, 1.8, and 2.4 were tested over the usable angle-of-attack range at inlet-air angles of 30° , 45° , and 60° and solidities of 1.0 and 1.5.

A comparison with data of NACA Technical Note 3916 shows that the angle-of-attack operating range is 2° to 6° less than the range for the uniformly loaded section; however, the wake losses near design angle of attack are slightly lower than those for the uniformly loaded section. Except for highly cambered blades at high inlet angles, the NACA 63- $(C_{l_0}A_4K_6)06$ compressor-blade sections are capable of more efficient operation for moderate-speed subsonic compressors at design angle of attack than are the NACA 65- $(C_{l_0}A_{10})10$ or the NACA 65- $(C_{l_0}A_{2I8b})10$ compressor-blade sections, where C_{l_0} in the designation is the design lift coefficient of the isolated airfoil. In contrast with the other sections, the loaded-leading-edge sections are capable of operating efficiently at the lower Reynolds numbers.

INTRODUCTION

Systematic low-speed cascade data for the NACA 65-series compressor-blade sections are presented in reference 1 for a wide range of cascade configurations. These data, however, are limited to the uniformly loaded mean line. In high-speed compressors, blade mean lines other than those

¹Supersedes recently declassified NACA Research Memorandum L55J05, "Low-Speed Cascade Investigation of Loaded Leading-Edge Compressor Blades," by James C. Emery, 1956.

for uniform load are of interest. Reference 2 presents the results of a systematic variation in mean-line loading for NACA 65-series compressor-blade sections having the A_6I_{4b} and A_2I_{8b} mean lines, which shift the loading toward the trailing edge, and the A_6I_4 mean line which shifts the loading toward the leading edge. Additional data for a loaded-leading-edge mean line A_4K_6 were obtained in an investigation to develop a series of 6-percent-thick guide-vane profiles (ref. 3) suitable for operation at high inlet Mach numbers. This consideration led to a departure from the NACA 65-series thickness distribution to the NACA 63-series thickness distribution which has a more forward location of maximum thickness. At the same time, the thickness was reduced from 10 to 6 percent. This combination of mean-line loading, thickness distribution, and thickness provided favorable blade-passage-area distributions for high-speed compressors where choking of the flow in the guide-vane passages was a possibility. The results of reference 3 are limited to an inlet-air angle of 0° .

Some exploratory tests of the guide-vane blade sections at inlet-air angles in the range of interest for compressors showed high turning and low drag. The purpose of this paper is to present data obtained in tests of the 6-percent-thick NACA 63-series with A_4K_6 mean-line loading at inlet-air angles of 30° , 45° , and 60° , each at solidities of 1.0 and 1.5 in the low-speed porous-wall cascade. Carpet plots of the 63- $(C_{l_0}A_4K_6)06$ data and comparisons of these data with data for the 65- $(12A_2I_{8b})10$ and 65- $(12A_{10})10$ profiles are included.

SYMBOLS

c	blade chord, ft
C_{d_1}	section drag coefficient based on upstream dynamic pressure
C_{l_1}	section lift coefficient based on upstream dynamic pressure
C_{l_0}	camber, expressed as design lift coefficient of isolated airfoil
C_{w_1}	wake momentum-difference coefficient based on upstream dynamic pressure
L/D	lift-drag ratio
P	total pressure
p	static pressure

q	dynamic pressure
R	Reynolds number based on blade chord and entering velocity
S	pressure coefficient, $\frac{P - p_l}{q_l}$
α	angle between the inlet flow and the blade chord, deg
β	inlet-air angle, angle between the inlet-flow direction and the perpendicular to the cascade, deg
θ	flow turning angle, deg
σ	solidity, chord of blades divided by tangential spacing
P_R	resultant pressure coefficient; difference between local upper- and lower-surface pressure coefficients
$\frac{A_T}{A_1}$	ratio of blade-passage throat area to area of upstream flow
x	chordwise distance from blade leading edge, percent chord
y	blade thickness coordinate, percent chord
t	maximum thickness
Subscripts:	
d	design, when used with blades
l	local
1	upstream

APPARATUS, TEST PROGRAM, AND PROCEDURE

Description of Test Equipment

The test apparatus used in this investigation was the Langley 10-inch low-speed porous-wall cascade (fig. 1) described in reference 4 which was modified by reducing the test-section width from 20 inches to 10 inches. Five-inch-chord blades were used to give an aspect ratio of 2.0. Seven blades were used in the cascade except at the inlet-air angle of 30° and

solidity of 1.0 for which only five blades could be fitted into the tunnel. The side walls in the entrance to the test section contained a flush-type boundary-layer suction slot 1 chord length upstream from the blade sections being tested. In all tests a screen of 1/2-inch mesh hardware cloth was inserted at the entrance to the test section. This screen was inserted in order to increase the turbulence level of the entering air in an attempt to reduce the laminar separation on the test airfoils. The addition of the above screen made the turbulence level comparable to that of the Langley 5-inch cascade (refs. 1, 2, 4, and 5). Data from the two cascades may be compared directly without consideration of the effects of turbulence.

Description of Airfoils

The compressor blades used in this investigation were NACA 63-series airfoils of 6 percent thickness. The blade sections used were the 63-(6A₄K₆)06, 63-(12A₄K₆)06, 63-(18A₄K₆)06, and 63-(24A₄K₆)06 sections, for which the profiles are shown in figure 2. The part of the designation of these sections within parentheses follows a system used explicitly for compressor and turbine profiles. In this system the number within parentheses represents the design lift coefficient C_{l_0} in tenths. The letters A to K are identified with the mean lines $a = 1.0$ to $a = 0$ for each increment of 0.1, and the subscripts indicate the fraction (in tenths) of the lift coefficient associated with the particular mean line. The mean line and thickness distribution of this family are the same as those of reference 3. The A₄K₆ mean line of the present series avoids the reflex curvature near the trailing edge which is characteristic of the $a = 0$ mean line. The coordinates for this mean line for $C_{l_0} = 1.0$ are given in table I. The coordinates for the thickness distribution used (NACA 63-006 airfoil) are given in table II and the chordwise loading distribution is shown in figure 3.

Choking in blade rows is determined by the minimum passage or throat area. By laying out large-scale drawings of the blade passages for the A₄K₆ blades at design angle of attack for various combinations of inlet-air angle, solidity, and camber, the ratio of minimum passage area A_T to inlet area A_1 could be measured. Figure 4 presents A_T/A_1 plotted against inlet-air angle for solidities of 1.0 and 1.5 and cambers of 0.6, 1.2, 1.8, and 2.4 for the A₄K₆ blade section. In addition, A_T/A_1 for the A₁₀ blade section ($C_{l_0} = 1.2$) is given for comparison. It is apparent that shifting the loading to the leading edge has very little effect on the area ratio below an inlet angle of 40°. Above 40° the A₄K₆ sections increase in passage area faster than the A₁₀ sections; hence, the A₄K₆ sections are equal to A₁₀ sections in area ratio up to 40° and are more open at higher inlet-air angles.

Test Program and Procedure

Test program.- The combinations of inlet-air angle, solidity, and blade section for which data are presented are shown in the following table:

σ	β , deg		
	30	45	60
1.0	63-(6A ₄ K ₆)06	63-(6A ₄ K ₆)06	63-(6A ₄ K ₆)06
	63-(12A ₄ K ₆)06	63-(12A ₄ K ₆)06	63-(12A ₄ K ₆)06
	63-(18A ₄ K ₆)06	63-(18A ₄ K ₆)06	*
	63-(24A ₄ K ₆)06	63-(24A ₄ K ₆)06	*
1.5	63-(6A ₄ K ₆)06	63-(6A ₄ K ₆)06	63-(6A ₄ K ₆)06
	63-(12A ₄ K ₆)06	63-(12A ₄ K ₆)06	63-(12A ₄ K ₆)06
	63-(18A ₄ K ₆)06	63-(18A ₄ K ₆)06	*
	63-(24A ₄ K ₆)06	63-(24A ₄ K ₆)06	*

*Stall occurred before design angle of attack.

The test program for the A₄K₆ blades was planned to provide sufficient information to satisfy conventional compressor-velocity diagrams when these data are used in conjunction with the A₁₀ data presented in reference 2.

Test procedure.- The porous-wall test procedure described in reference 4 was followed throughout this investigation. The tests covered the angle-of-attack range in 3° increments from negative to positive stall where stall was determined by a large increase in wake size (twice minimum).

It was not practical to maintain the same entering velocity for all the tests because of the large variation in pressure ratio across the various cascades and the changes in upstream area. Therefore, the tests were run at near maximum output of the tunnel drive motor and the resultant Reynolds number based on the upstream velocity and the 5-inch chord varied from 297,000 to 346,000. Two cascade combinations were

tested at design angle of attack over a range of Reynolds number from 160,000 to 385,000 to assist in estimating performance at Reynolds numbers other than the usual test value.

Test measurements.- Blade pressure distributions, turning-angle surveys, and wake total-pressure loss were obtained by using the methods of reference 1. Upstream conditions were measured in the same manner as in reference 3.

Calculations.- The calculative procedure is completely described in reference 1. Brief definitions of wake, lift, and drag coefficient are repeated herein. The wake coefficient C_{w1} represents the momentum difference between the wake and the stream outside of the wake. All forces due to pressure and momentum changes across the blade row were summed to obtain the resultant blade-force coefficient. The resultant force coefficient was resolved into components perpendicular and parallel to the vector mean velocity to obtain the lift coefficient C_{l1} and the drag coefficient C_{d1} , respectively. All coefficients are based on the upstream dynamic pressure q_1 .

Accuracy of Results

The measured turning-angle accuracy was within $\pm 0.5^\circ$ near the design condition. For tests near positive or negative stall the accuracy was somewhat reduced because of increased wake widths in the plane of angle measurement.

The blade normal-force coefficient calculated from pressure-rise and momentum considerations was compared with the normal-force coefficient obtained by integration of the pressure distribution. Since these values would be affected by errors in turning angle, surface pressure, wake-survey readings, or a failure to achieve two dimensionality of the flow, this comparison is a check of the overall acceptability of the tests. The agreement between normal-force coefficients obtained by the aforementioned methods was within 5 percent. The lift coefficients presented were obtained from momentum considerations.

Presentation of Results

The coordinates for the $A_{14}K_6$ mean line are presented in table I, and the thickness-distribution coordinates for the NACA 63-006 airfoil with trailing edge thickened ($t/c = 6$ percent) are presented in table II. The results for the various blade sections tested are presented in figures 4 to 43, as indexed in the following table:

PRESENTATION OF RESULTS

Figure	NACA blade sections	Legend	Solidity	Inlet-air angle
Figure 4	63-(6A ₄ K ₆)06 63-(12A ₄ K ₆)06 63-(18A ₄ K ₆)06 63-(24A ₄ K ₆)06 65-(12A ₁₀)06	Ratio of blade-passage throat area to area of upstream flow at α_d	1.0 and 1.5	0° to 60°
Figures 5 to 24	63-(C ₁₀ A ₄ K ₆)06	Detailed blade performance and summary plots	1.0 and 1.5	30°, 45°, and 60°
Figures 25 to 30	63-(6A ₄ K ₆)06 63-(12A ₄ K ₆)06 63-(18A ₄ K ₆)06 63-(24A ₄ K ₆)06	Summary of turning-angle θ and angle-of-attack α relationship	1.0 and 1.5	30°, 45°, and 60°
Figures 31 to 32	63-(C ₁₀ A ₄ K ₆)06 65-(C ₁₀ A ₁₀)10	Variation of estimated operating angle-of-attack range with inlet-air angle for several cambers	1.0 and 1.5	30°, 45°, and 60°
Figure 33	63-(C ₁₀ A ₄ K ₆)06 65-(C ₁₀ A ₁₀)10	Difference in α_d and θ_d for two cambers	1.0 and 1.5	30°, 45°, and 60°
Figure 34	63-(12A ₄ K ₆)06	Blade-surface pressure distributions for Reynolds number range from 159,000 to 385,000	1.5	45°
Figure 35	63-(12A ₄ K ₆)06	Summary plot of R effect on section characteristics	1.5	45°
Figure 36	63-(12A ₄ K ₆)06	Blade-surface pressure distributions for Reynolds number range from 159,000 to 385,000	1.0	60°
Figure 37	63-(12A ₄ K ₆)06	Summary plot of R effect on section characteristics	1.0	60°
Figure 38	63-(12A ₄ K ₆)06 65-(12A ₁₀ I _{8B})10 65-(12A ₁₀)10	Variation of $\theta - \theta_{\max}$ and C_{d1} with R at α_d	1.0	60°
Figure 39	63-(12A ₄ K ₆)06 65-(12A ₁₀ I _{8B})10 65-(12A ₁₀)10	Variation of L/D with R at α_d	1.0	60°
Figure 40	63-(12A ₄ K ₆)06 65-(12A ₁₀)10	Variation of $\theta - \theta_{\max}$ and C_{d1} with R at α_d	1.5	45°
Figure 41	63-(12A ₄ K ₆)06 65-(12A ₁₀)10	Variation of L/D with R at α_d	1.5	45°
Figure 42	63-(C ₁₀ A ₄ K ₆)06	Design α carpet plot	1.0 and 1.5	0° to 60°
Figure 43	63-(C ₁₀ A ₄ K ₆)06	Design θ carpet plot	1.0 and 1.5	0° to 60°

DISCUSSION OF RESULTS

Operating Range

Summaries of the turning angle, angle-of-attack relationships for the four cambered blade sections tested are given for each inlet angle and solidity in figures 25 to 30. For combinations giving moderate pressure rises there are straight-line relationships for considerable portions of the curves. At the highest pressure-rise combinations ($\beta = 60^\circ$) the two-dimensional pressure rise is very near the stalling pressure rise and the straight-line relationship exists for only a small portion of the curve.

In order to select the upper and lower limits of angle of attack, Howell's index of twice minimum drag (ref. 6) was used to estimate the useful operating range of the various sections at the solidity and inlet-angle conditions tested. In figures 31 and 32 a comparison of the operating range of the 63- $(C_{l_0}A_{t_0}K_6)06$ blade sections with that of the 65- $(C_{l_0}A_{t_0})10$ blade sections of reference 1 indicates a 2° to 6° greater range for the 65- $(C_{l_0}A_{t_0})10$ sections for the conditions tested. The smaller operating range of the 63- $(C_{l_0}A_{t_0}K_6)06$ sections is attributed to the difference in profile thickness (ref. 5). In addition to the effect of profile thickness, the loaded leading edge of the 63- $(C_{l_0}A_{t_0}K_6)06$ sections has a steeper pressure gradient near the leading edge which tends to form a thick boundary layer on the convex surface; consequently, a reduction in operating range is to be expected.

Turning Angle

In figure 33 a comparison of the 63- $(C_{l_0}A_{t_0}K_6)06$ and 65- $(C_{l_0}A_{t_0})10$ blade sections is presented to show the differences in design angle of attack and turning angle for these two different sections. In general, the difference is of the order of 1° for the design turning angle. The difference in the design angle of attack is 3.9° for the 65- $(24A_{t_0}K_6)06$ blade sections and decreases linearly with camber. It can be seen that at the three inlet-air angles (at design angle of attack) the difference between the turning angles for the two types of loading is small.

Reynolds Number Effects

As shown in figures 35 and 37 the drag coefficient and turning angle remain almost constant above a Reynolds number of 220,000.

Figures 34 and 36 indicate no significant change in the pressure distribution over the range of Reynolds number tested.

Figures 38 and 40 show the variation of θ and C_{d1} at α_d with Reynolds number for the 63-(12A₄K₆)06, 65-(12A₂I_{8b})10, and the 65-(12A₁₀)10 blade sections at β of 60° and 45°, σ of 1.0 and 1.5. The A₂I_{8b} section is not included in the lower inlet-angle figure because no data were available for that condition. The A₄K₆ section has a lower critical Reynolds number than the A₂I_{8b} or the A₁₀ sections as indicated by the lower drag and higher turning angle at the lower end of the Reynolds number range. This is to be expected because of the adverse pressure gradient beginning at the leading edge of the A₄K₆ section.

The variation of the lift-drag ratio with Reynolds number for the 63-(12A₄K₆)06, 65-(12A₁₀)10 and the 65-(12A₂I_{8b})10 blade section is presented in figures 39 and 41 for inlet angles of 60° and 45° and solidities of 1.0 and 1.5. The lift-drag ratios for the A₄K₆ section are generally higher than the values for the A₁₀ section. Some variation occurred in the curves of wake and drag coefficients plotted against Reynolds number because of the sudden changes in the nature of the boundary-layer flow for both sections; therefore, the drag coefficient and lift-drag ratio are not sufficiently reliable to use directly in a compressor-performance analysis. However, these values should be of some use for comparative purposes. An evaluation based on lift-drag ratio indicates that the 63-(C_{l0}A₄K₆)06 blade sections would operate more efficiently than the 65-(C_{l0}A₁₀)10 or 65-(C_{l0}A₂I_{8b})10 sections in a compressor up to critical speed. It should be noted, however, that the critical speed of these loaded-leading-edge sections will be lower than that of the uniformly loaded or the loaded-trailing-edge sections.

Carpet Plots

In order to facilitate the selection of blade camber and design angle of attack to fulfill a design vector diagram, a carpet plot of blade camber as a function of inlet-air angle, turning angle, and solidity is presented in figure 43. Design angle of attack may be obtained from figure 42 which is a carpet plot of design angle of attack as a function of solidity and camber. The design angle of attack was found to be independent of inlet-air angle. A complete discussion of carpet plots and the method of interpolation of intermediate values is given in reference 7.

SUMMARY OF RESULTS

The NACA 63- $(C_{l_0}A_4K_6)$ 06 compressor-blade sections (where C_{l_0} is the design lift coefficient of the isolated airfoil) were designed with relatively straight trailing edges, low maximum thickness, and high aerodynamic loading in the leading-edge region. Comparison of the results of low-speed cascade tests of these sections with those of uniformly loaded or loaded-trailing-edge sections indicates the following characteristics:

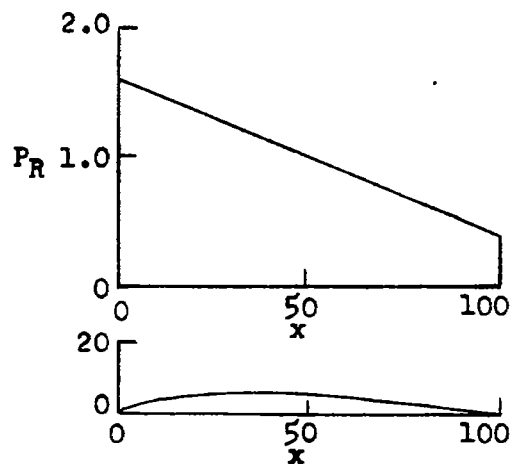
1. Wake losses for the loaded-leading-edge sections near design angle of attack are slightly lower than are those for uniformly loaded or loaded-trailing-edge sections.
2. The angle-of-attack operating range for the loaded-leading-edge sections is 2° to 6° less than the range for the uniformly loaded sections.
3. In contrast with the other blade sections, the loaded-leading-edge sections are capable of operating efficiently at the lower Reynolds numbers.
4. Except for highly cambered blades at high inlet angles, the NACA 63- $(C_{l_0}A_4A_6)$ 06 compressor-blade sections are capable of more efficient operation for moderate-speed subsonic compressors at design angle of attack than are the NACA 65- $(C_{l_0}A_{10})$ 10 or the NACA 65- $(C_{l_0}A_2I_8b)$ 10 compressor-blade sections.

REFERENCES

1. Herrig, L. Joseph, Emery, James C., and Erwin, John R.: Systematic Two-Dimensional Cascade Tests of NACA 65-Series Compressor Blades at Low Speeds. NACA TN 3916, 1957. (Supersedes NACA RM L51G31.)
2. Erwin, John R., Savage, Melvyn, and Emery, James C.: Two-Dimensional Low-Speed Cascade Investigation of NACA Compressor Blade Sections Having a Systematic Variation in Mean-Line Loading. NACA TN 3817, 1956. (Supersedes NACA RM L53I30b.)
3. Dunavant, James C.: Cascade Investigation of a Related Series of 6-Percent-Thick Guide-Vane Profiles and Design Charts. NACA TN 3959, 1957. (Supersedes NACA RM L54I02.)
4. Erwin, John R., and Emery, James C.: Effect of Tunnel Configuration and Testing Technique on Cascade Performance. NACA Rep. 1016, 1951. (Supersedes NACA TN 2028.)
5. Herrig, L. Joseph, Emery, James C., and Erwin, John R.: Effect of Section Thickness and Trailing-Edge Radius on the Performance of NACA 65-Series Compressor Blades in Cascade at Low Speeds. NACA RM L51J16, 1951.
6. Howell, A. R.: Design of Axial Compressors. Lectures on the Development of the British Gas Turbine Jet Unit Published in War Emergency Issue No. 12 of the Institution of Mechanical Engineers. A.S.M.E. Reprint, Jan. 1947, pp. 452-462.
7. Felix, A. Richard: Summary of 65-Series Compressor-Blade Low-Speed Cascade Data by Use of the Carpet-Plotting Technique. NACA TN 3913, 1957. (Supersedes NACA RM L54H18a.)

TABLE I.- COORDINATES FOR A_4K_6 MEAN LINE

$$[c_{l_0} = 1.0]$$

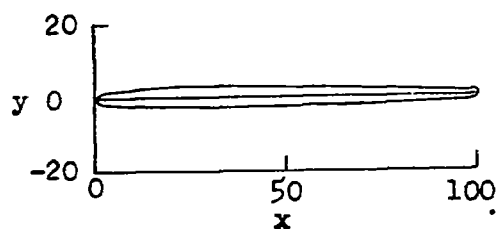


x	y	dy/dx
0	0	-----
.5	.376	0.6237
1.25	.792	.5034
2.5	1.357	.4100
5.0	2.248	.3131
10	3.531	.2110
15	4.420	.1483
20	5.040	.1023
25	5.458	.0659
30	5.710	.0359
35	5.824	.0104
40	5.820	-.0116
45	5.713	-.0308
50	5.516	-.0478
55	5.239	-.0628
60	4.891	-.0761
65	4.479	-.0881
70	4.011	-.0990
75	3.492	-.1090
80	2.922	-.1184
85	2.308	-.1278
90	1.642	-.1387
95	.912	-.1555
100	0	-----

TABLE II.-- THICKNESS-DISTRIBUTION COORDINATES FOR NACA 63-006

AIRFOIL WITH TRAILING EDGE THICKENED ($t/c = 6$ PERCENT)

[Stations and ordinates given in percent of chord]



x	±y
0	0
1.25	.771
2.5	1.057
5.0	1.462
10	2.010
15	2.386
20	2.656
25	2.841
30	2.954
35	3.000
40	2.971
45	2.877
50	2.723
55	2.517
60	2.301
65	2.085
70	1.870
75	1.654
80	1.438
85	1.222
90	1.007
95	.791
100	0
L. E. radius: 0.297	
T. E. radius: 0.6	

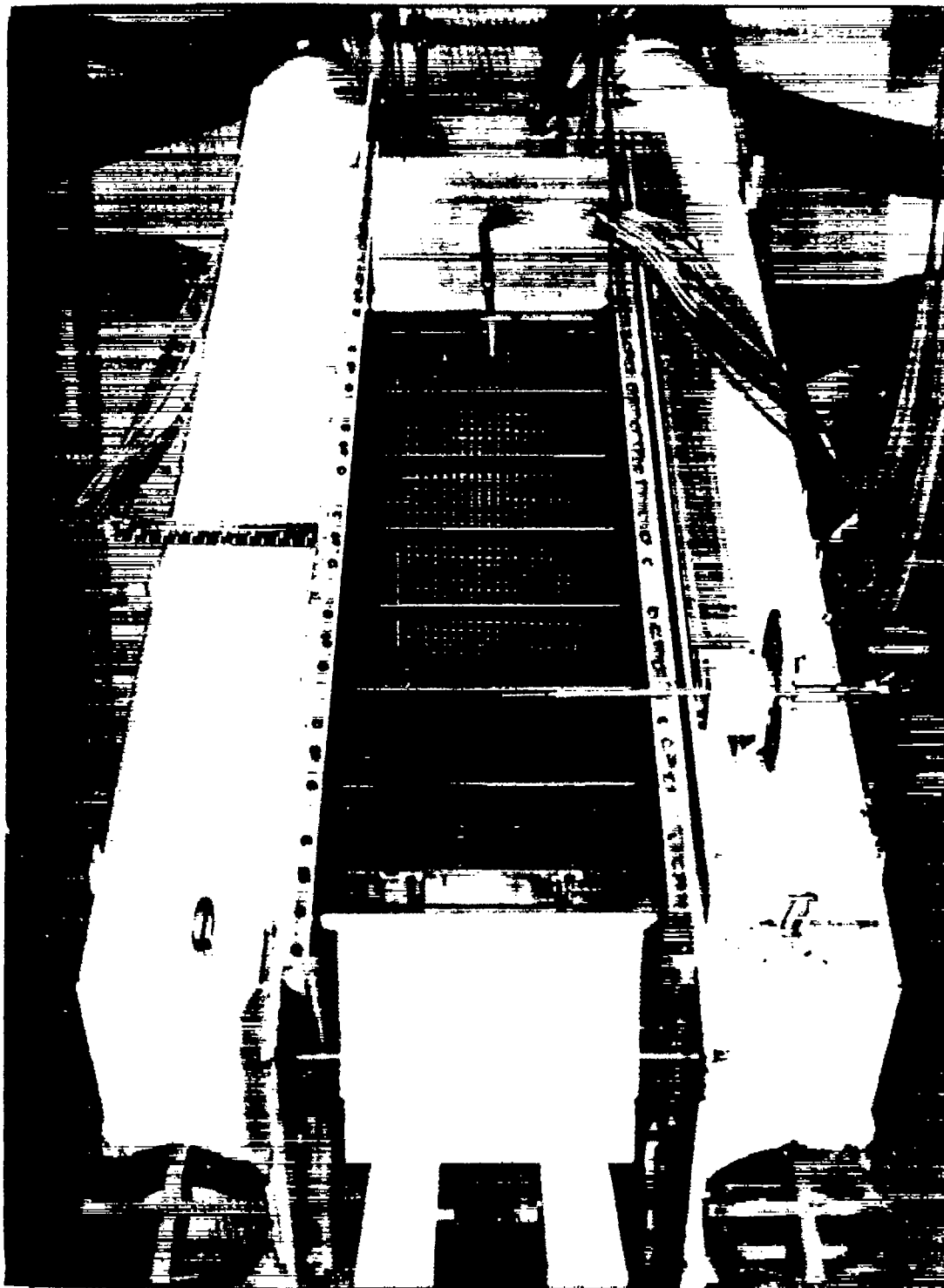


Figure 1.- Photograph of Langley 10-inch cascade.

L-87133

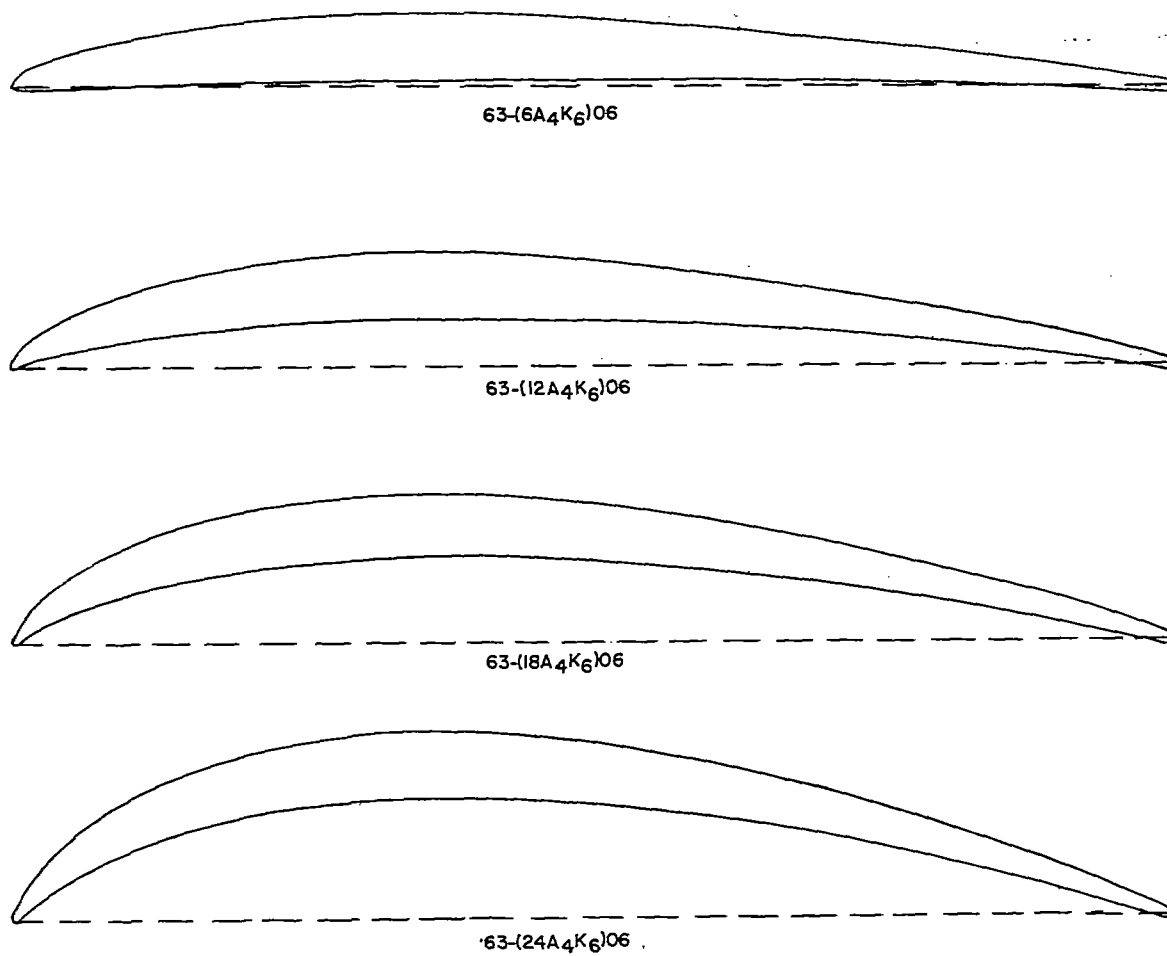


Figure 2.- Blade sections tested in this investigation.

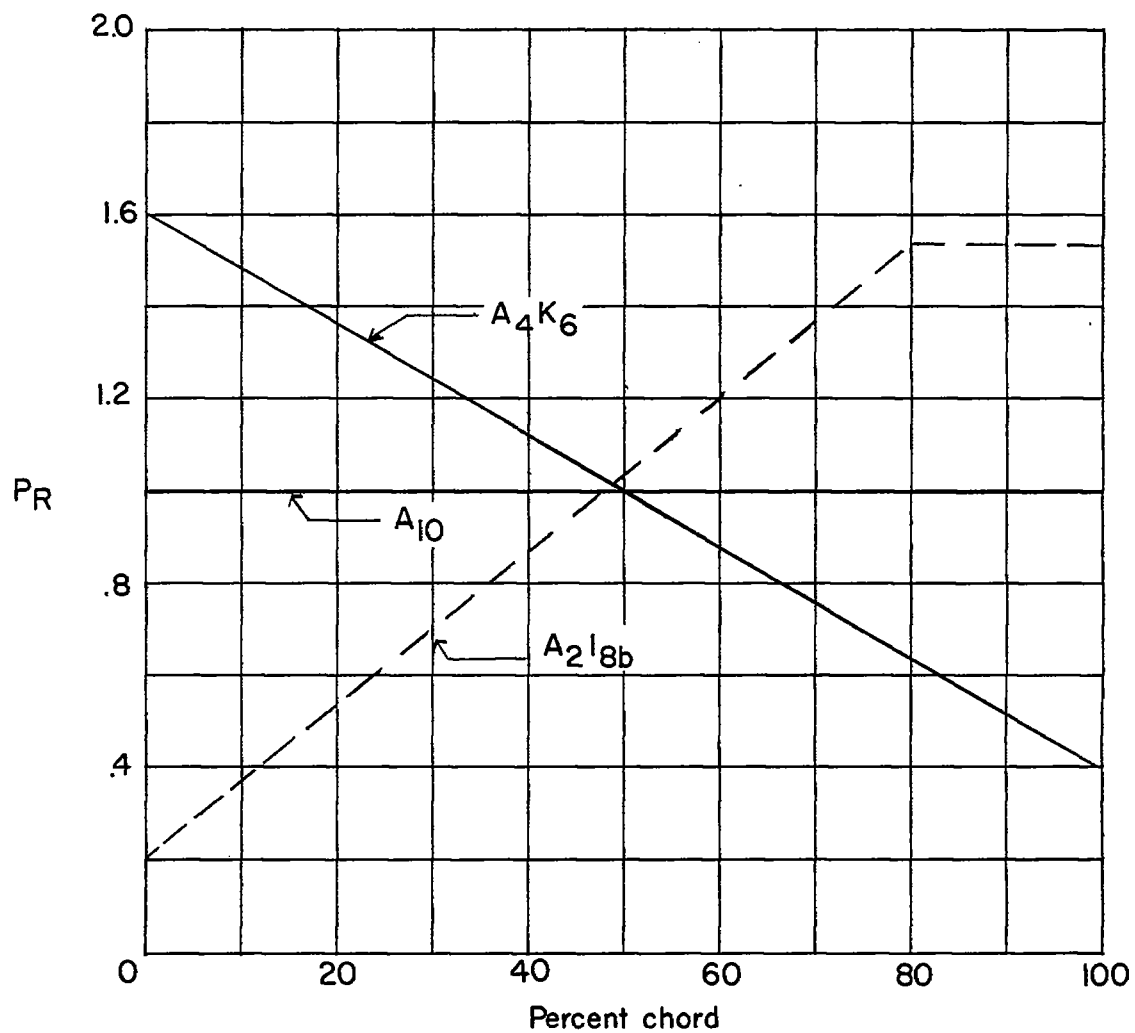


Figure 3.- Chordwise load distribution of the isolated airfoil for the A_4K_6 , A_2I_{8b} , and A_{10} mean lines.

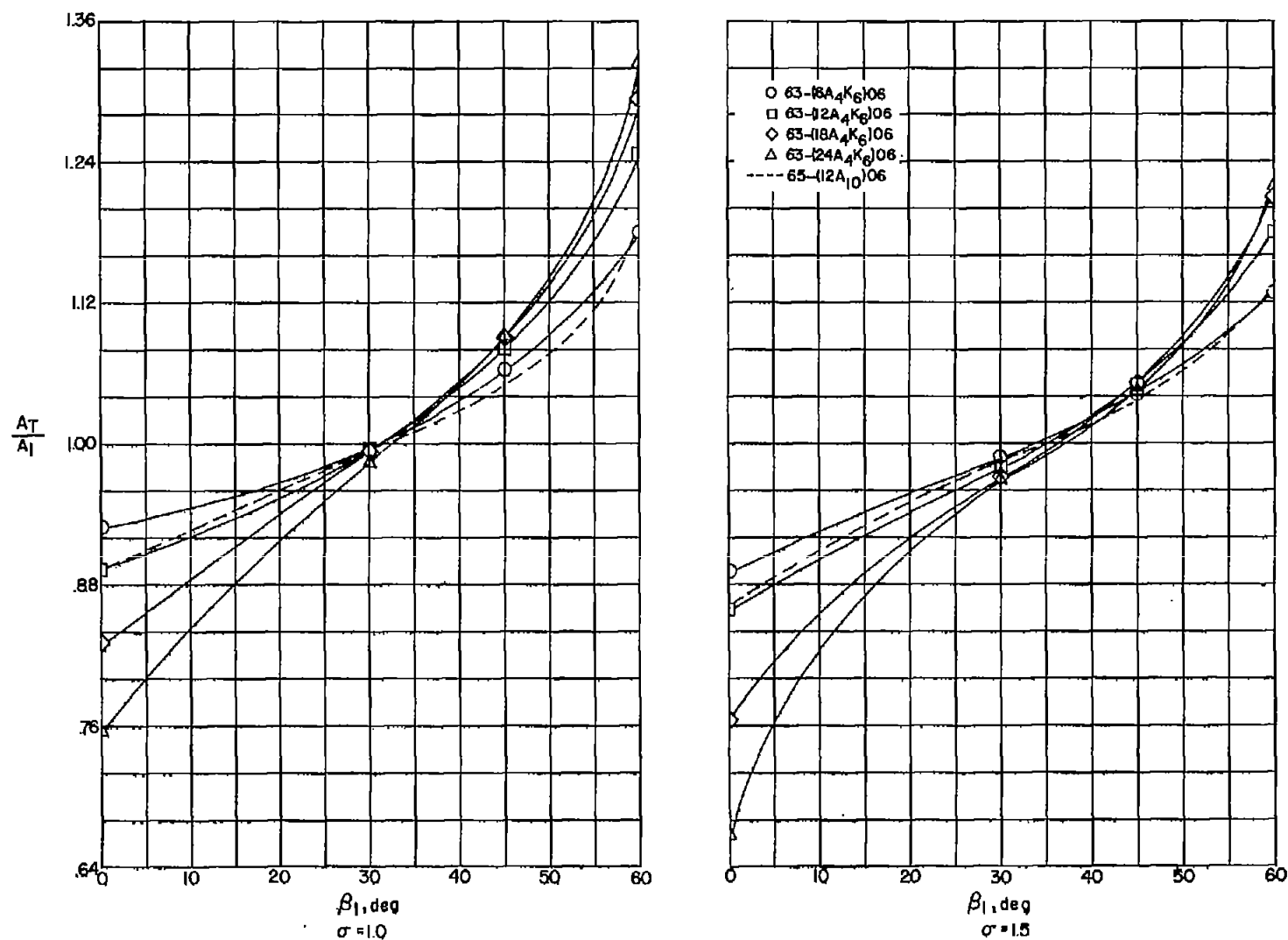


Figure 4.- Ratio of blade-passage throat area to area of upstream flow at α_1 .

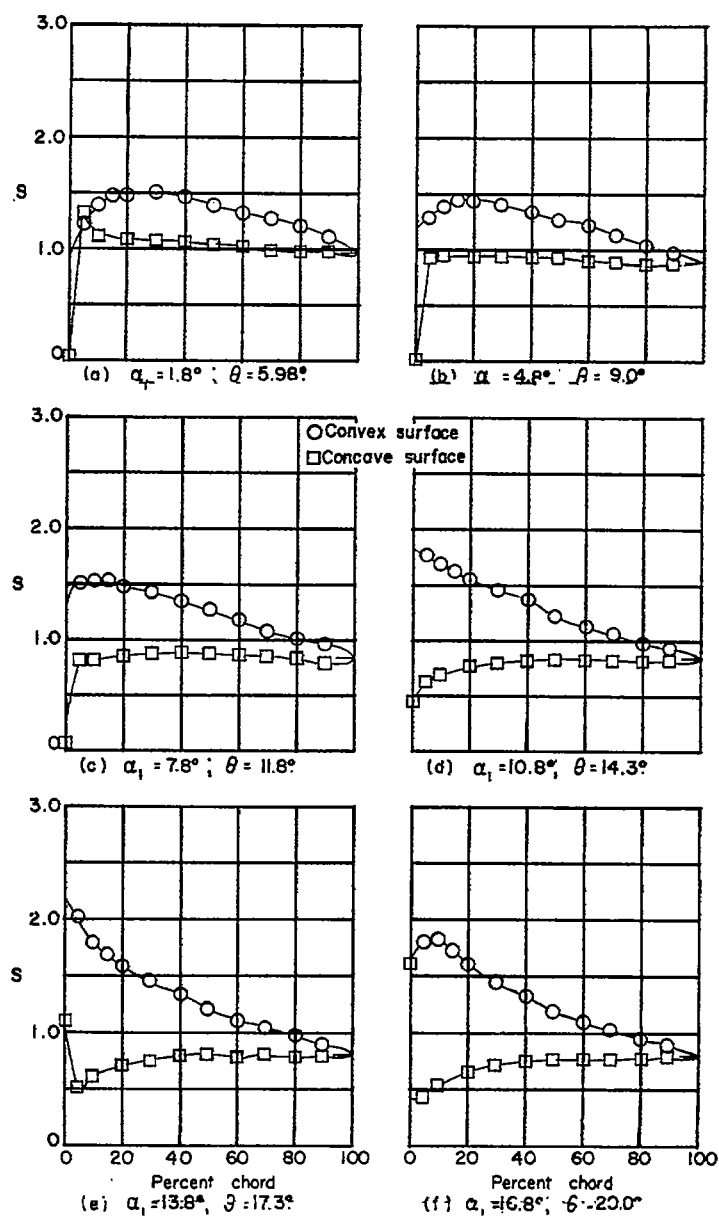
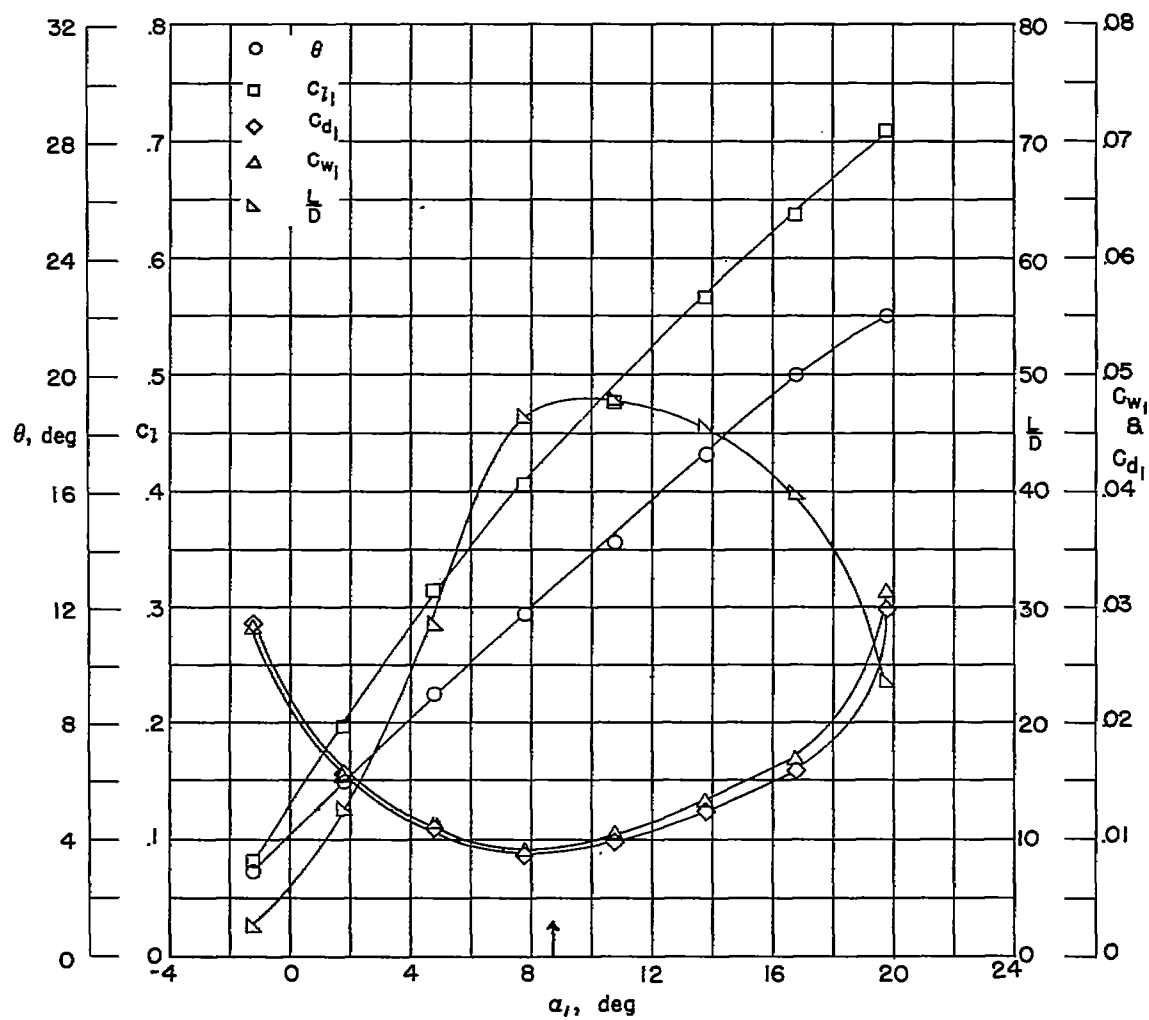


Figure 5.- Blade-surface pressure distributions and section characteristics _____
for the cascade combination $\beta = 30^\circ$; $\sigma = 1.0$; and blade section
63-(6A₄K₆)06.



(g) Section characteristics; arrow shows design angle of attack.

Figure 5.- Concluded.

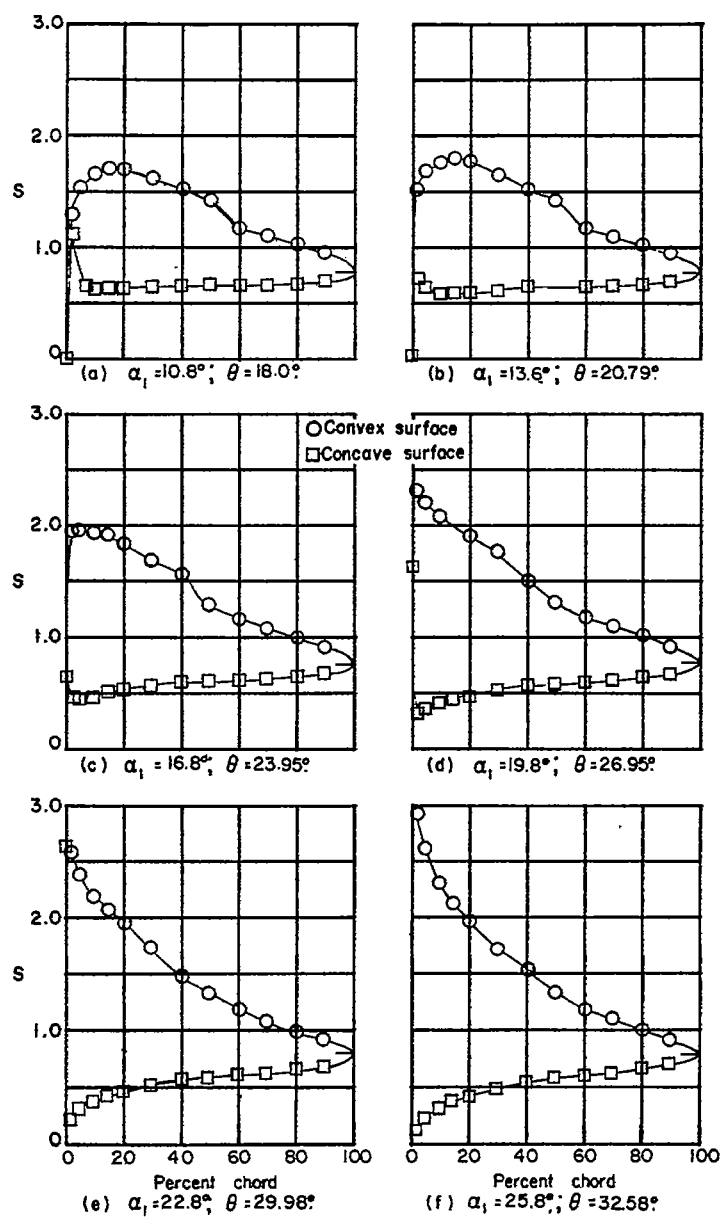
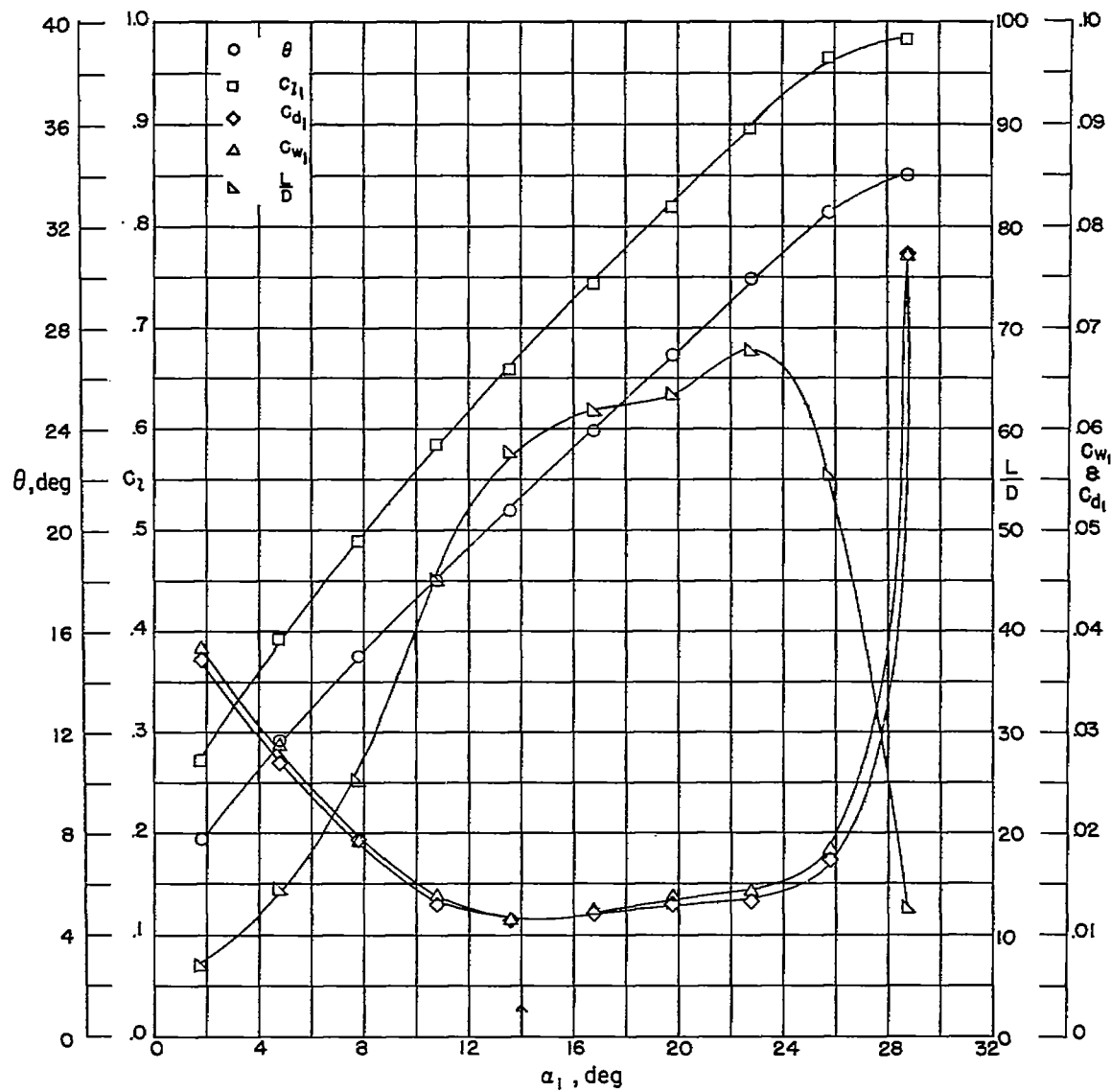


Figure 6.- Blade-surface pressure distributions and section characteristics for the cascade combination $\beta = 30^\circ$; $\sigma = 1.0$; and blade section 63-(12A₄K₆)06.



(g) Section characteristics; arrow shows design angle of attack

Figure 6.- Concluded.

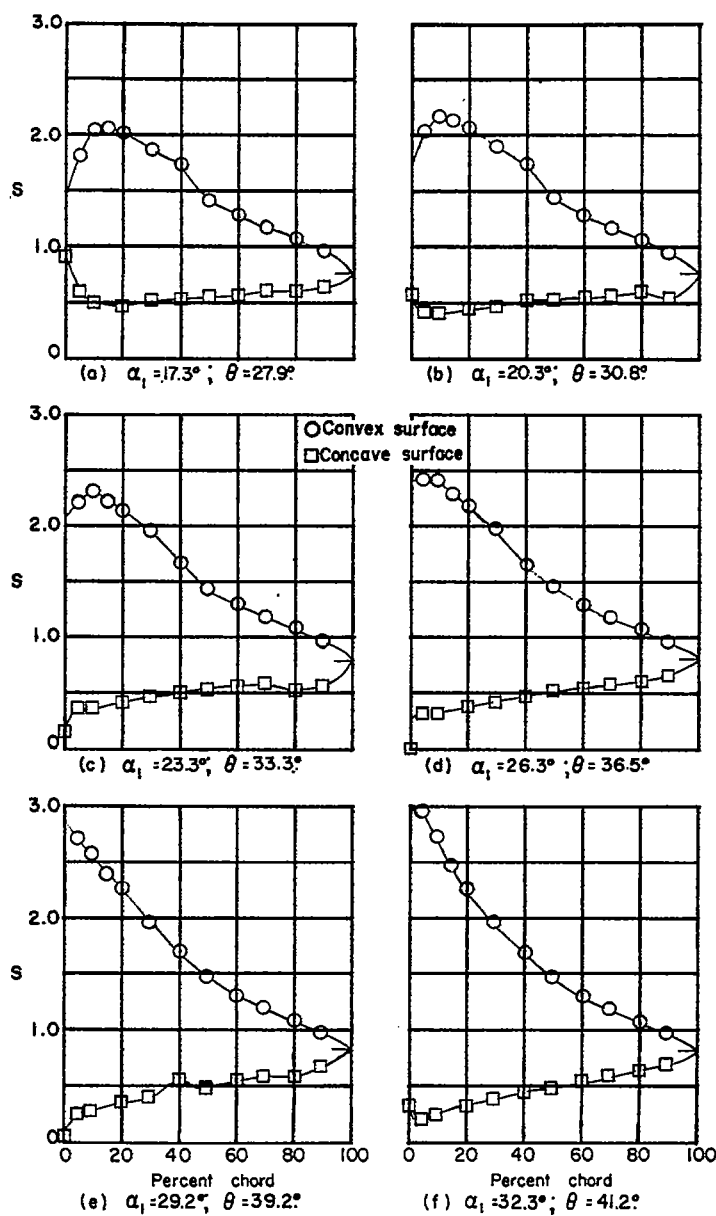
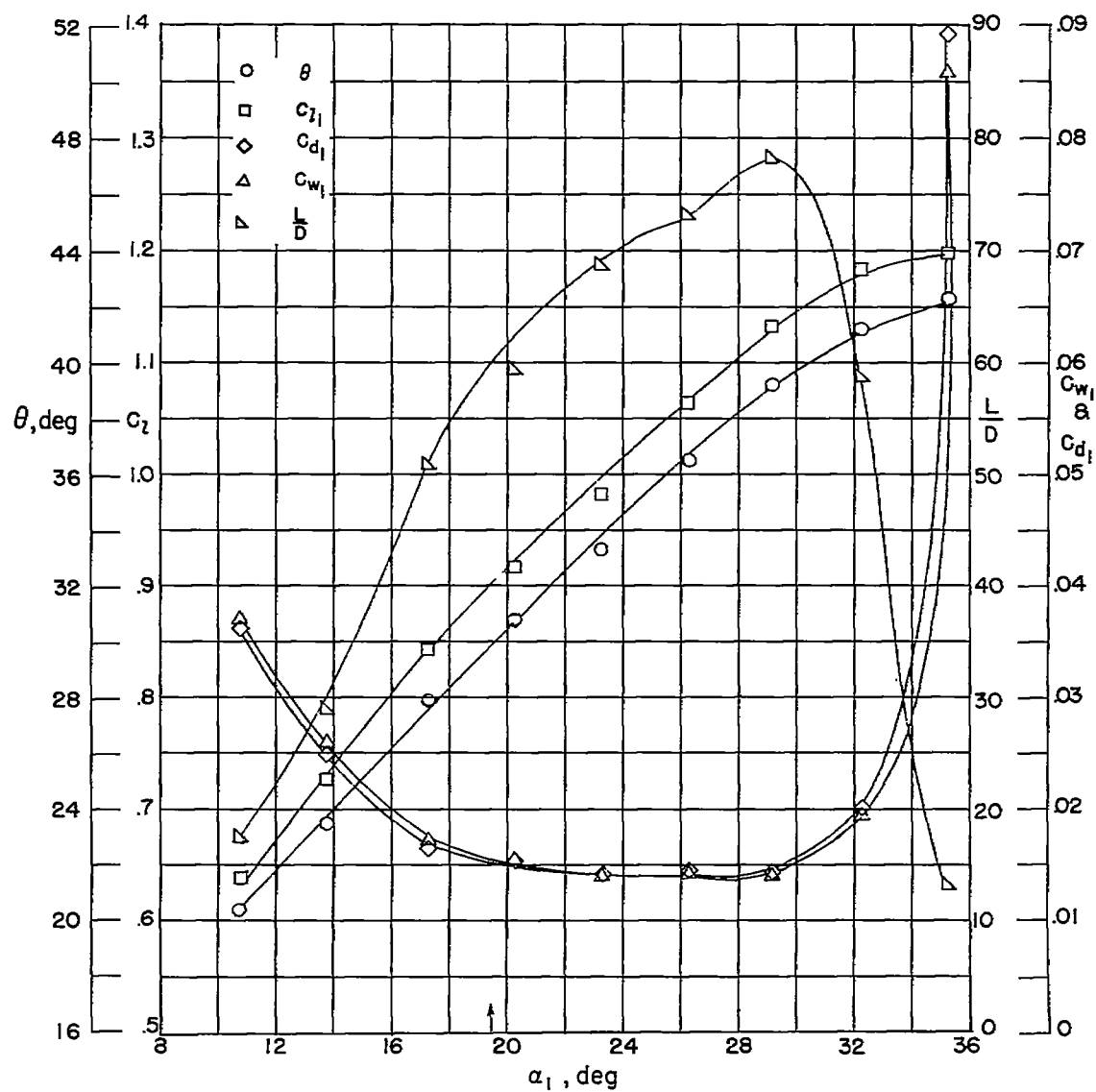


Figure 7.- Blade-surface pressure distributions and section characteristics for the cascade combination $\beta = 30^\circ$; $\sigma = 1.0$; and blade section 63-(18A₄K₆)06.



(g) Section characteristics; arrow shows design angle of attack.

Figure 7.- Concluded.

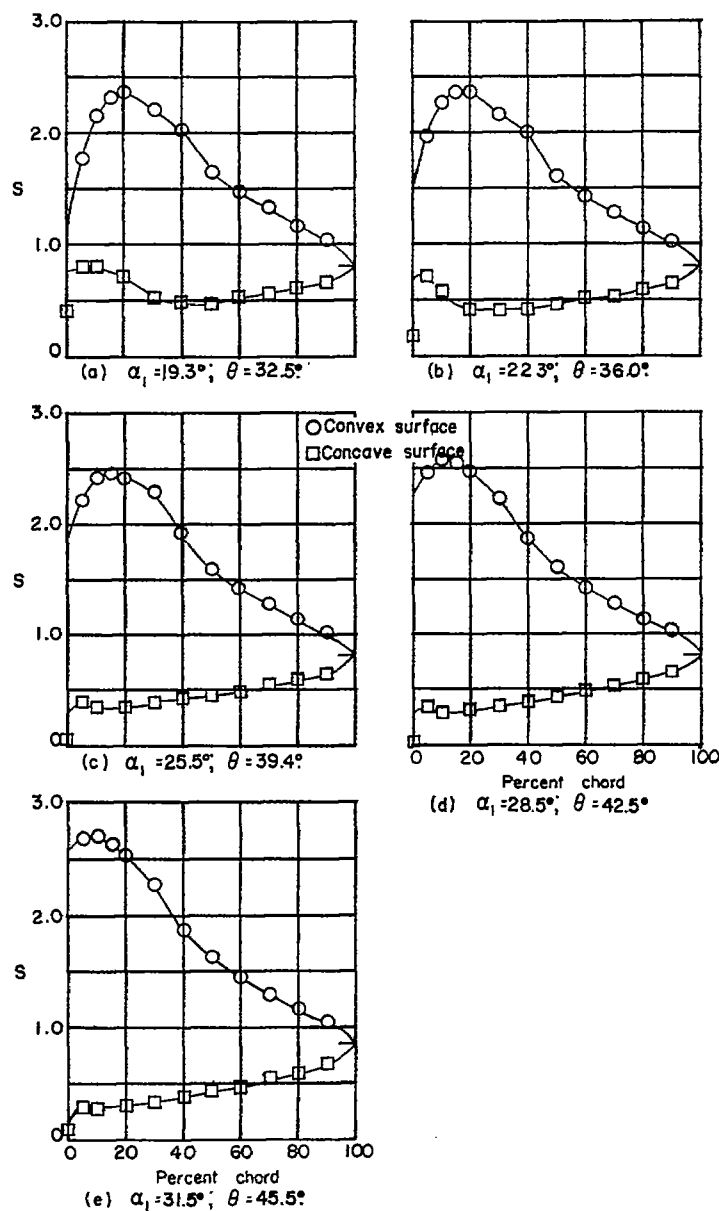
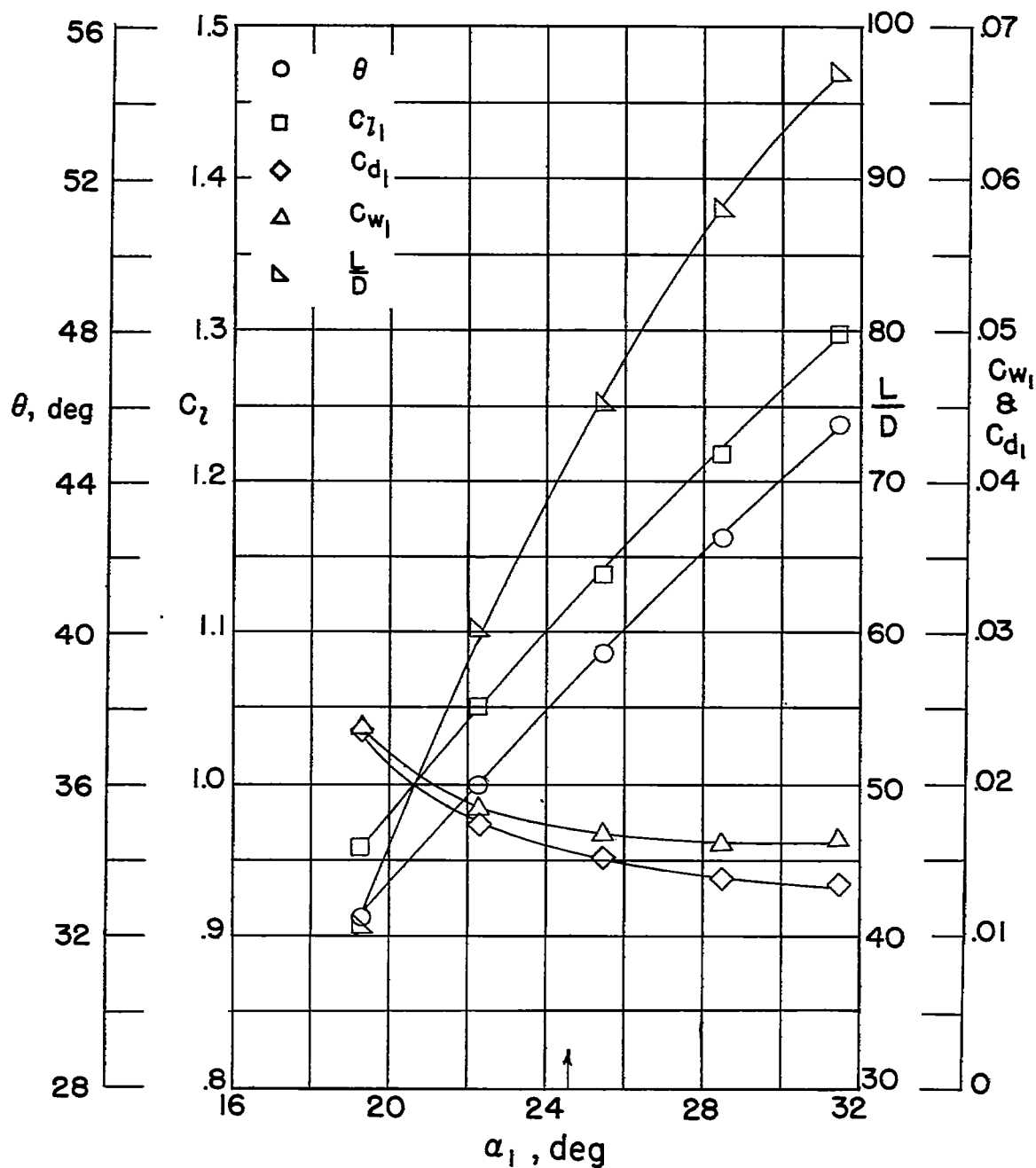


Figure 8.- Blade-surface pressure distributions and section characteristics for the cascade combination $\beta = 30^\circ$; $\sigma = 1.0$; and blade section 63-(24A₄K₆)06.



(f) Section characteristics; arrow shows design angle of attack.

Figure 8.- Concluded.

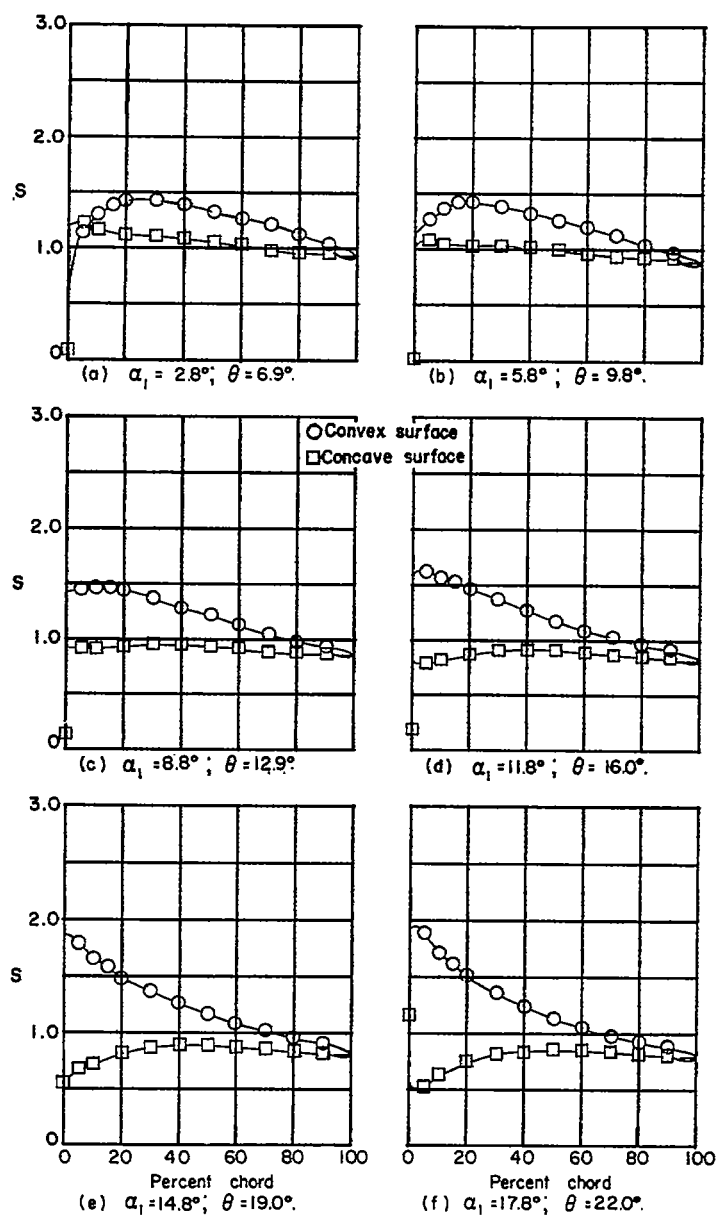
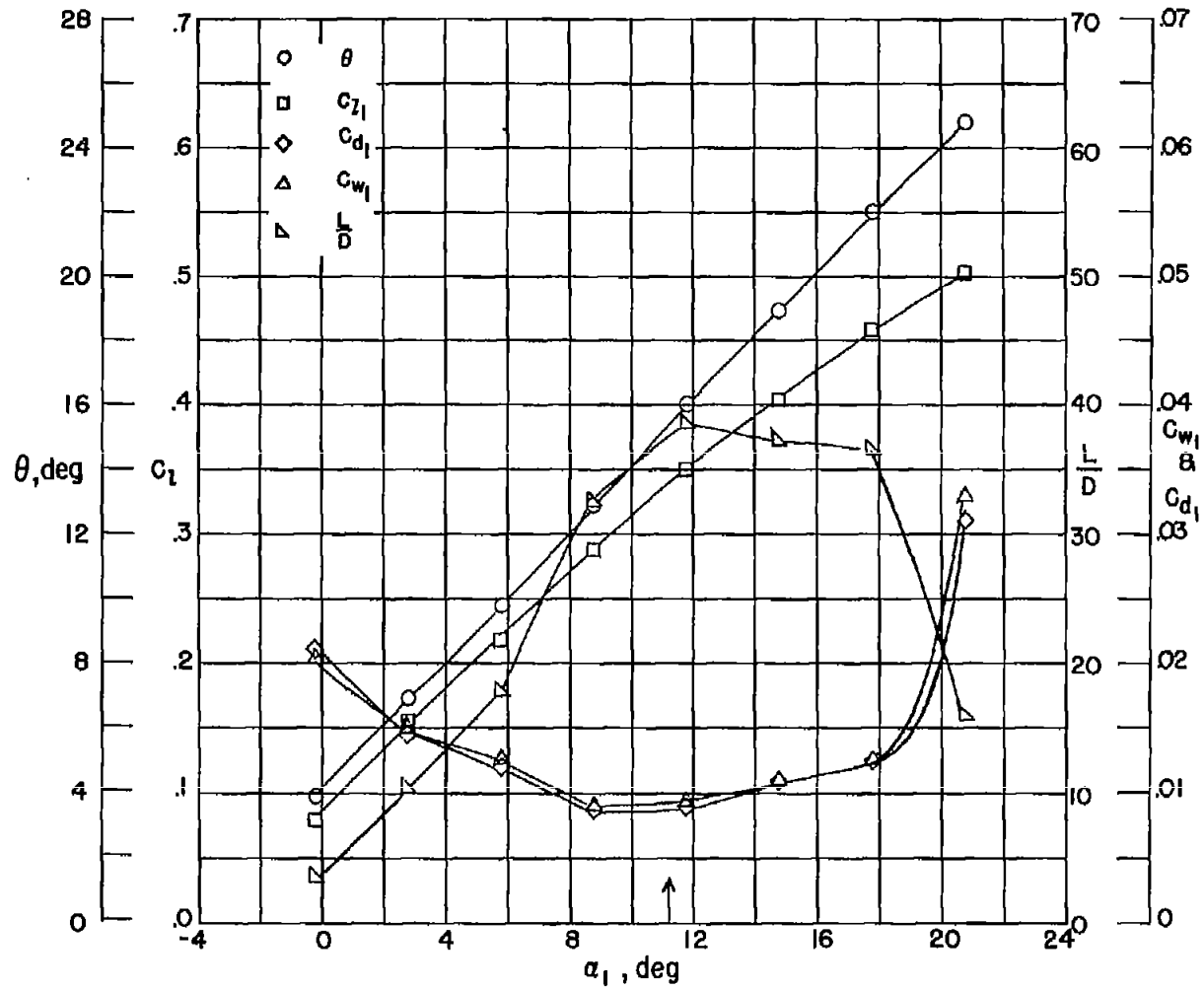


Figure 9.- Blade-surface pressure distributions and section characteristics for the cascade combination $\beta = 30^\circ$; $\sigma = 1.5$; and blade section 63-(6A₄K₆)06.



(g) Section characteristics; arrow shows design angle of attack.

Figure 9.- Concluded.

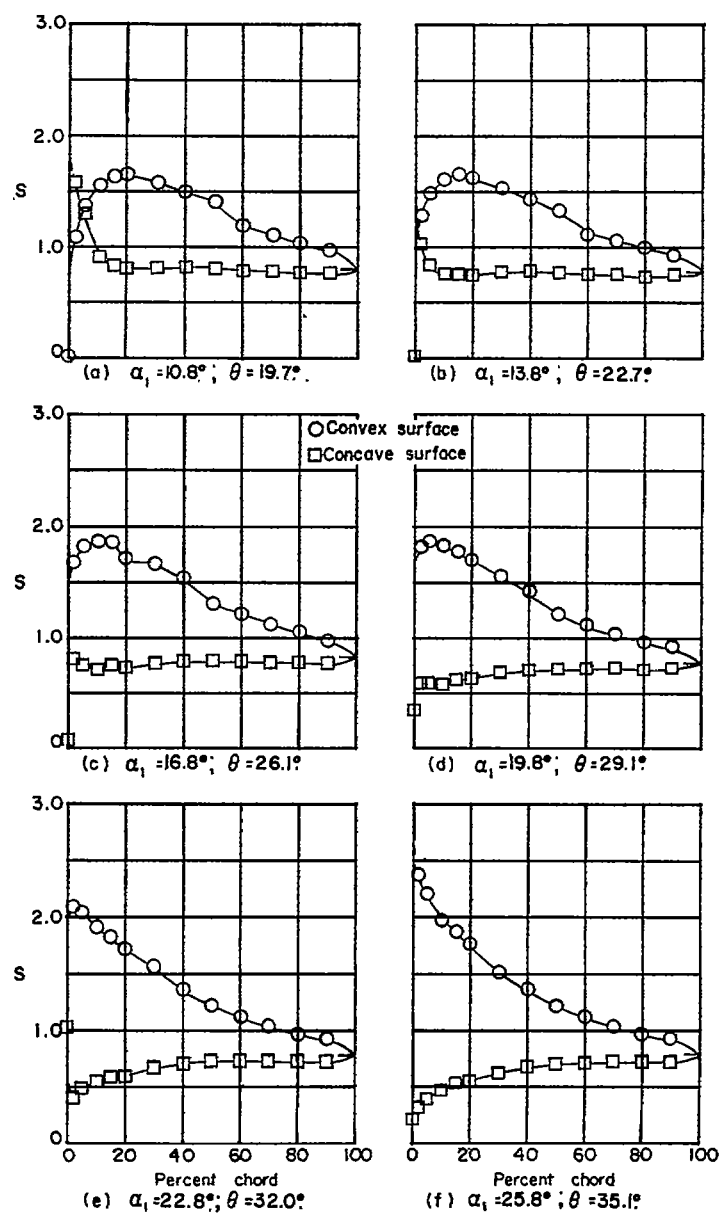
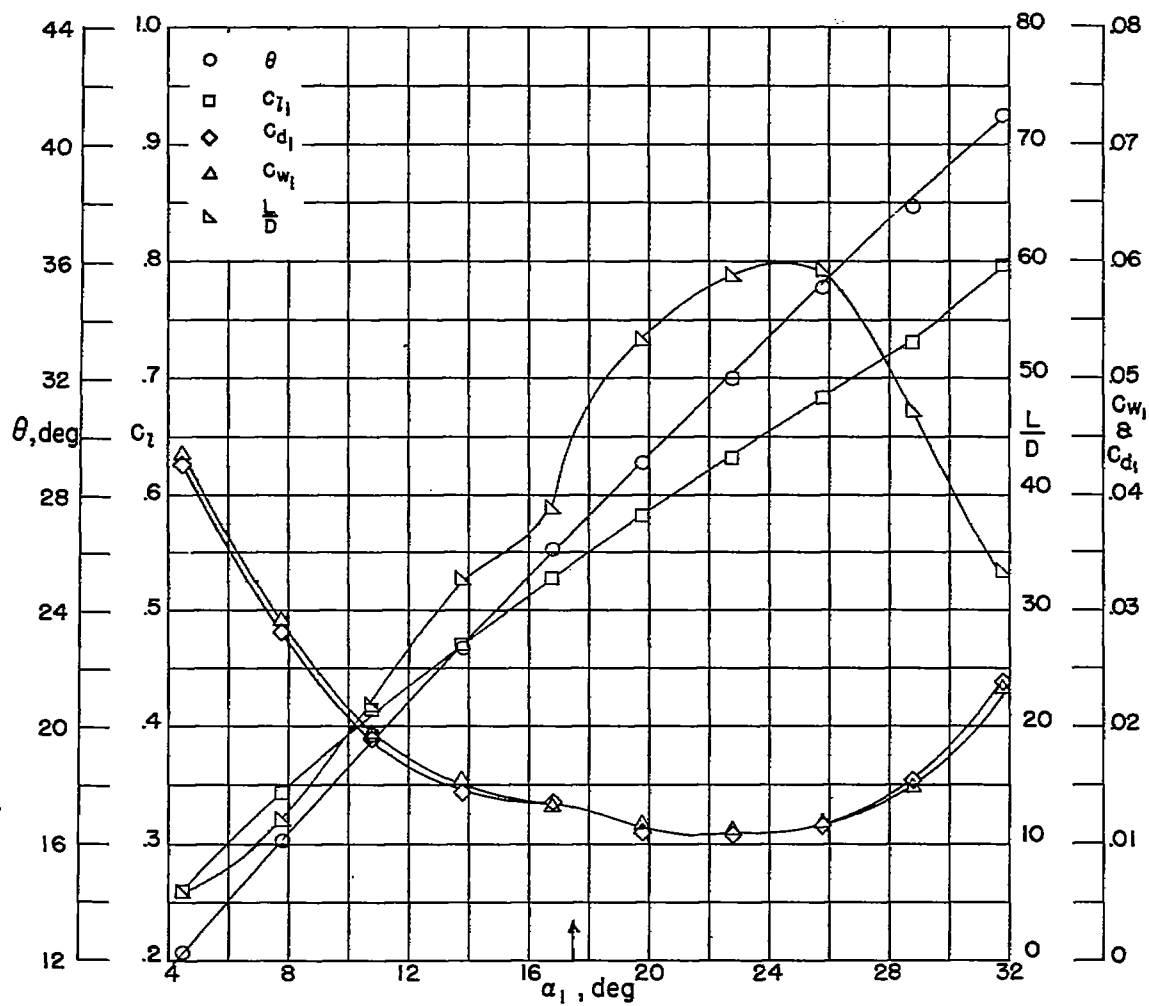


Figure 10.- Blade-surface pressure distributions and section characteristics for the cascade combination $\beta = 30^\circ$; $\sigma = 1.5$; and blade section 63-(12A₄K₆)06.



(g) Section characteristics; arrow shows design angle of attack.

Figure 10.- Concluded.

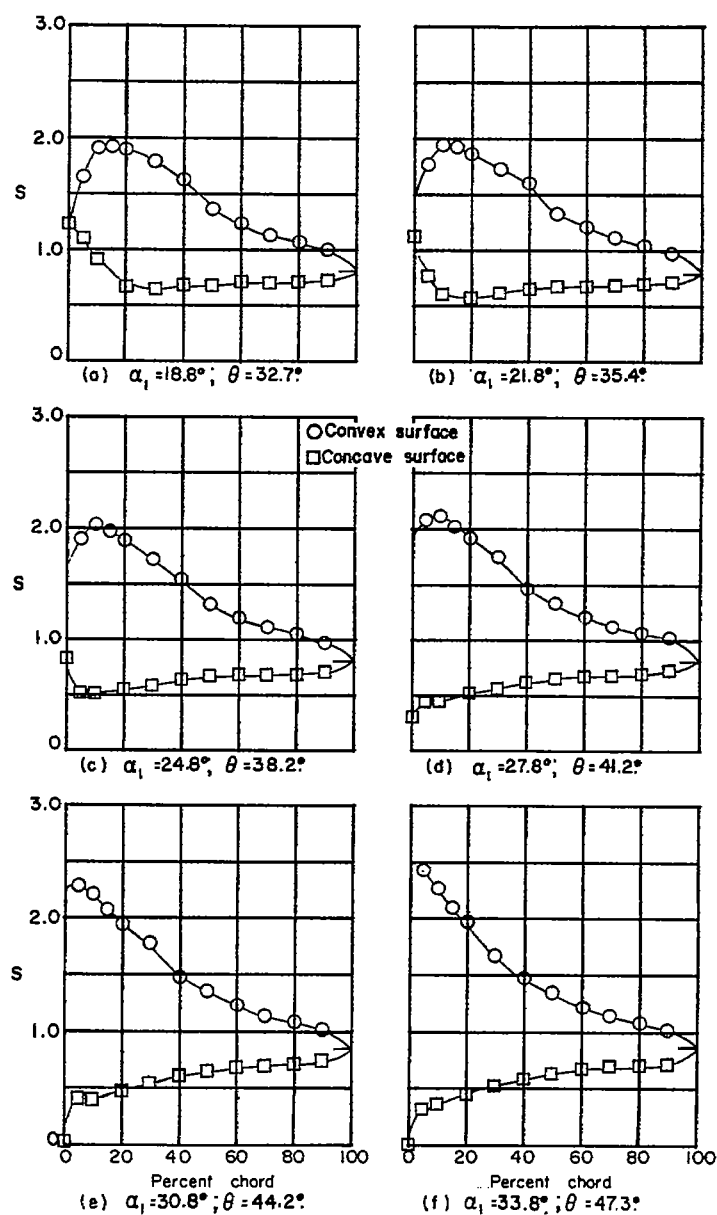
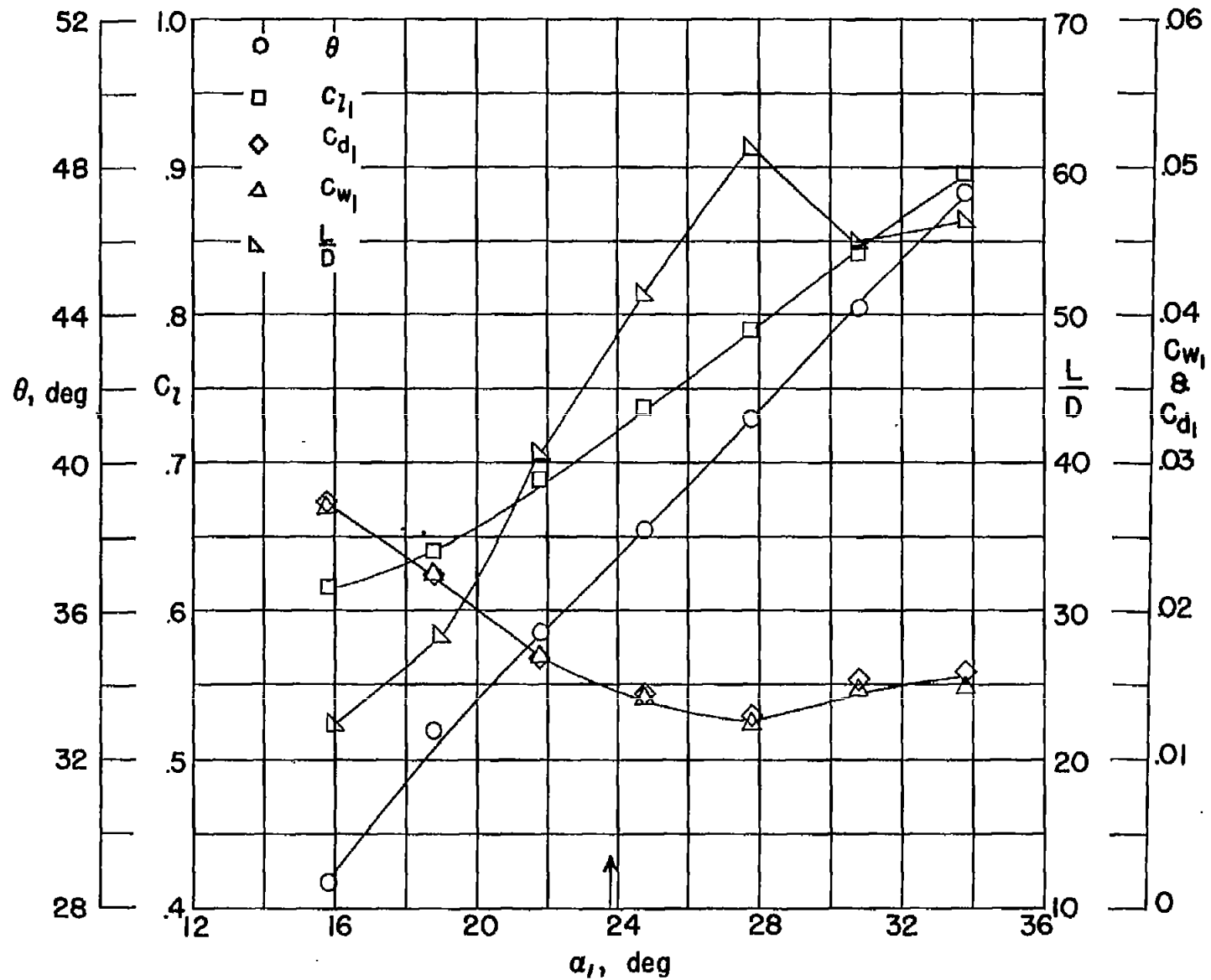


Figure 11.- Blade-surface pressure distributions and section characteristics for the cascade combination $\beta = 30^\circ$; $\sigma = 1.5$; and blade section 63-(18A₄K₆)06.



(g) Section characteristics; arrow shows design angle of attack.

Figure 11.- Concluded.

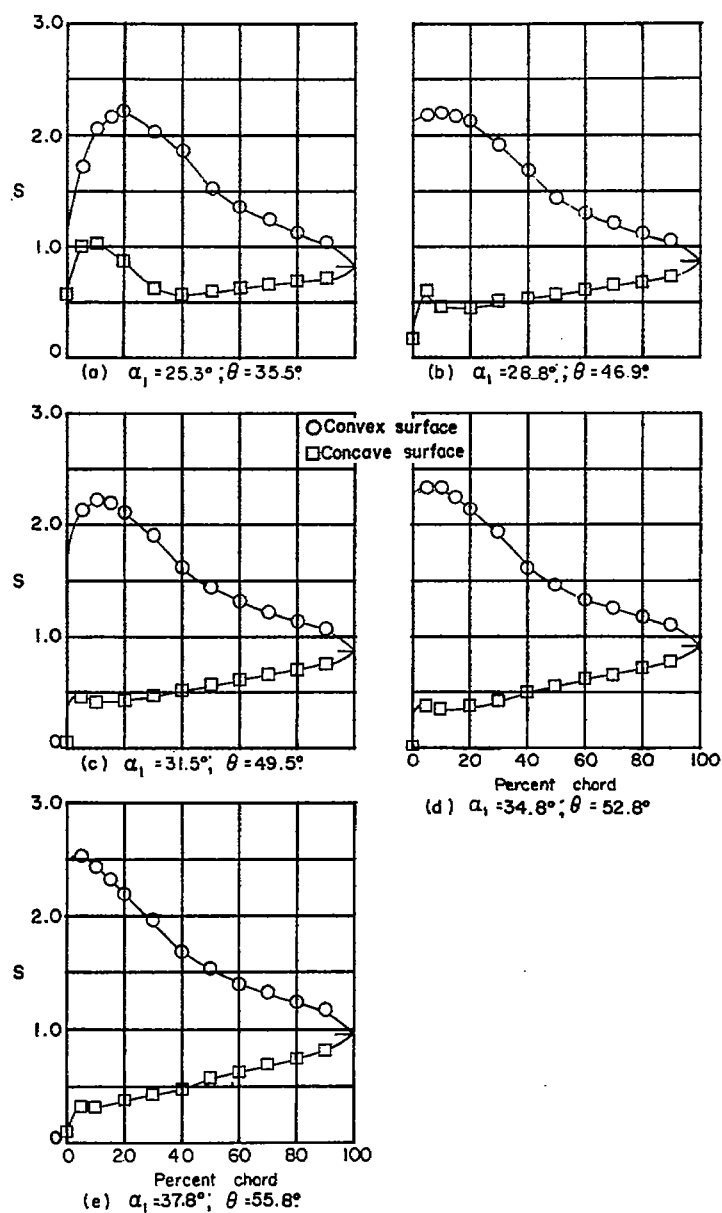
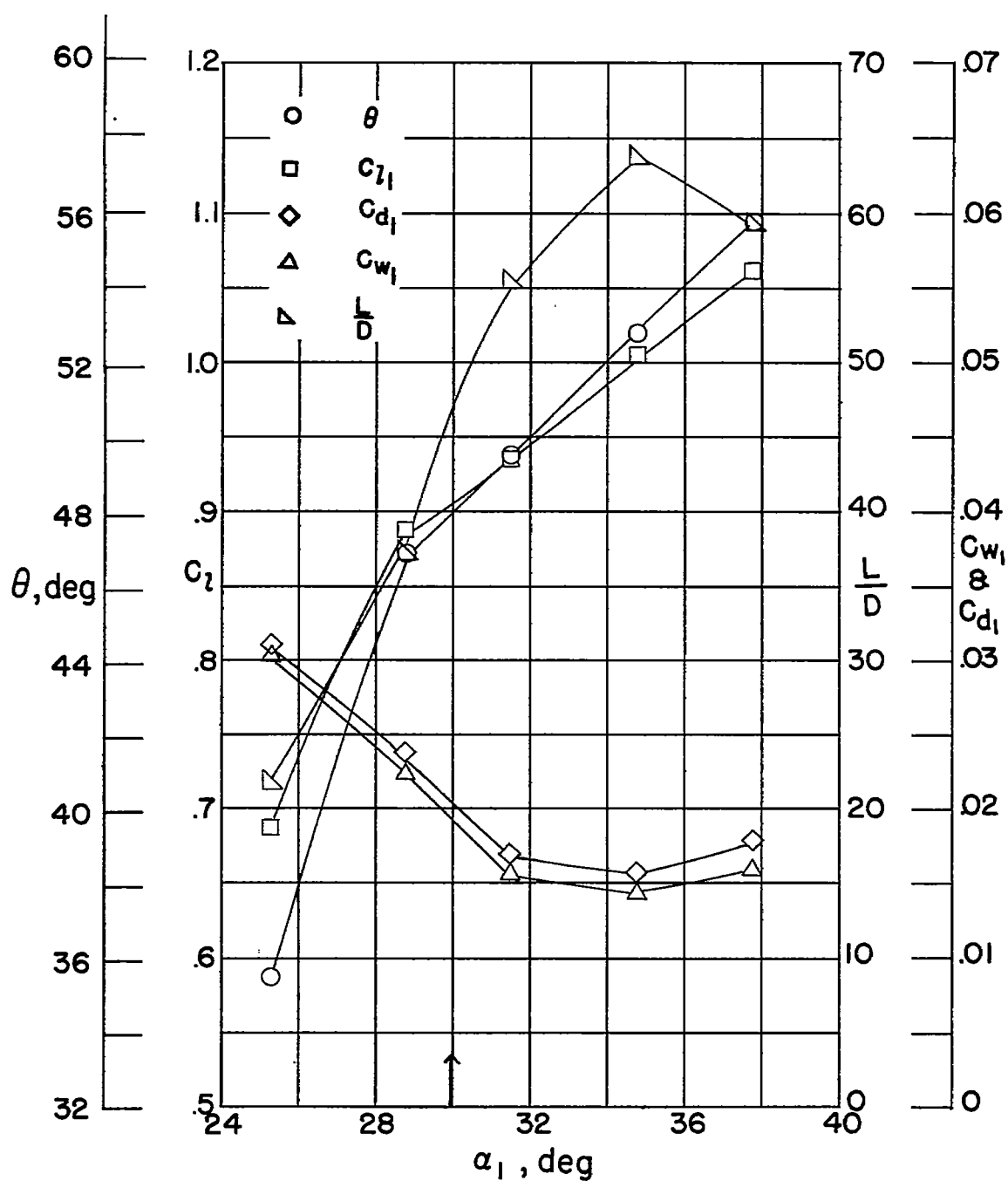


Figure 12.- Blade-surface pressure distributions and section characteristics for the cascade combination $\beta = 30^\circ$; $\sigma = 1.5$; and blade section 63-(24A₄K₆)06.



(f) Section characteristics; arrow shows design angle of attack.

Figure 12.- Concluded.

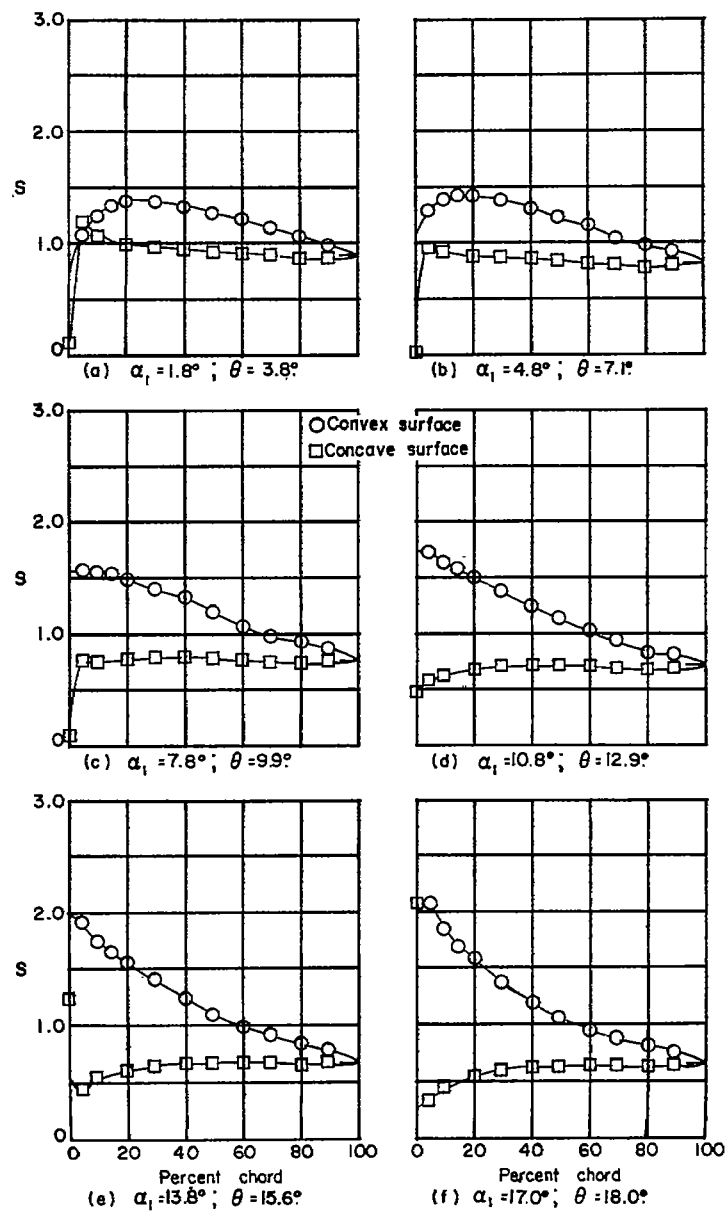
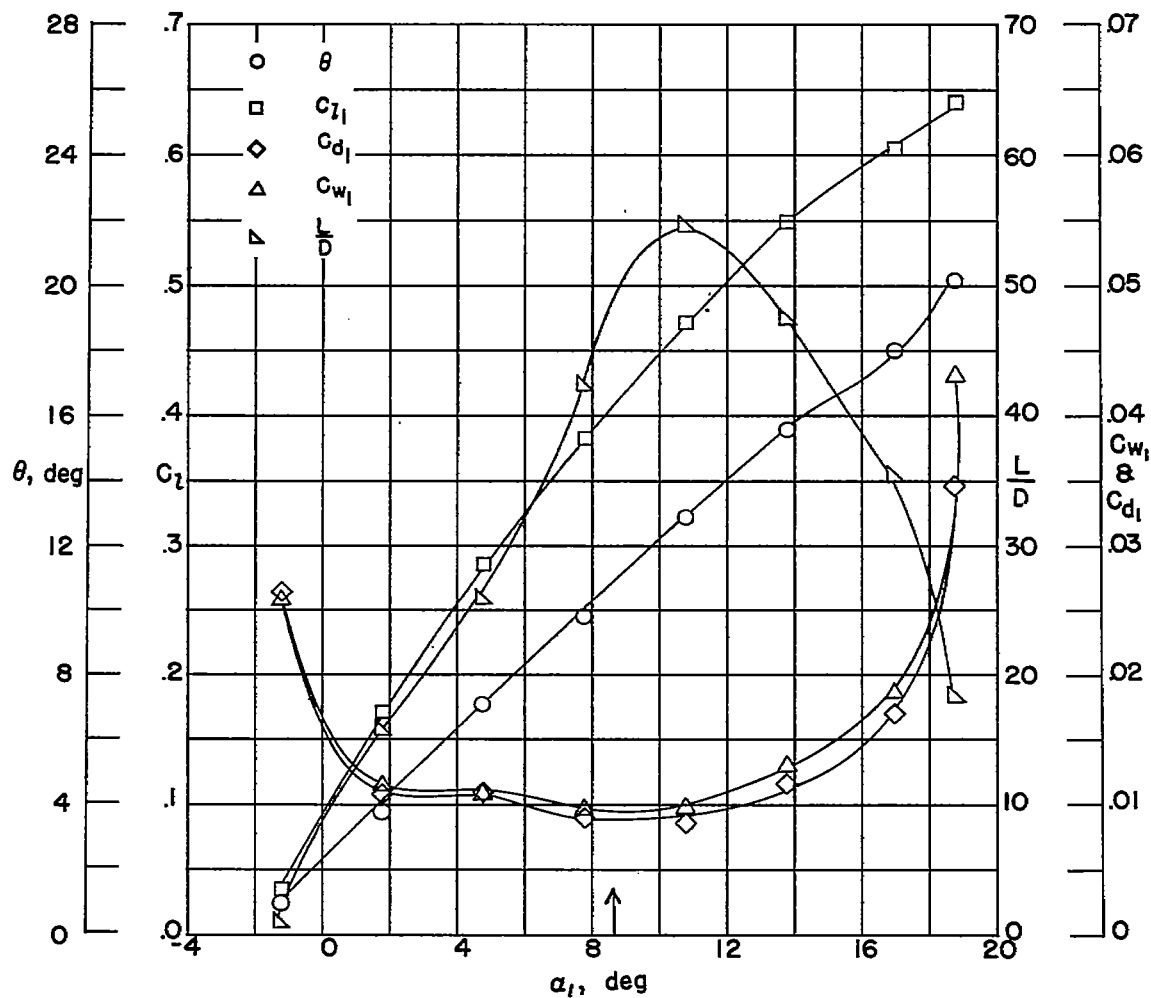


Figure 13.- Blade-surface pressure distributions and section characteristics for the cascade combination $\beta = 45^\circ$; $\sigma = 1.0$; and blade section 63-(6A4K6)06.



(g) Section characteristics; arrow shows design angle of attack.

Figure 13.- Concluded.

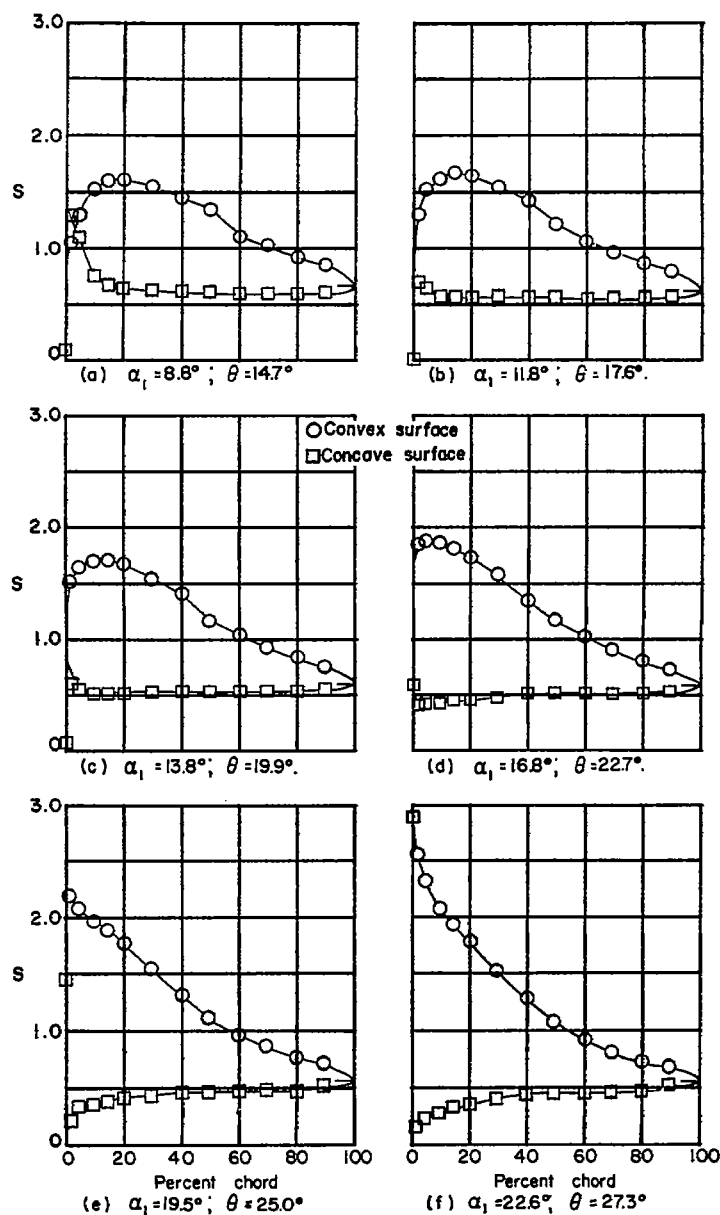
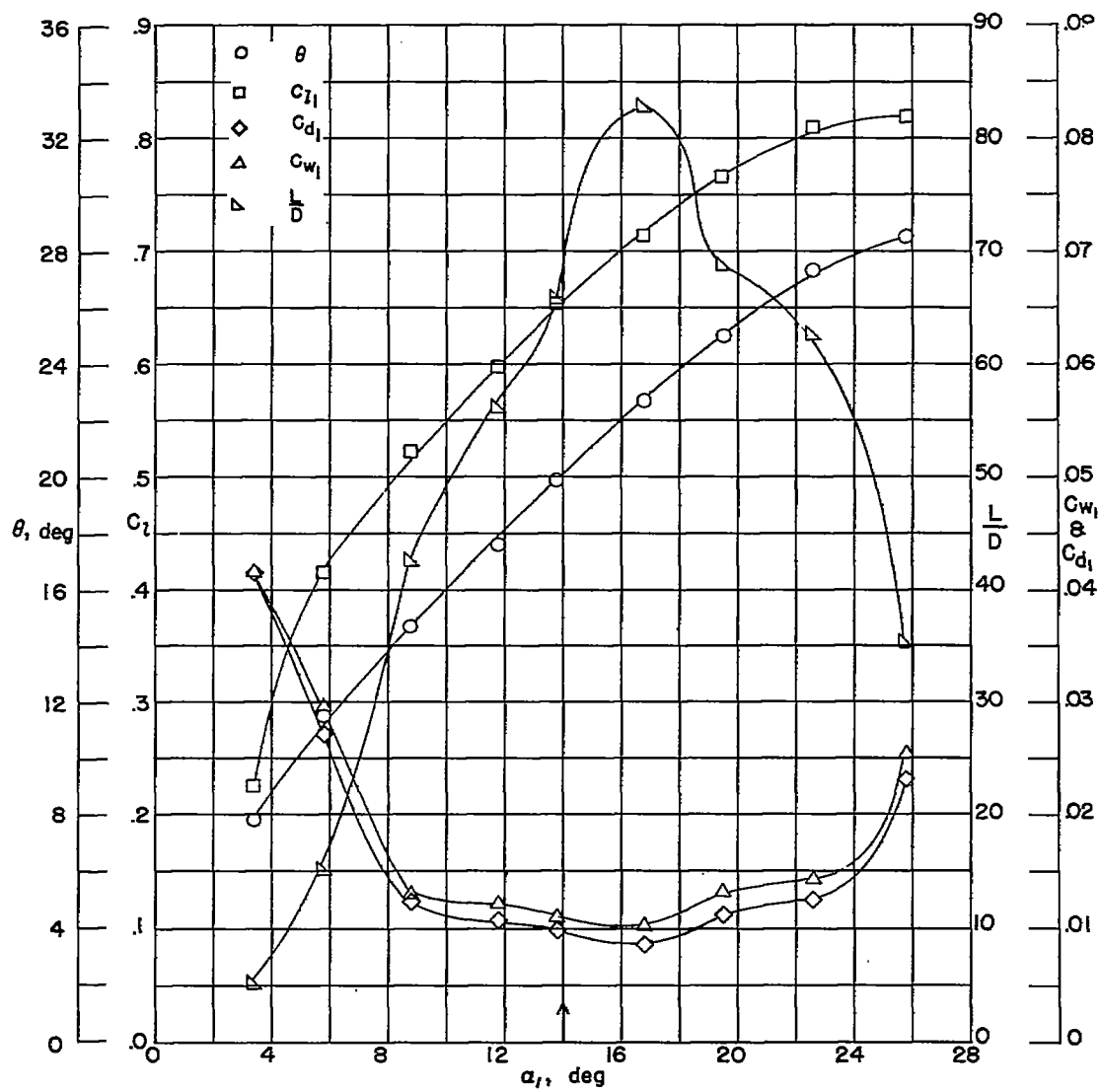


Figure 14.- Blade-surface pressure distributions and section characteristics for the cascade combination $\beta = 45^\circ$; $\sigma = 1.0$; and blade section 63-(12A₄K₆)06.



(g) Section characteristics; arrow shows design angle of attack.

Figure 14.- Concluded.

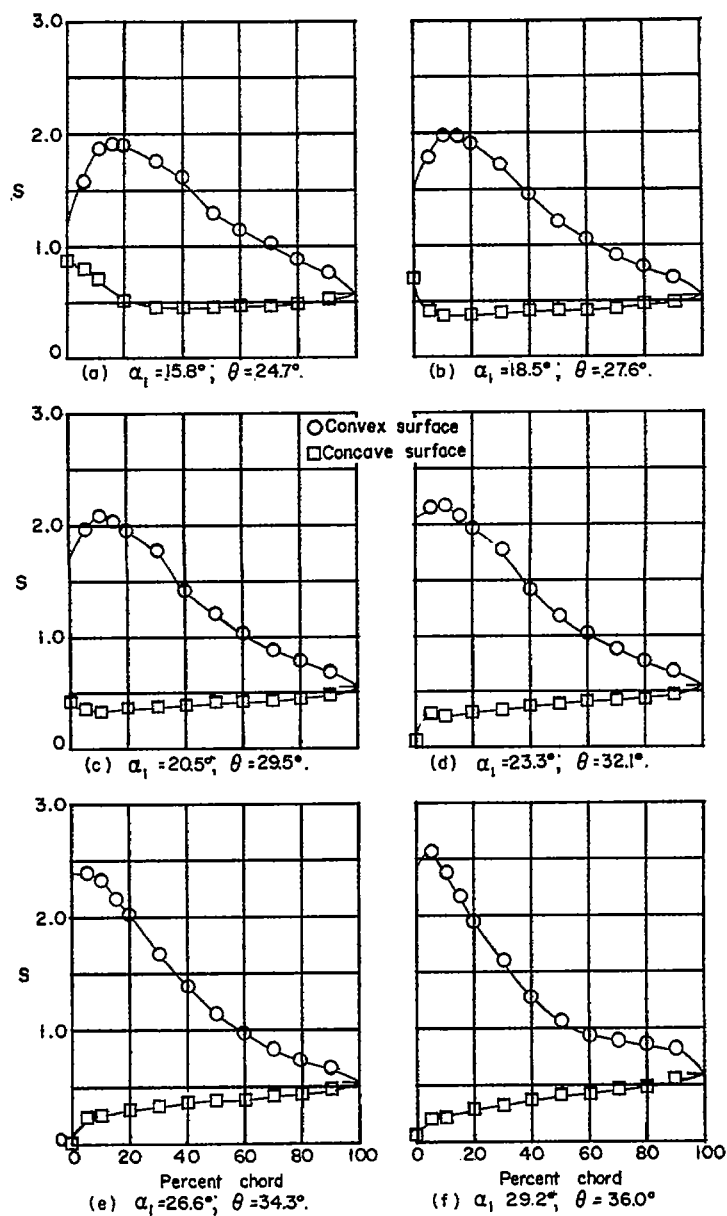
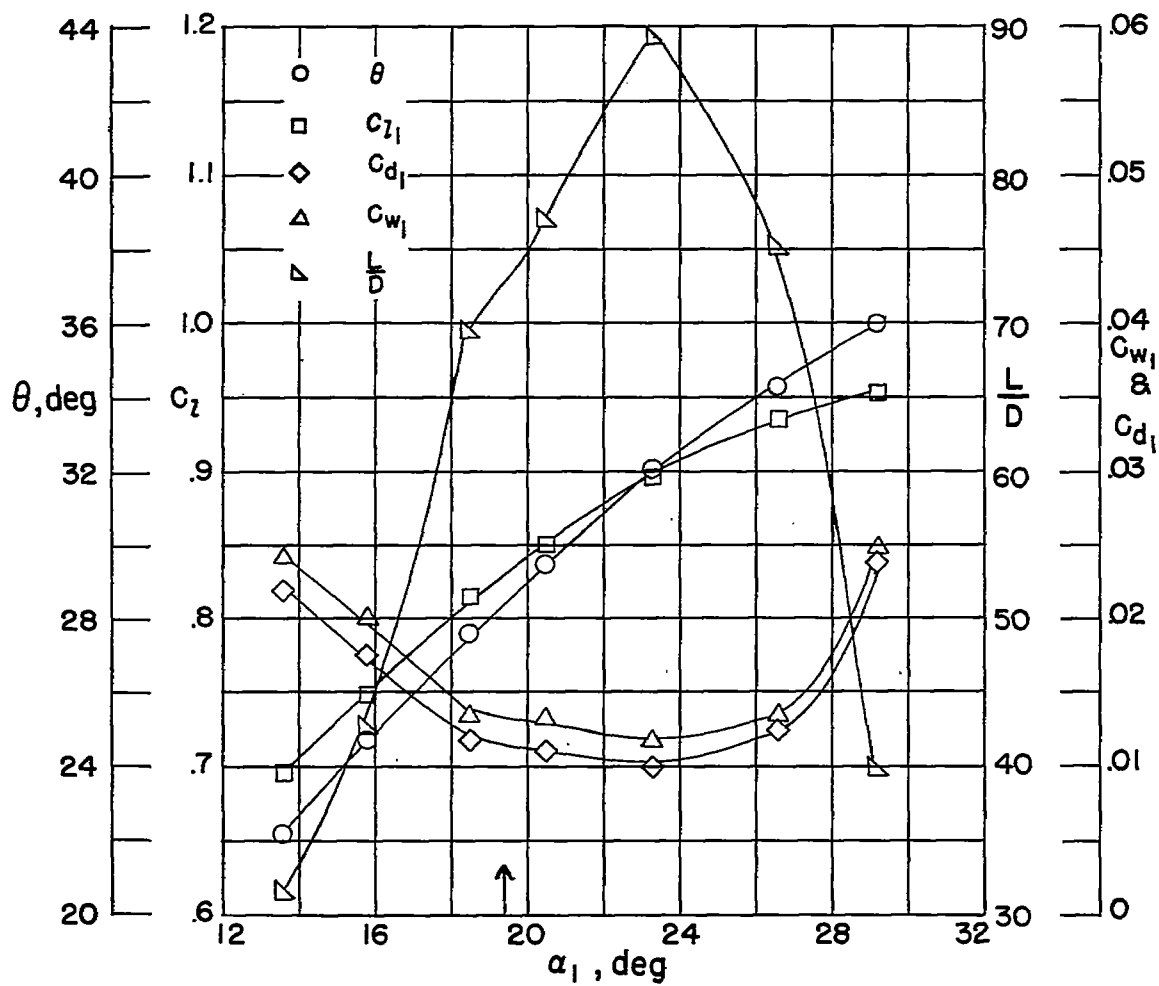


Figure 15.- Blade-surface pressure distributions and section characteristics for the cascade combination $\beta = 45^\circ$; $\sigma = 1.0$; and blade section 63-(18A₄K6)06.



(g) Section characteristics; arrow shows design angle of attack

Figure 15.- Concluded.

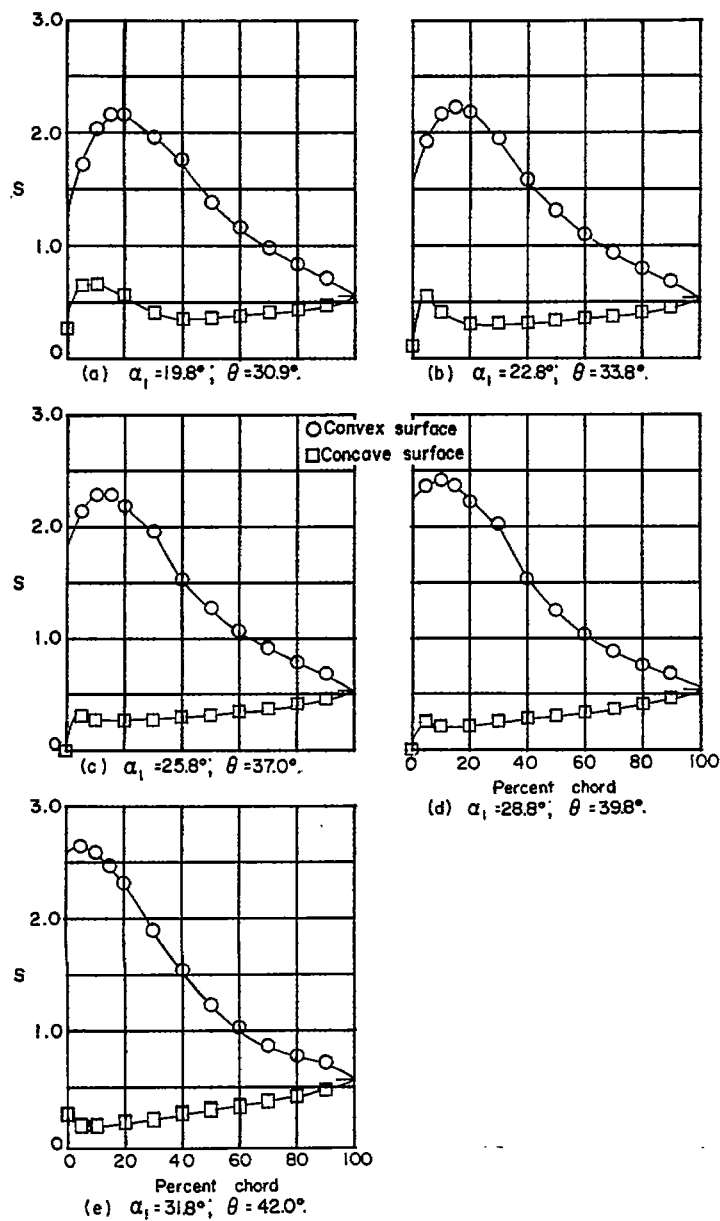
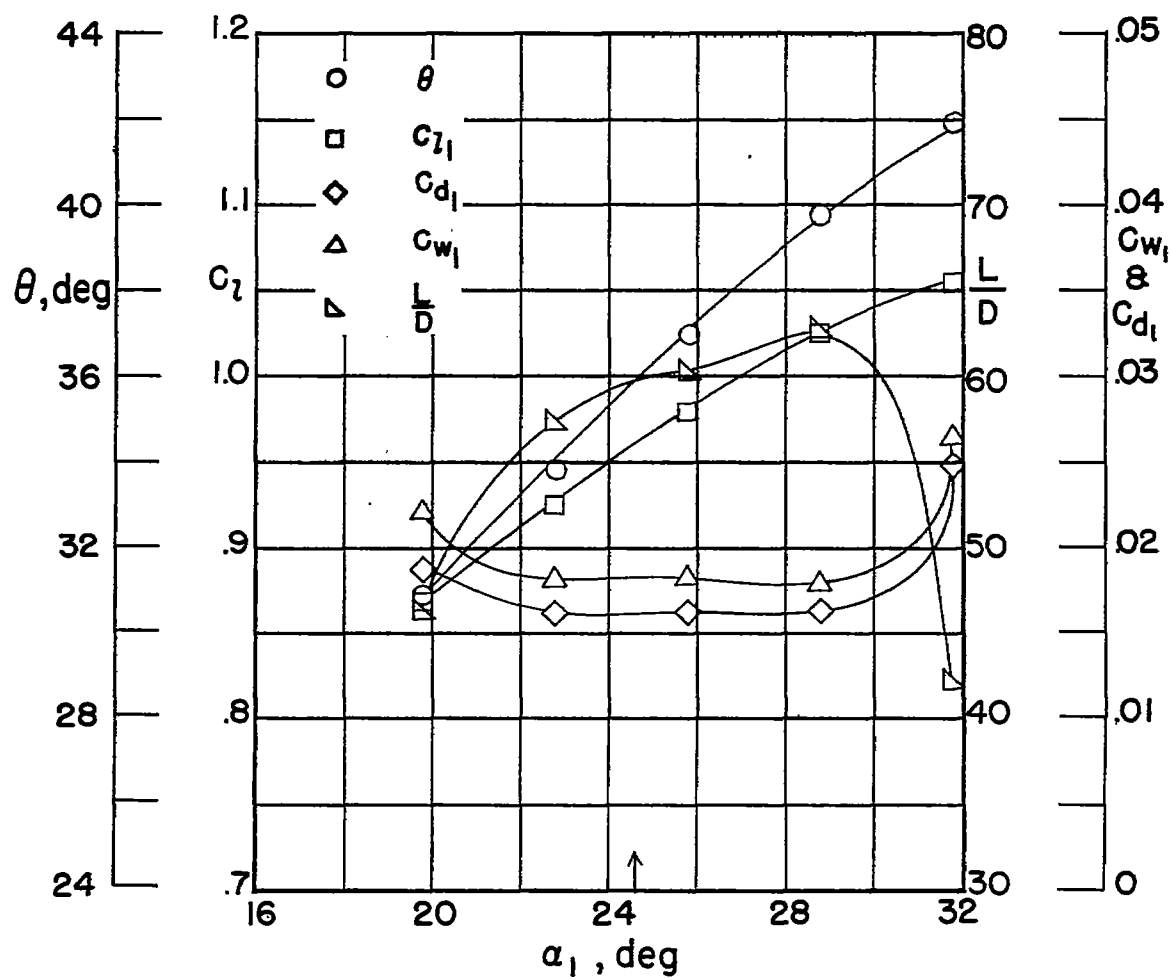


Figure 16.- Blade-surface pressure distributions and section characteristics for the cascade combination $\beta = 45^\circ$; $\sigma = 1.0$; and blade section 63-(24A4K6)06.



(f) Section characteristics; arrow shows design angle of attack.

Figure 16.- Concluded.

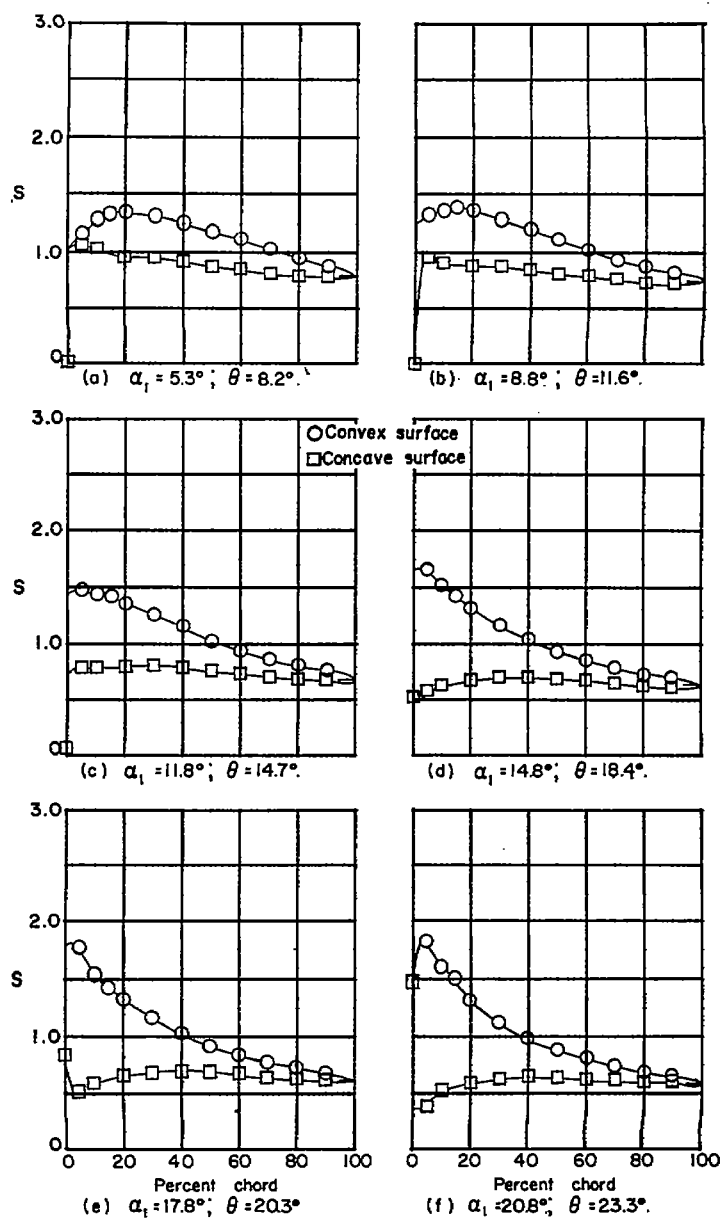
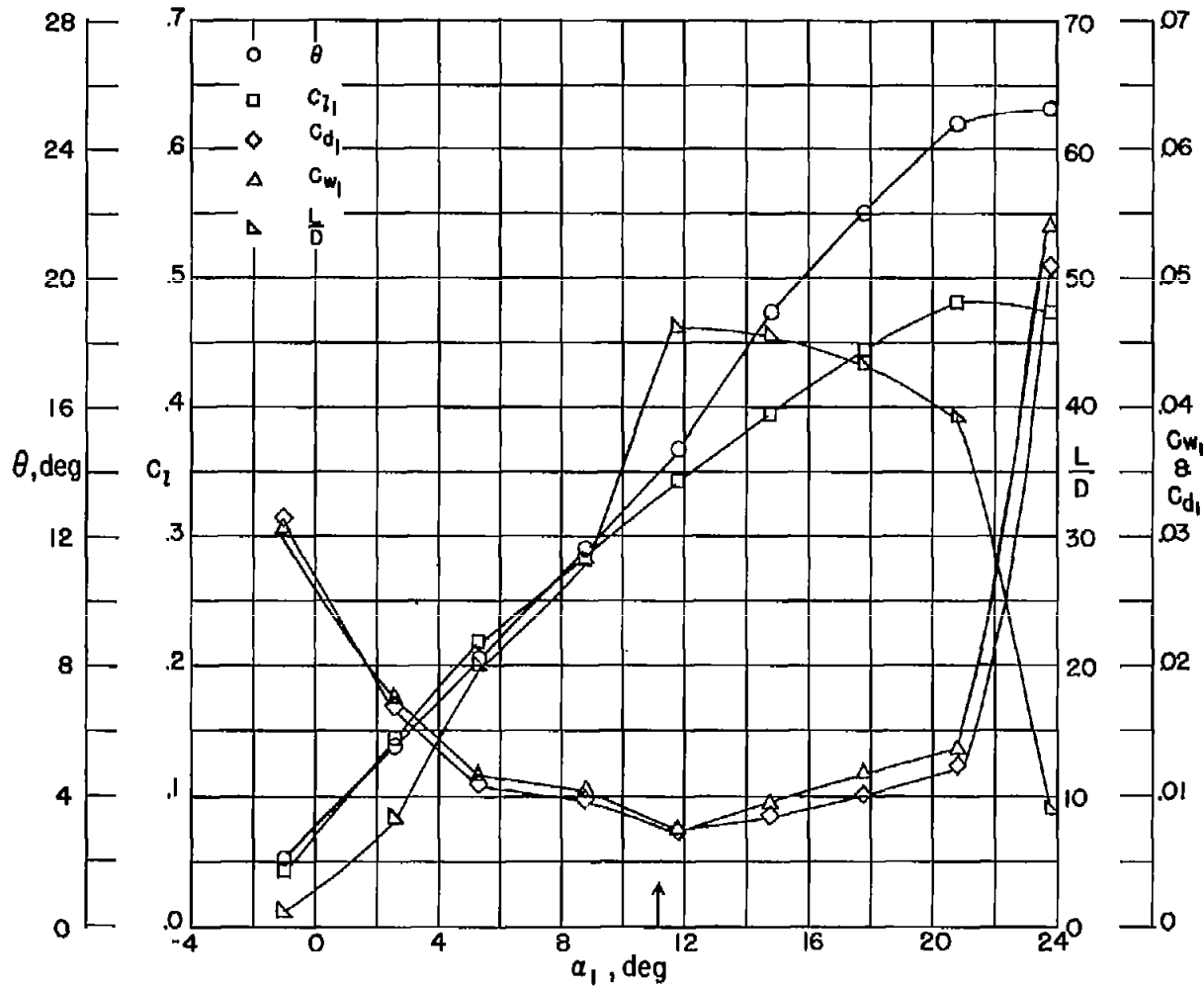


Figure 17.- Blade-surface pressure distributions and section characteristics for the cascade combination $\beta = 45^\circ$; $\sigma = 1.5$; and blade section 63-(6A₄K₆)06.



(g) Section characteristics; arrow shows design angle of attack.

Figure 17.- Concluded.

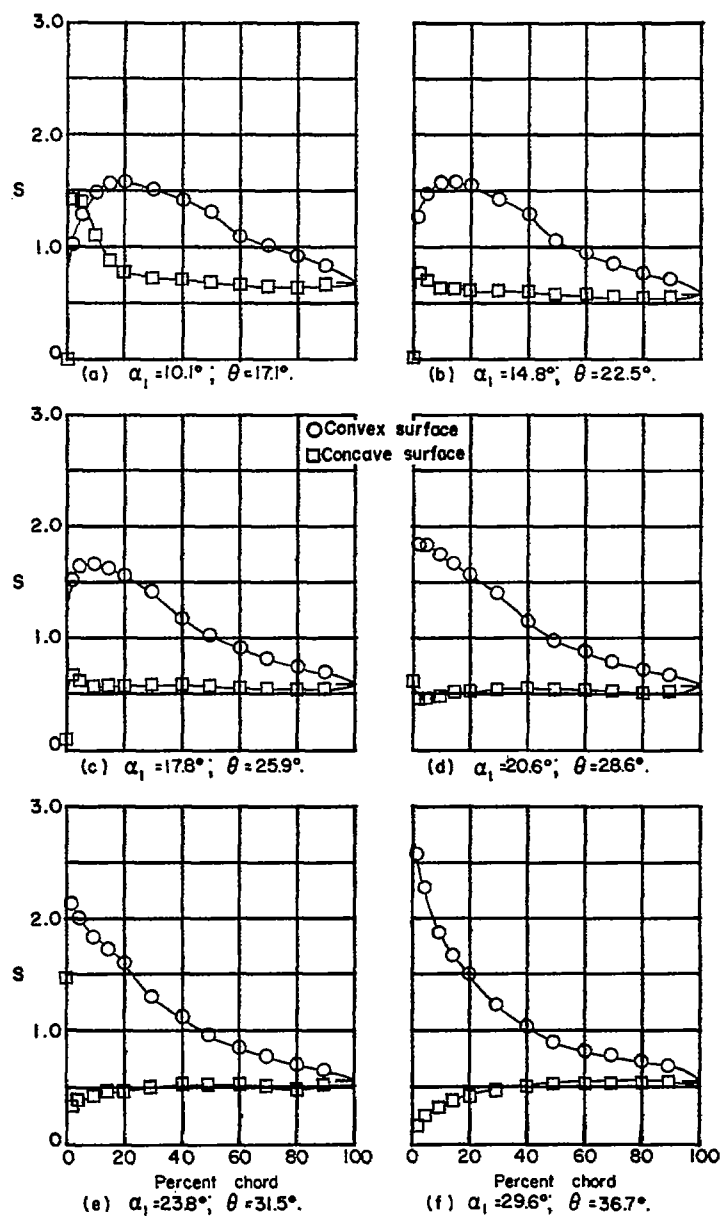
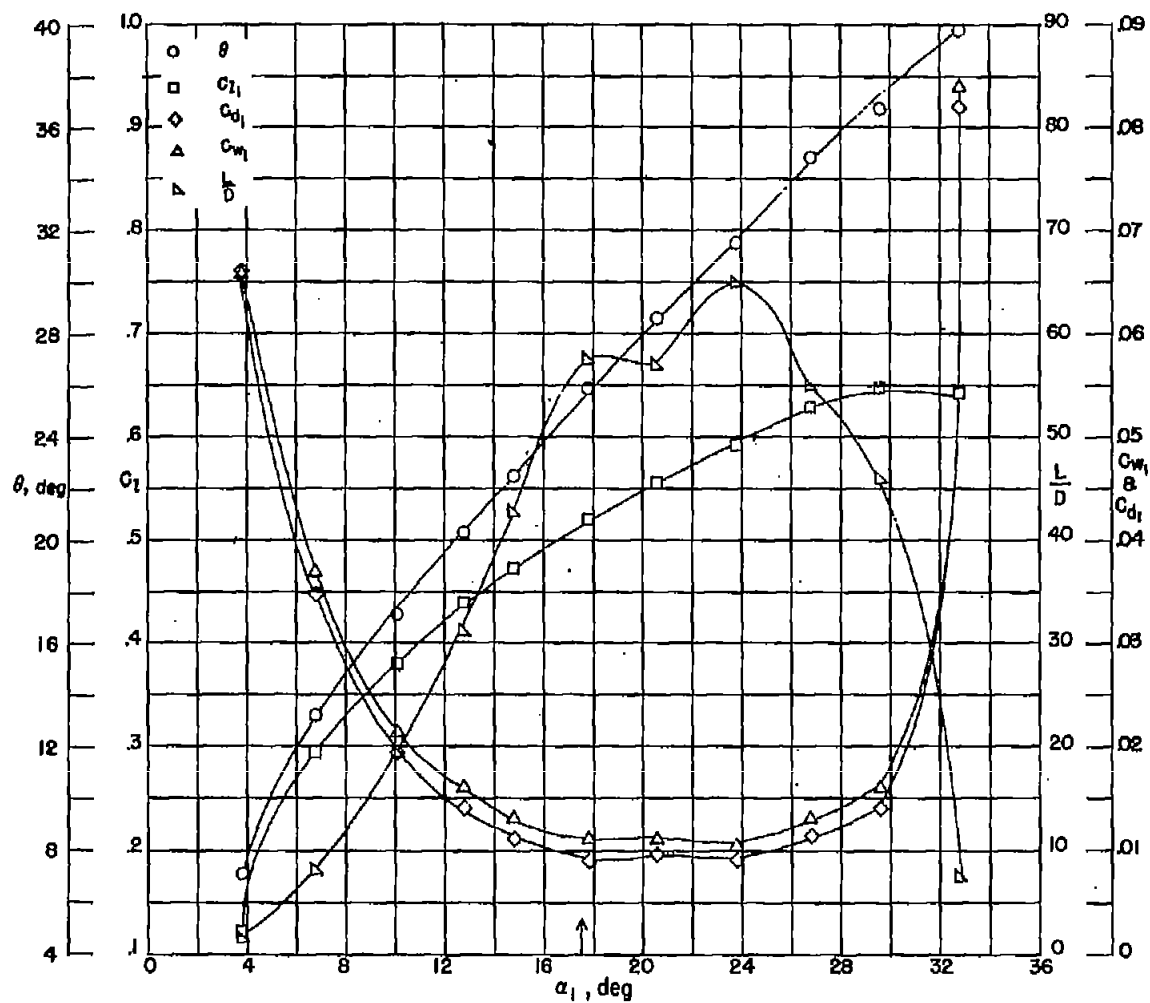


Figure 18.- Blade-surface pressure distributions and section characteristics for the cascade combination $\beta = 45^\circ$; $\sigma = 1.5$; and blade section 63-(12A₄K₆)06.



(g) Section characteristics; arrow shows design angle of attack.

Figure 18.- Concluded.

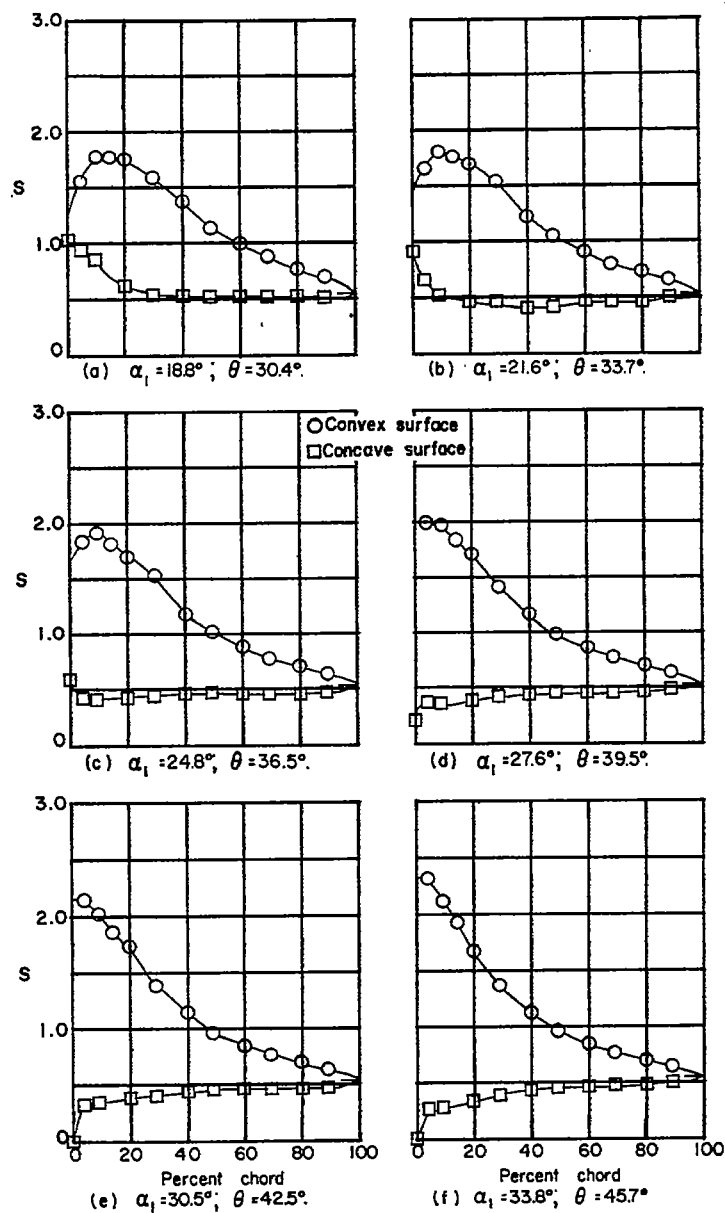
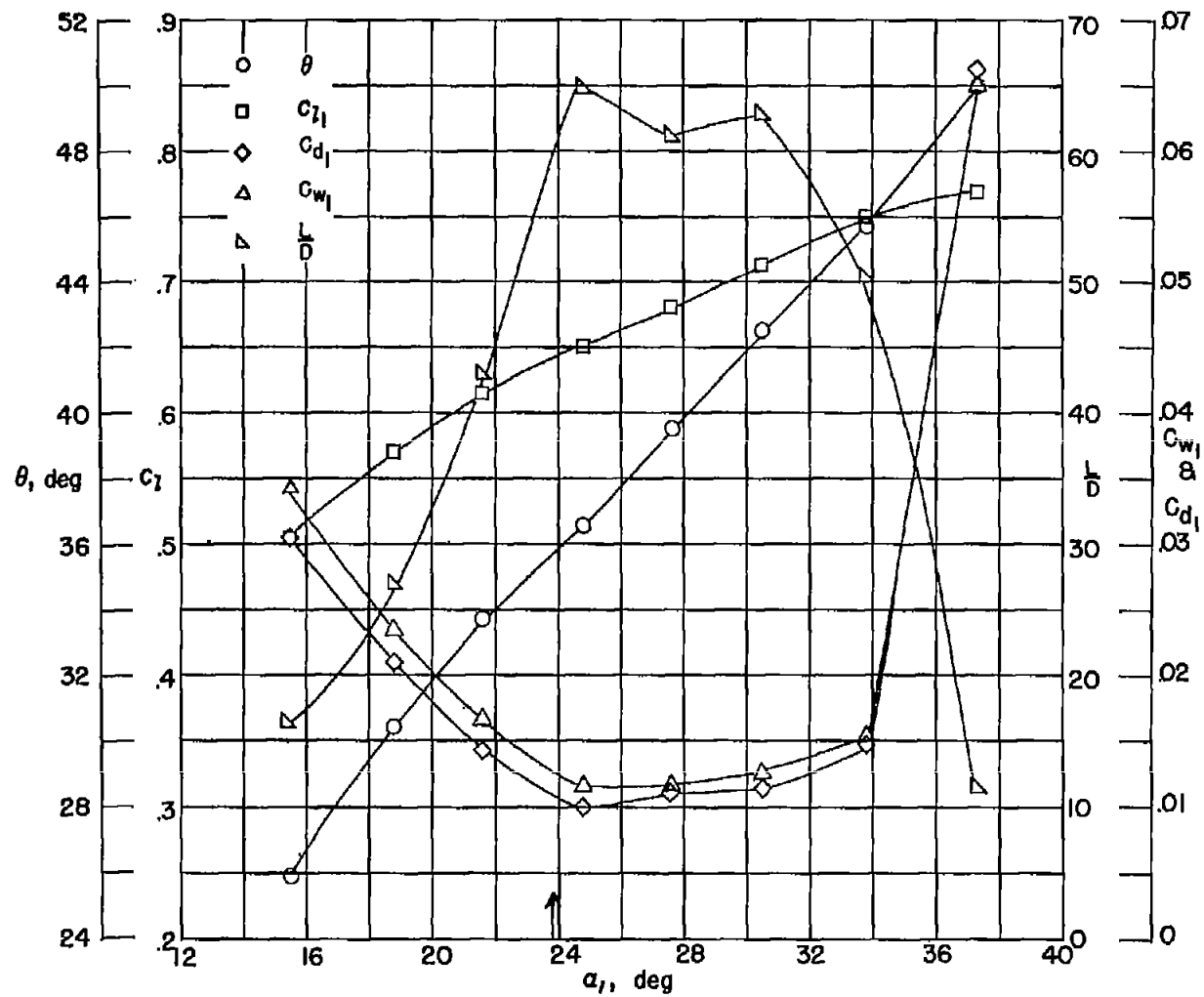


Figure 19.- Blade-surface pressure distributions and section characteristics for the cascade combination $\beta = 45^\circ$; $\sigma = 1.5$; and blade section 63-(18A₄K₆)06.



(g) Section characteristics; arrow shows design angle of attack.

Figure 19.- Concluded.

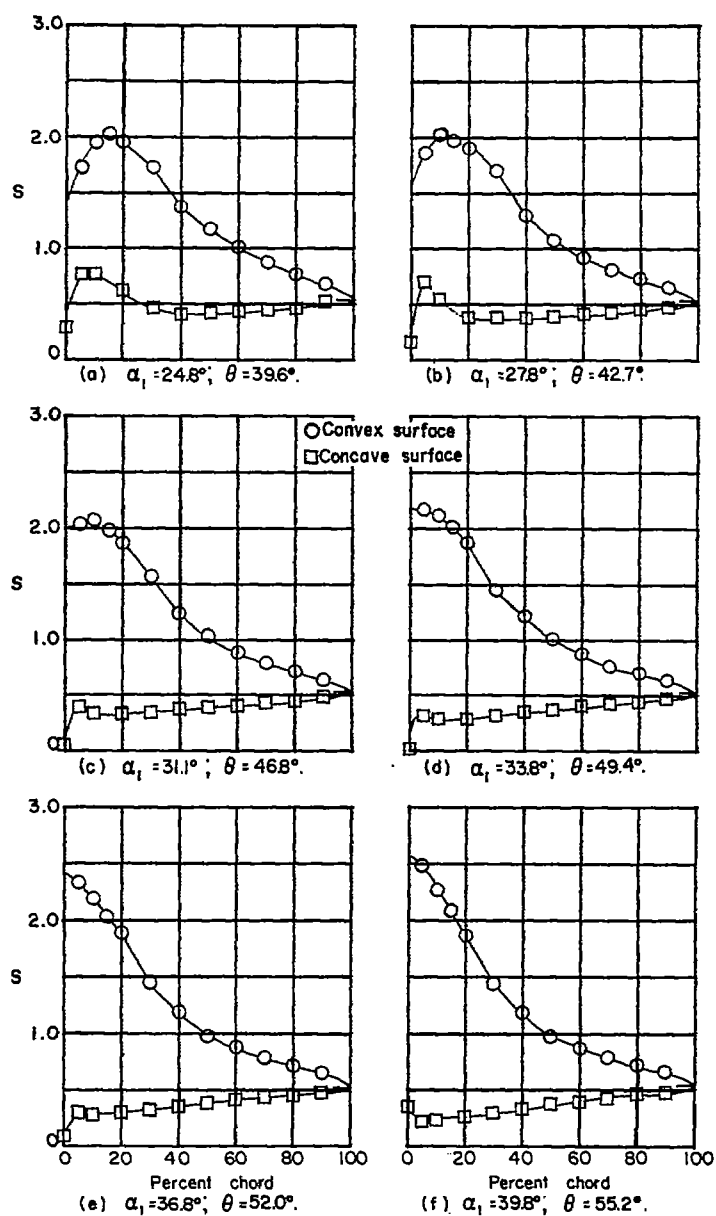
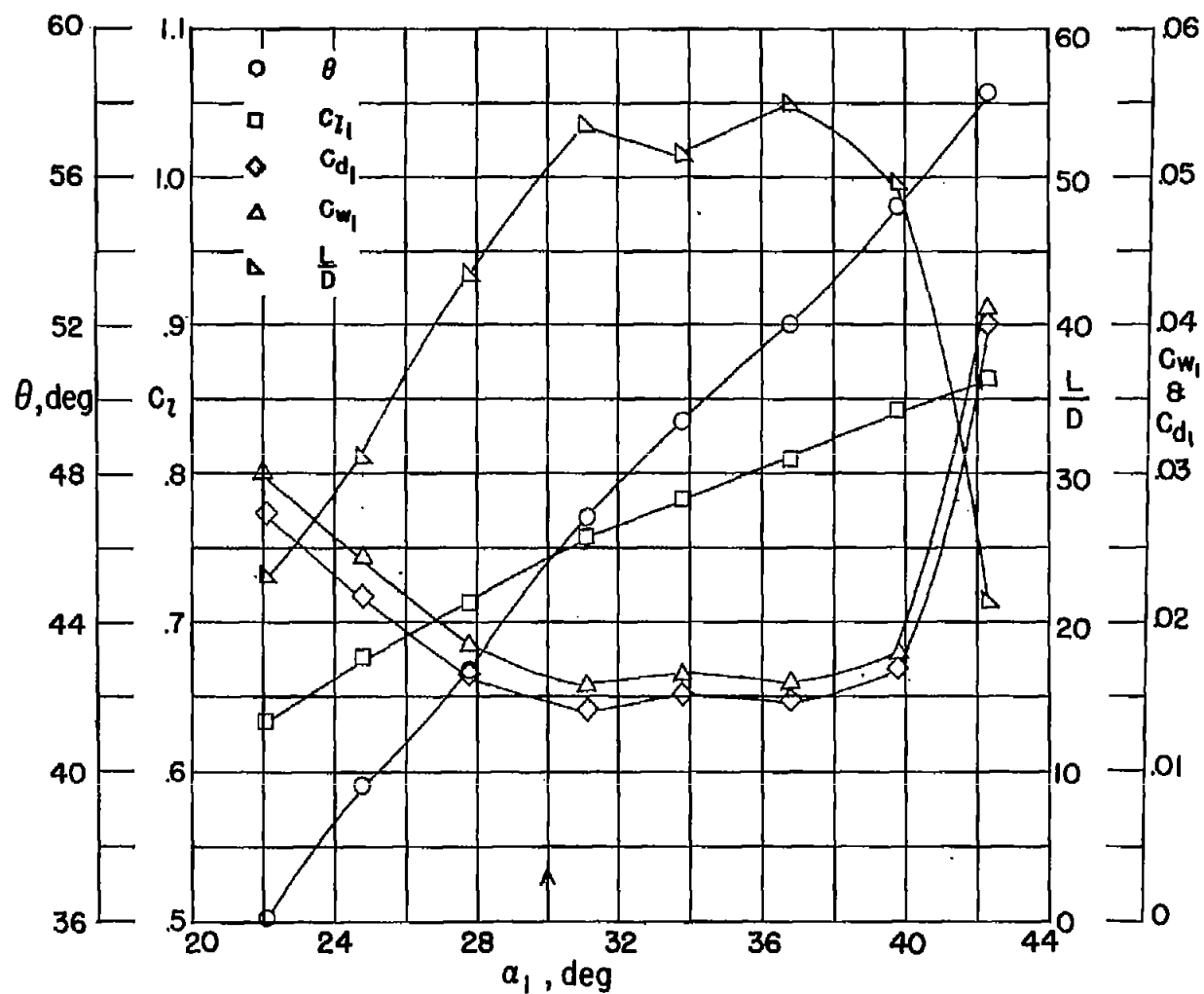


Figure 20.- Blade-surface pressure distributions and section characteristics for the cascade combination $\beta = 45^\circ$; $\sigma = 1.5$; and blade section, 63-(24A4K6)06.



(g) Section characteristics; arrow shows design angle of attack.

Figure 20.- Concluded.

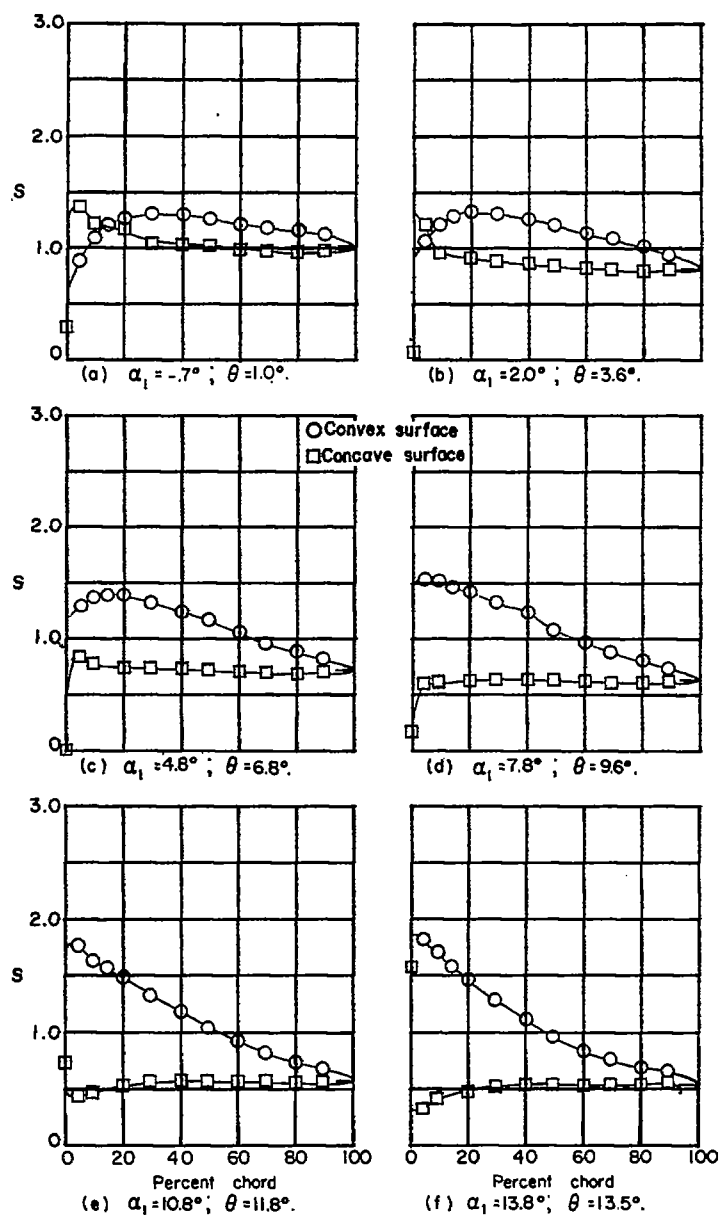
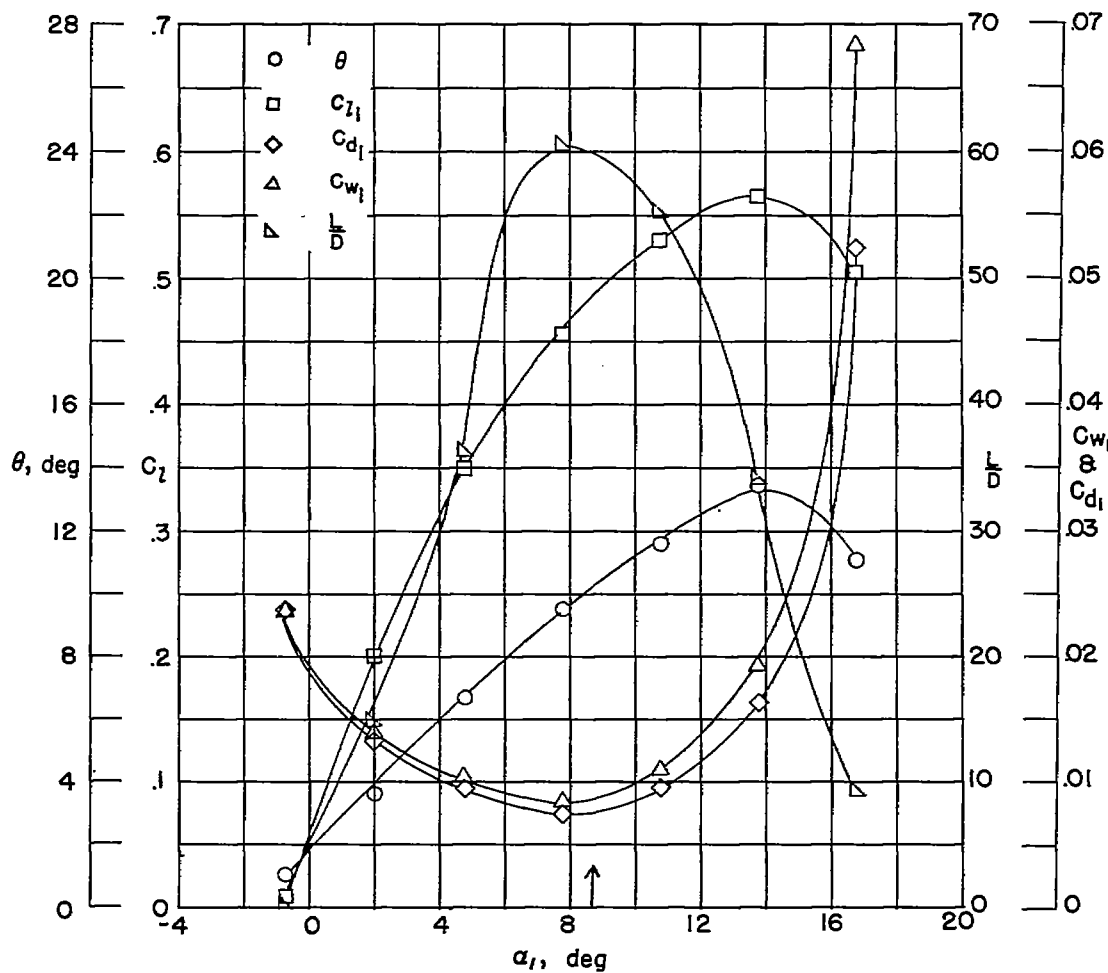


Figure 21.- Blade-surface pressure distributions and section characteristics for the cascade combination $\beta = 60^\circ$; $\sigma = 1.0$; and blade section, 63-(6A₄K₆)06.



(g) Section characteristics; arrow shows design angle of attack.

Figure 21.- Concluded.

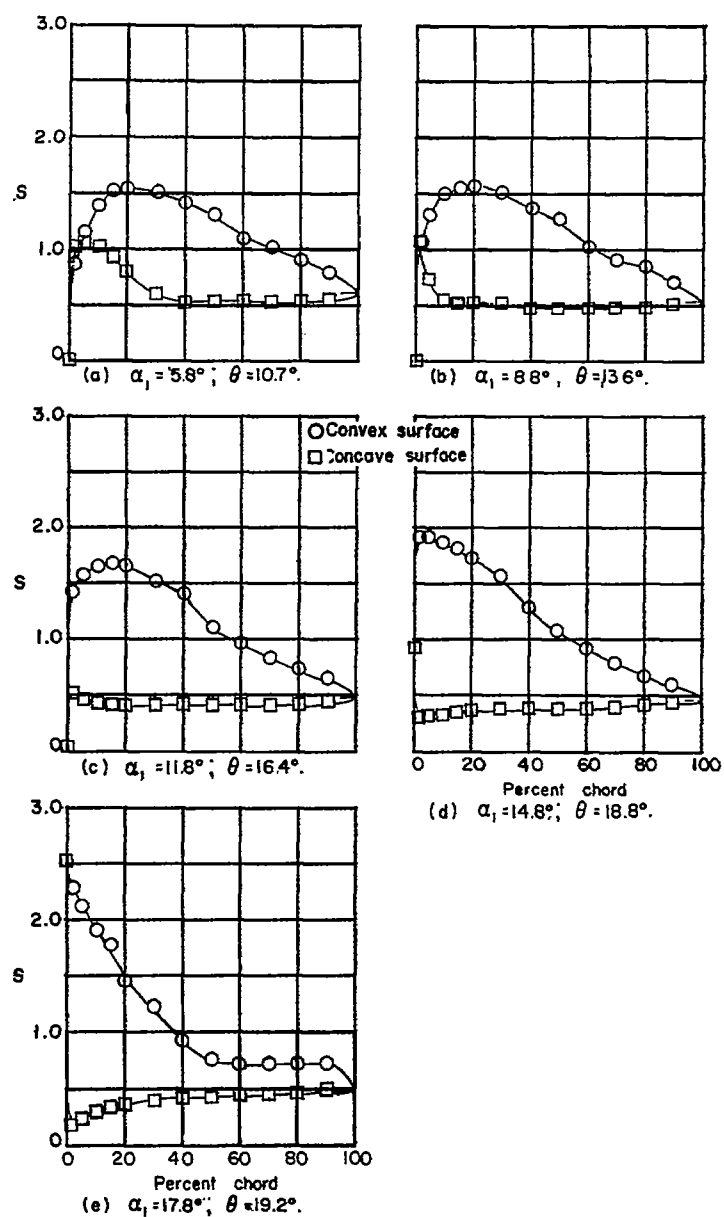
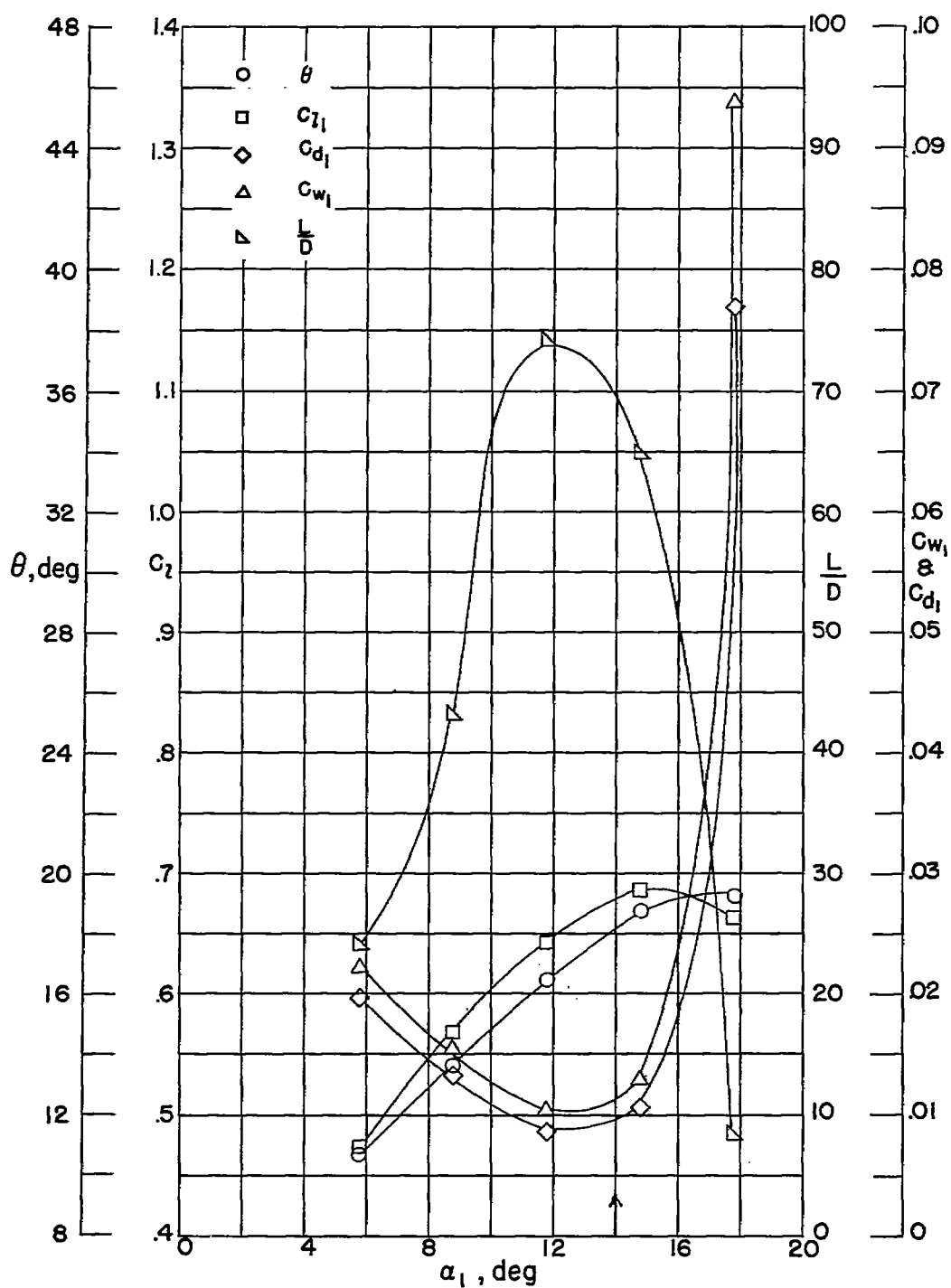


Figure 22.- Blade-surface pressure distributions and section characteristics for the cascade combination $\beta = 60^\circ$; $\sigma = 1.0$; and blade section 63-(12A₄K₆)06.



(f) Section characteristics; arrow shows design angle of attack.

Figure 22.- Concluded.

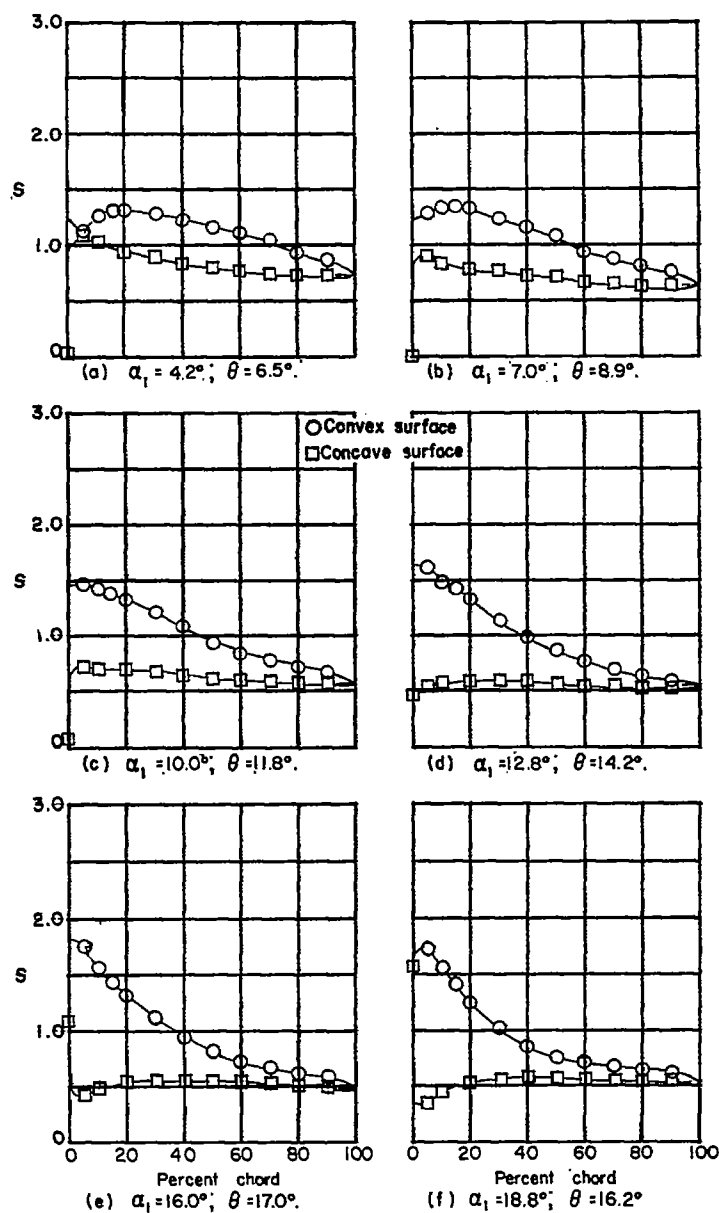
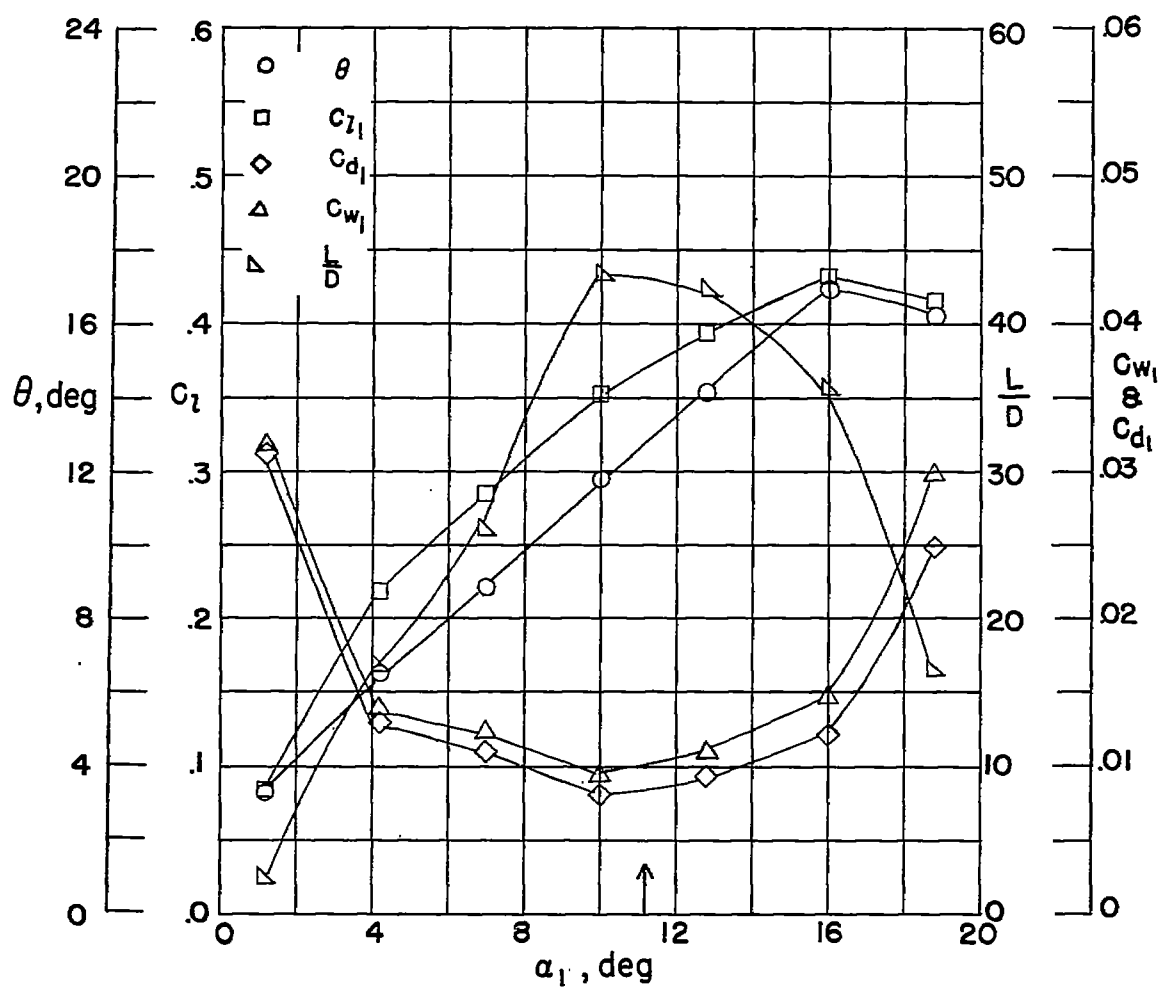


Figure 23.- Blade-surface pressure distributions and section characteristics for the cascade combination $\beta = 60^\circ$; $\sigma = 1.5$; and blade section 63-(6A₄K₆)06.



(g) Section characteristics; arrow shows design angle of attack.

Figure 23.- Concluded.

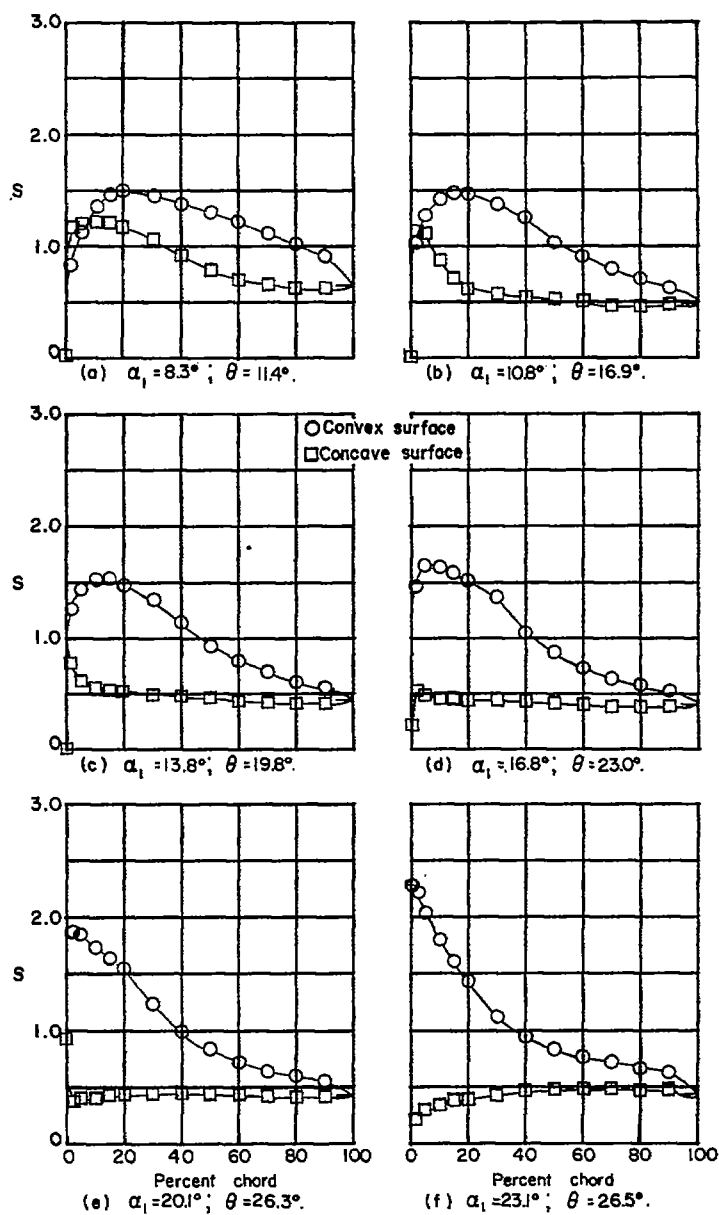
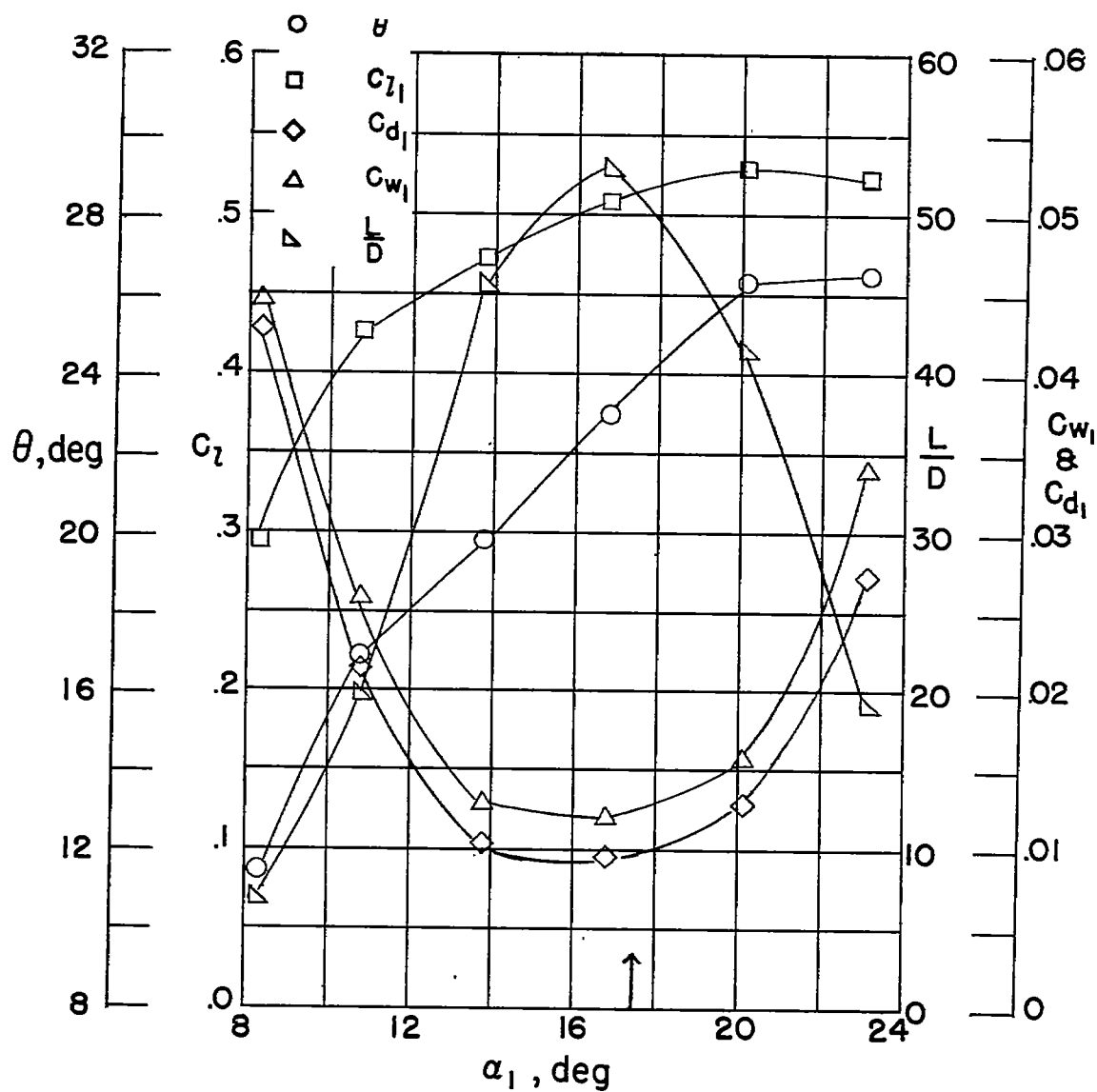


Figure 24.- Blade-surface pressure distributions and section characteristics for the cascade combination $\beta = 60^\circ$; $\sigma = 1.5$; and blade section 63-(12A₄K₆)06.



(g) Section characteristics; arrow shows design angle of attack.

Figure 24.- Concluded.

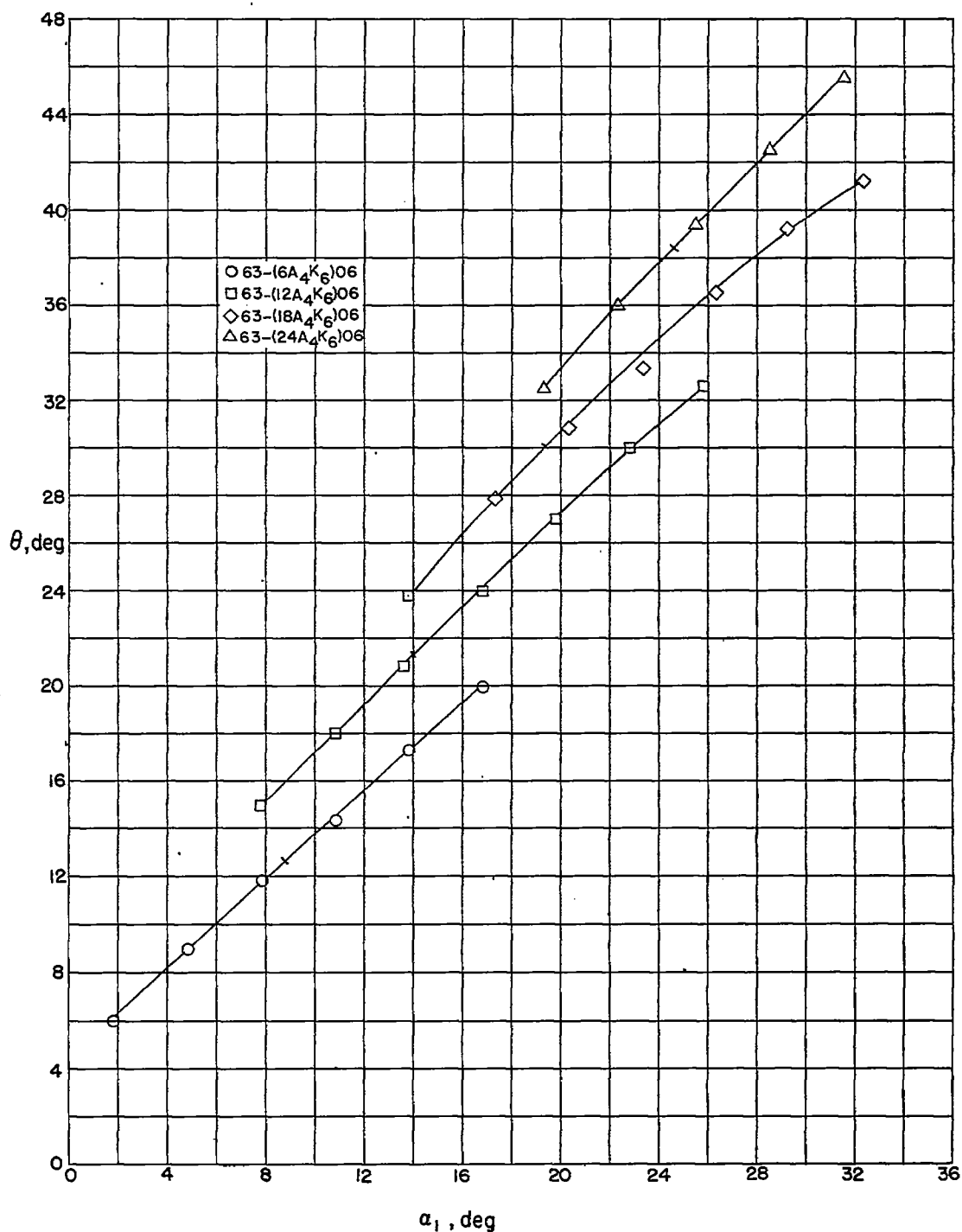


Figure 25.- Summaries of the turning angle, angle-of-attack relationships for the four cambered blade sections tested; $\beta = 30^\circ$; $\sigma = 1.0$. Short bar across curve is design angle of attack.

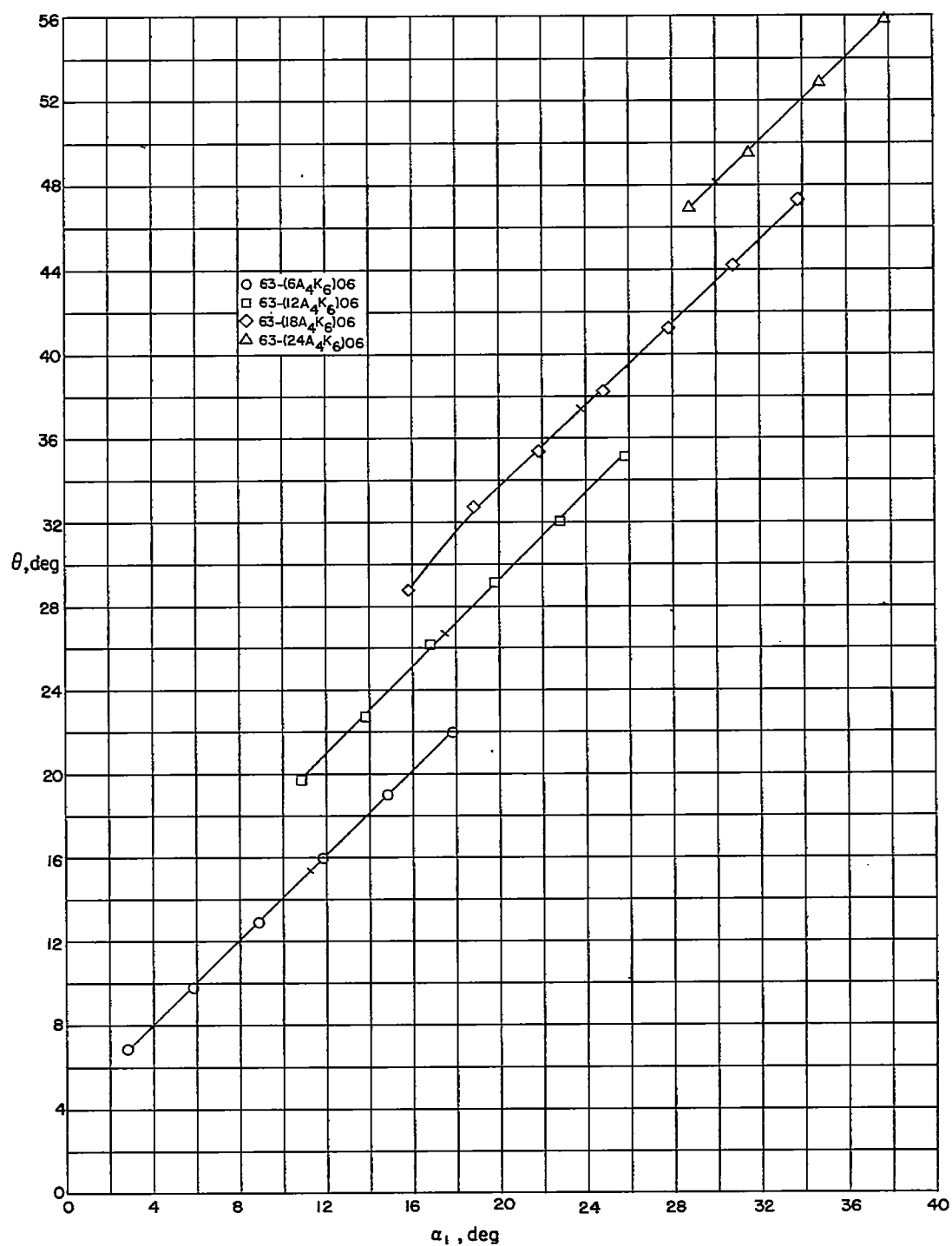


Figure 26.- Summaries of the turning angle, angle-of-attack relationships for the four cambered blade sections tested; $\beta = 30^\circ$; $\sigma = 1.5$. Short bar across curve is design angle of attack.

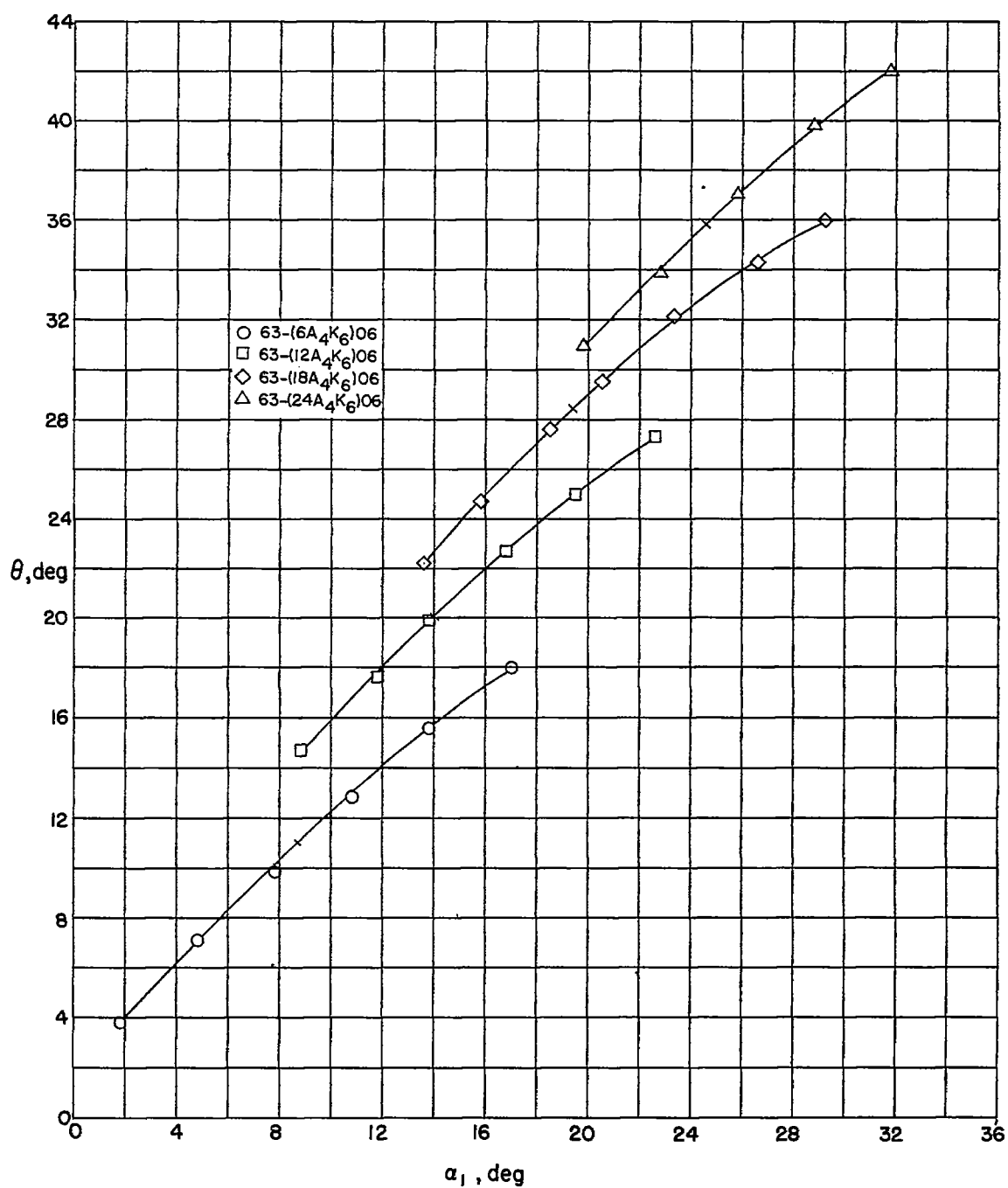


Figure 27.- Summaries of the turning angle, angle-of-attack relationships for the four cambered blade sections tested; $\beta = 45^\circ$; $\sigma = 1.0$. Short bar across curve is design angle of attack.

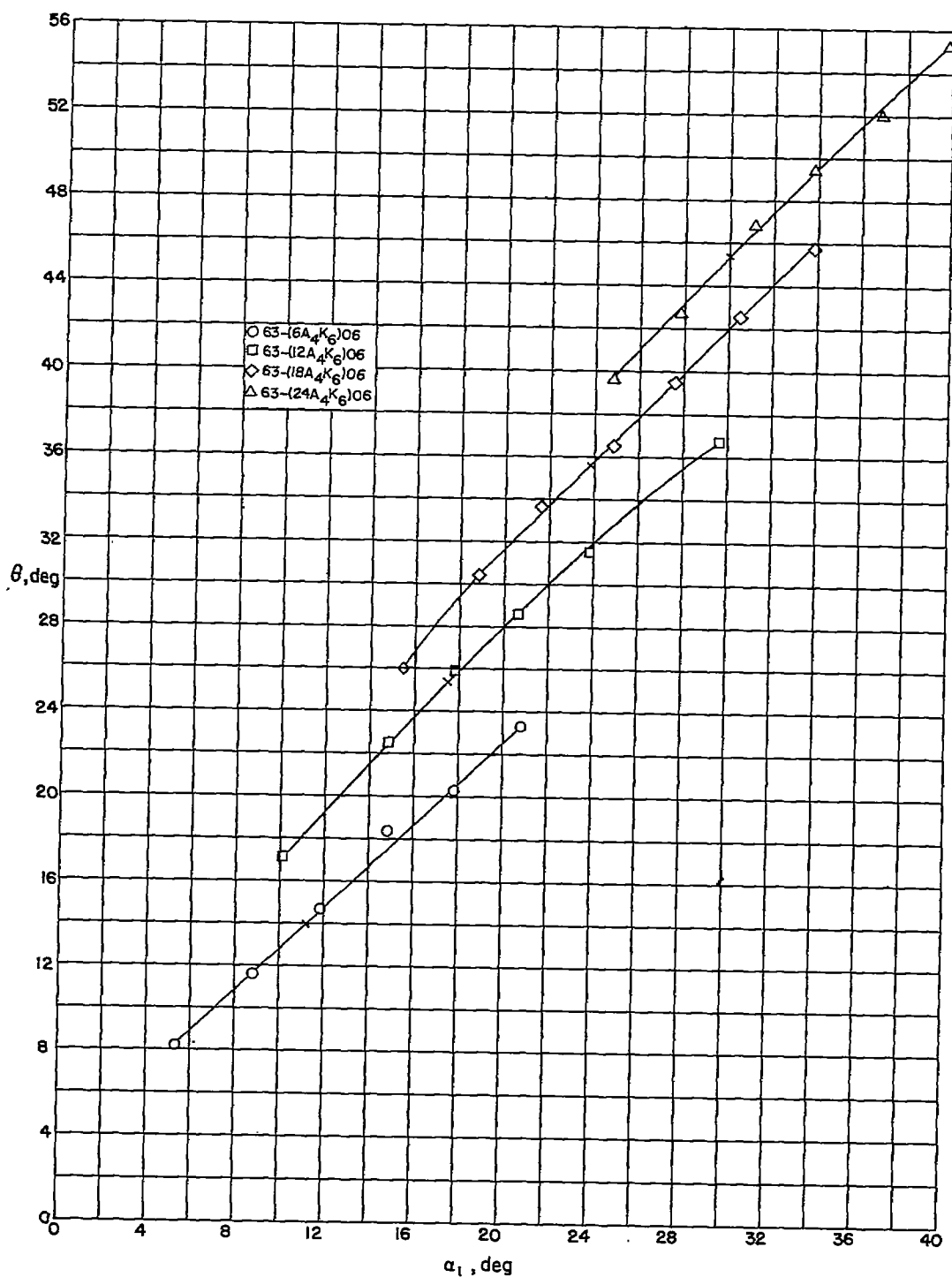


Figure 28.- Summaries of the turning angle, angle-of-attack relationships for the four cambered blade sections tested; $\beta = 45^\circ$; $\sigma = 1.5$. Short bar across curve is design angle of attack.

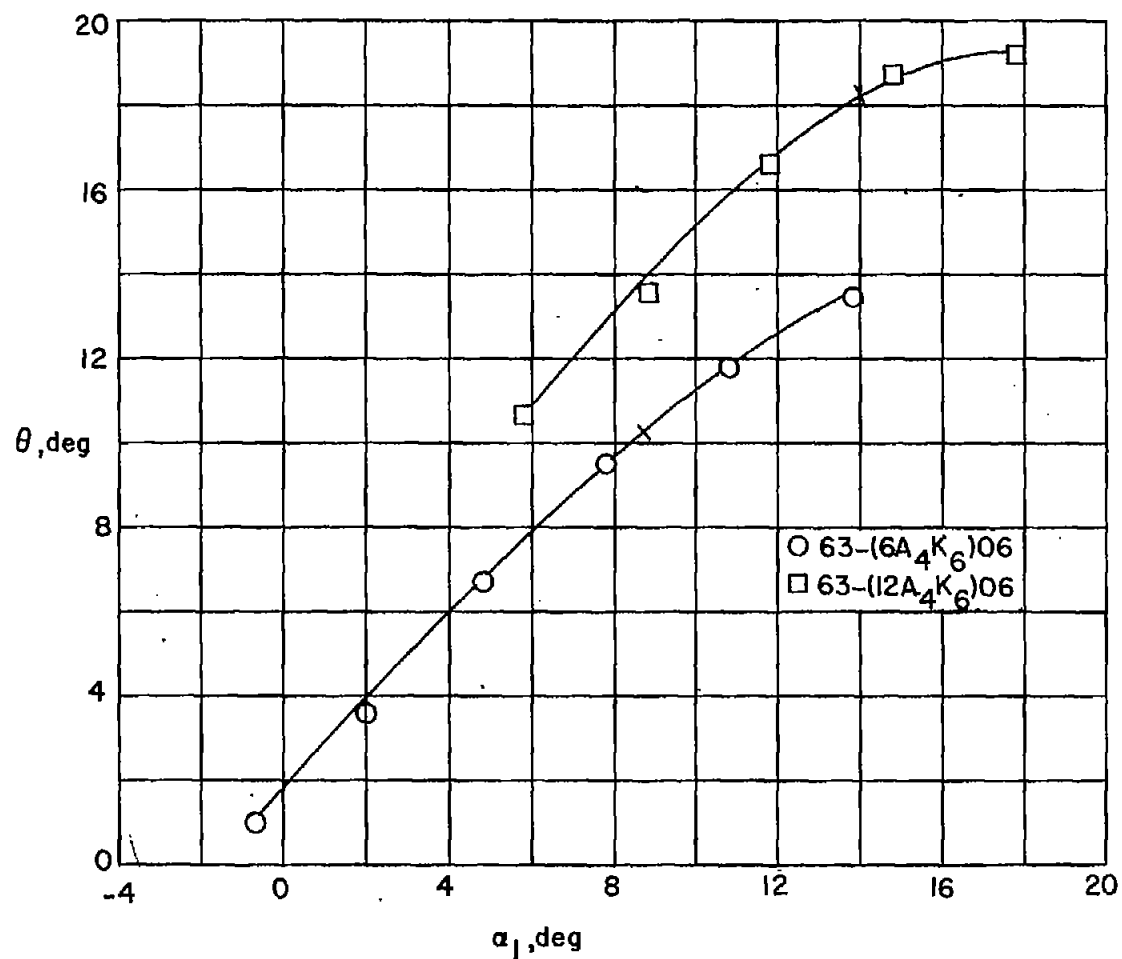


Figure 29.- Summaries of the turning angle, angle-of-attack relationships for two cambered blade sections; $\beta = 60^\circ$; $\sigma = 1.0$. Short bar across curve is design angle of attack.

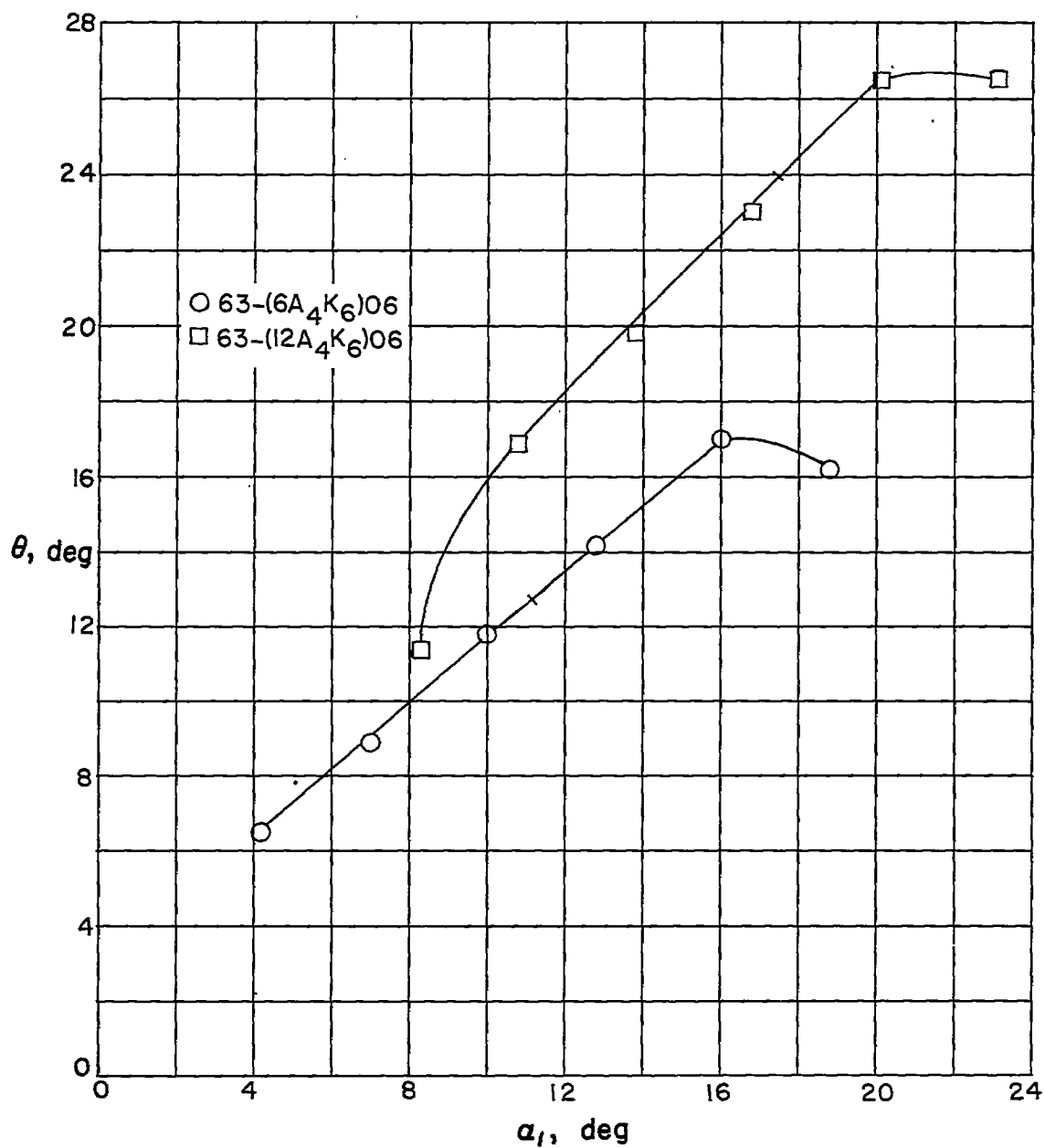


Figure 30.- Summaries of the turning angle, angle-of-attack relationships for two cambered blade sections; $\beta = 60^\circ$; $\sigma = 1.5$. Short bar across curve is design angle of attack.

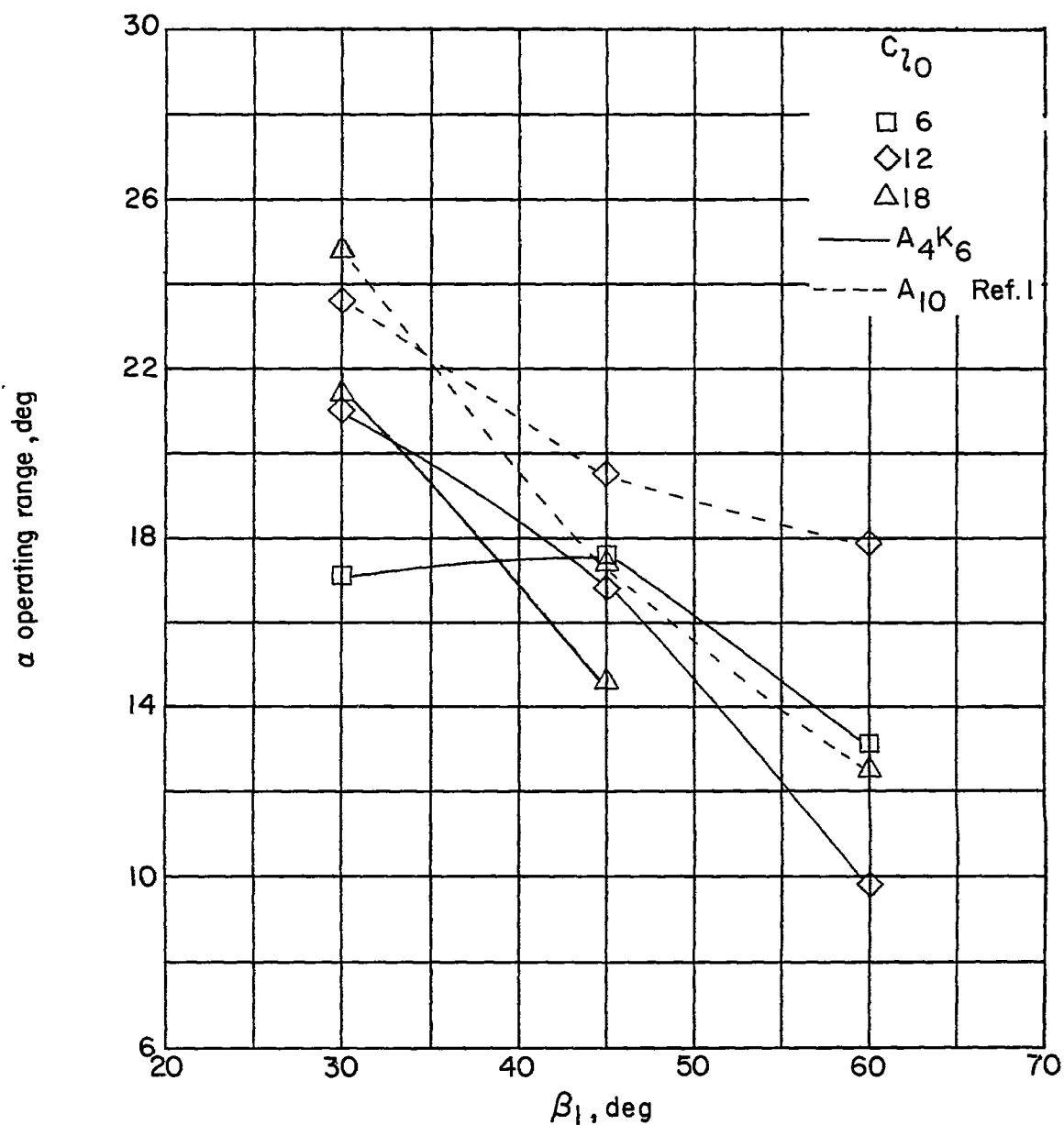


Figure 31.- Variation of the estimated operating angle-of-attack range with inlet-air angle for several cambers; $\sigma = 1.0$.

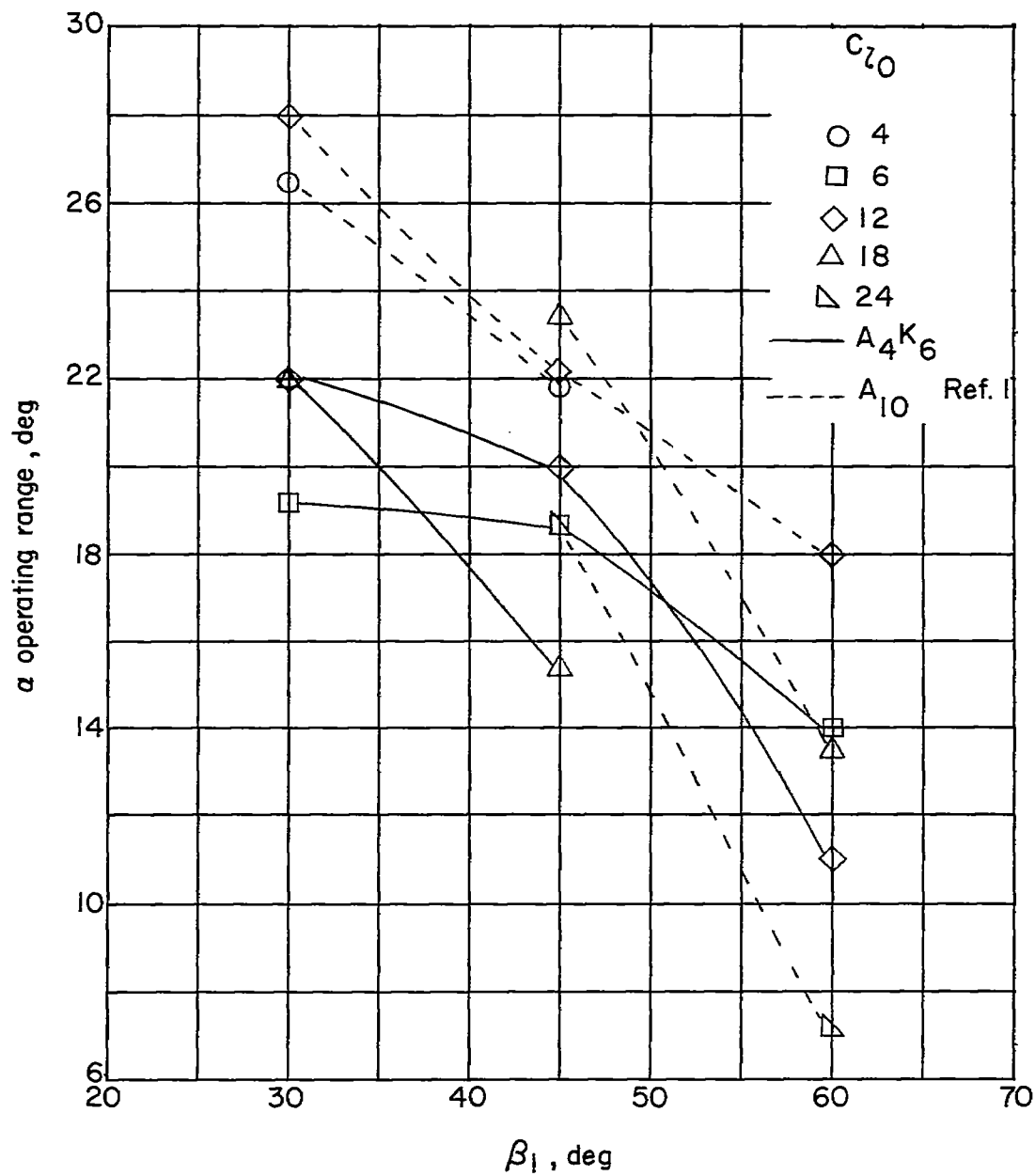


Figure 32.- Variation of the estimated operating angle-of-attack range with inlet-air angle for several cambers; $\sigma = 1.5$.

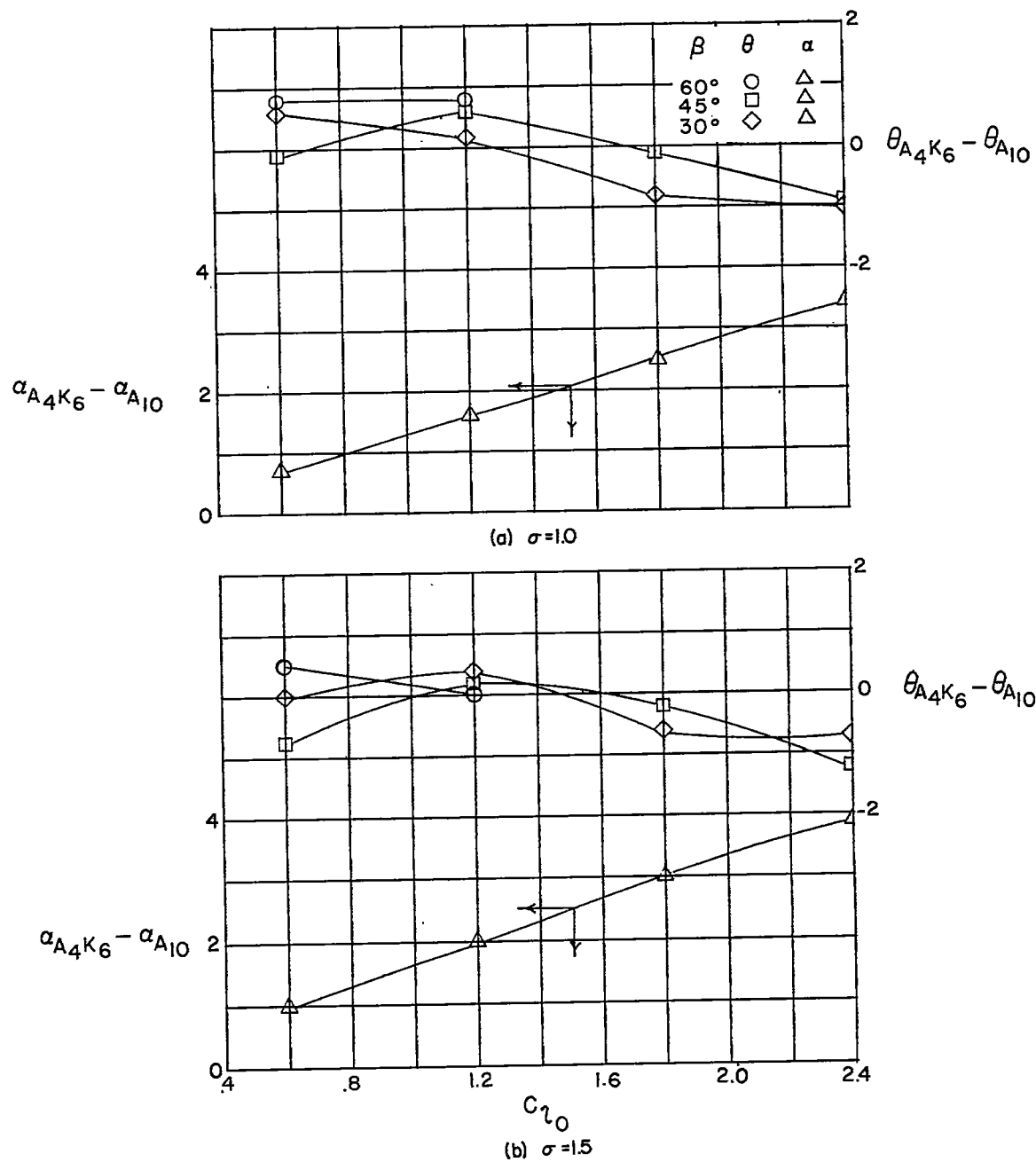


Figure 33.- Difference in design α and θ for the 63-($C_{10}A_{4K6}$)06 and 65-($C_{10}A_{10}$)10 blade sections.

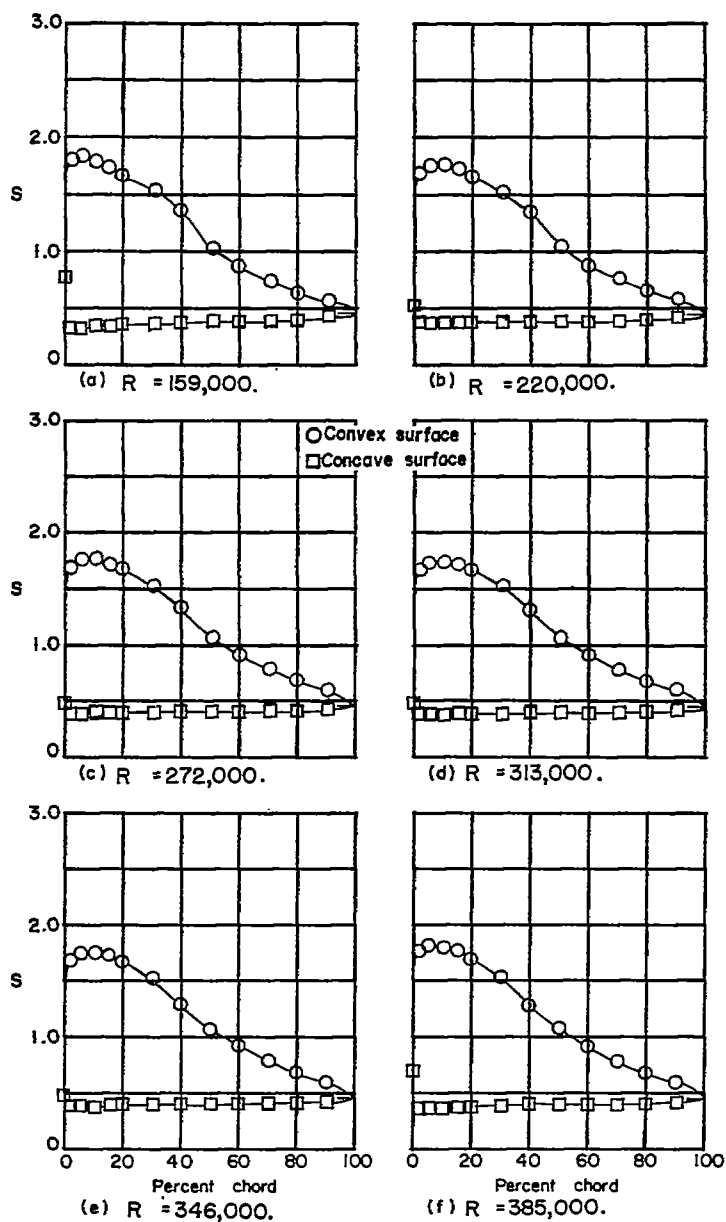


Figure 34.- Blade-surface pressure distributions at various Reynolds numbers for the cascade combination $\beta = 45^\circ$; $\sigma = 1.5$; and blade section 63-(12A₄K₆)06; $\alpha = 17.8^\circ$.

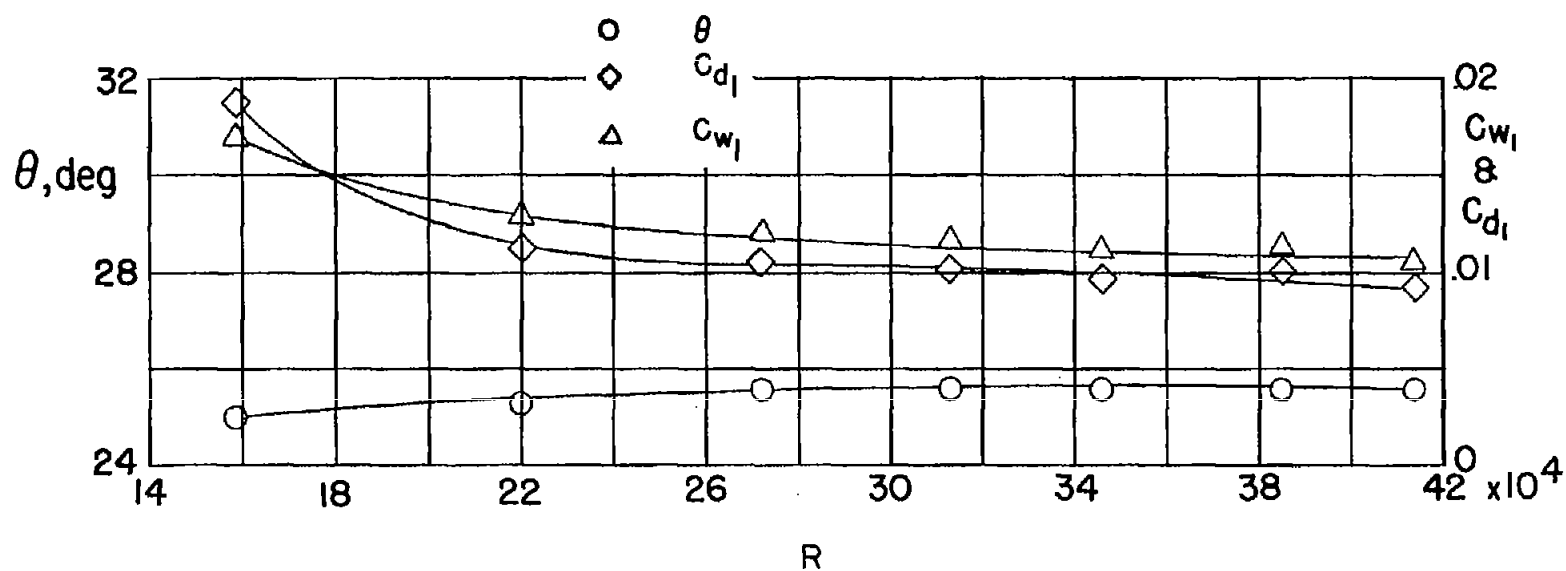


Figure 35.- Variation of section characteristics of the 63-(12A₄K₆)06 profiles with Reynolds number; $\beta = 45^\circ$; $\sigma = 1.5$; $\alpha = 17.8$.

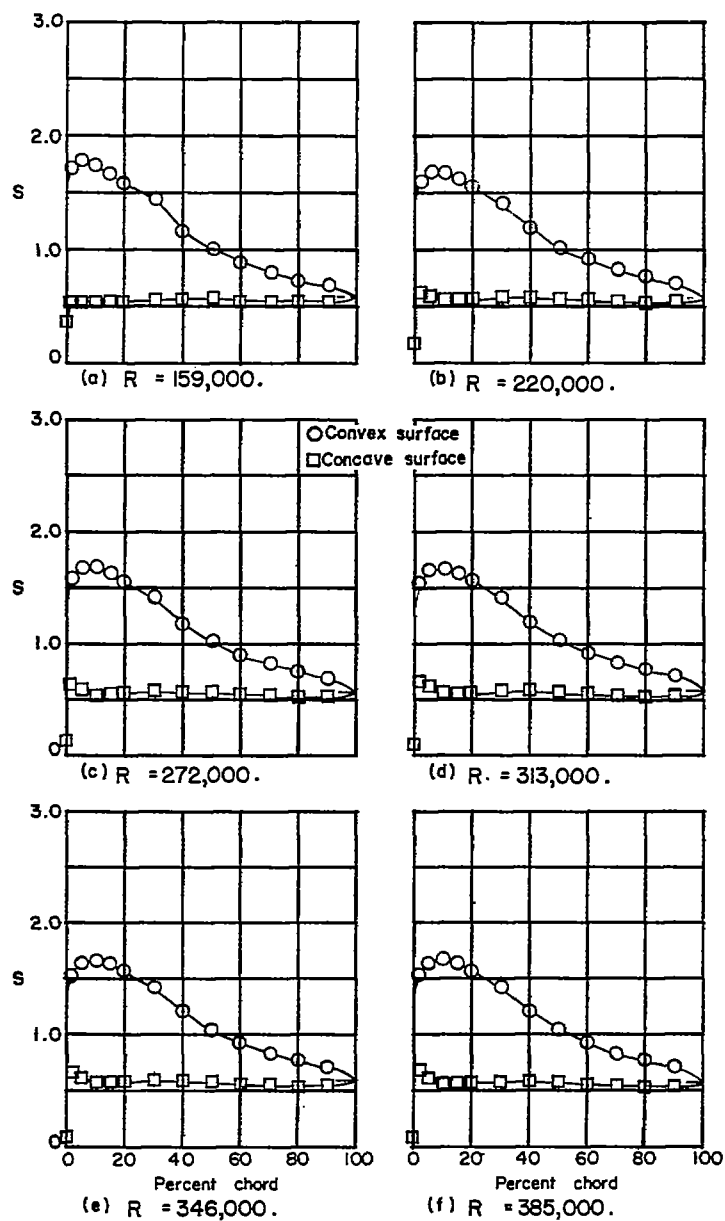


Figure 36.- Blade-surface pressure distributions at various Reynolds numbers for the cascade combination $\beta = 60^\circ$; $\sigma = 1.0$; and blade section 63-(12A₄K₆)06; $\alpha = 14.0$.

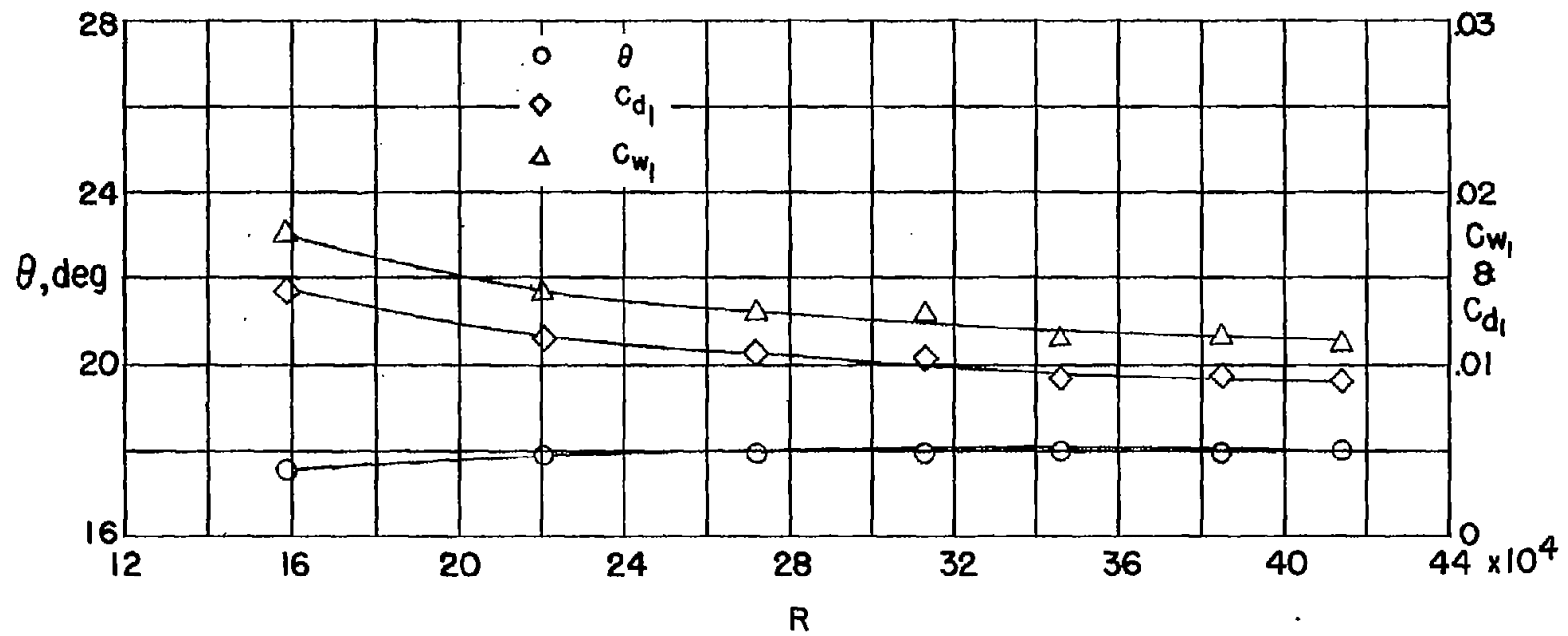


Figure 37.- Variation of section characteristics of the 63-(12A₄K₆)06 profiles with Reynolds number; $\beta = 60^\circ$; $\sigma = 1.0$; $\alpha = 14^\circ$.

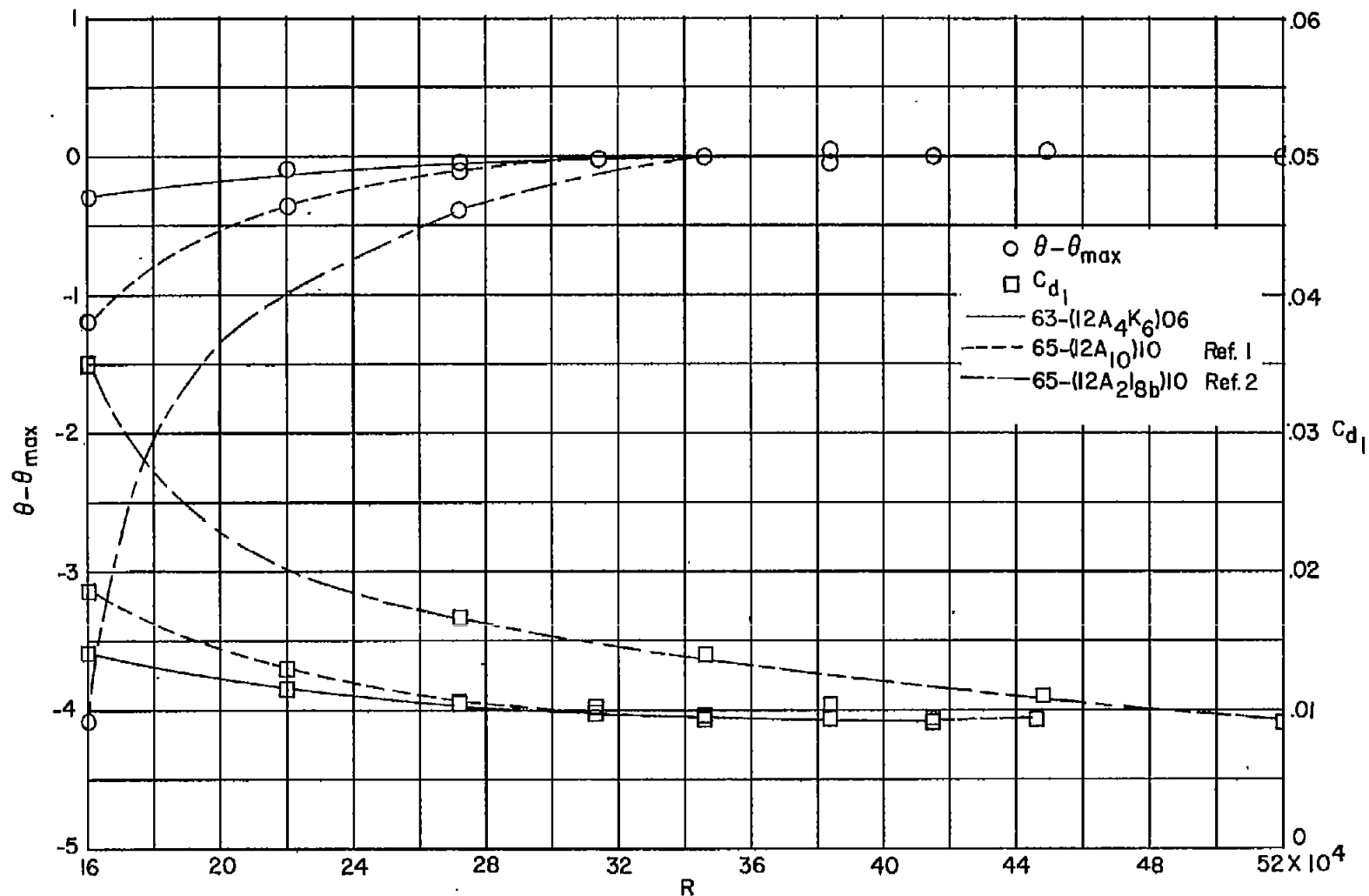


Figure 38.- Variation of $\theta - \theta_{\max}$ and C_{d1} with Reynolds number at $\alpha_d; \beta = 60^\circ; \sigma = 1.0$.

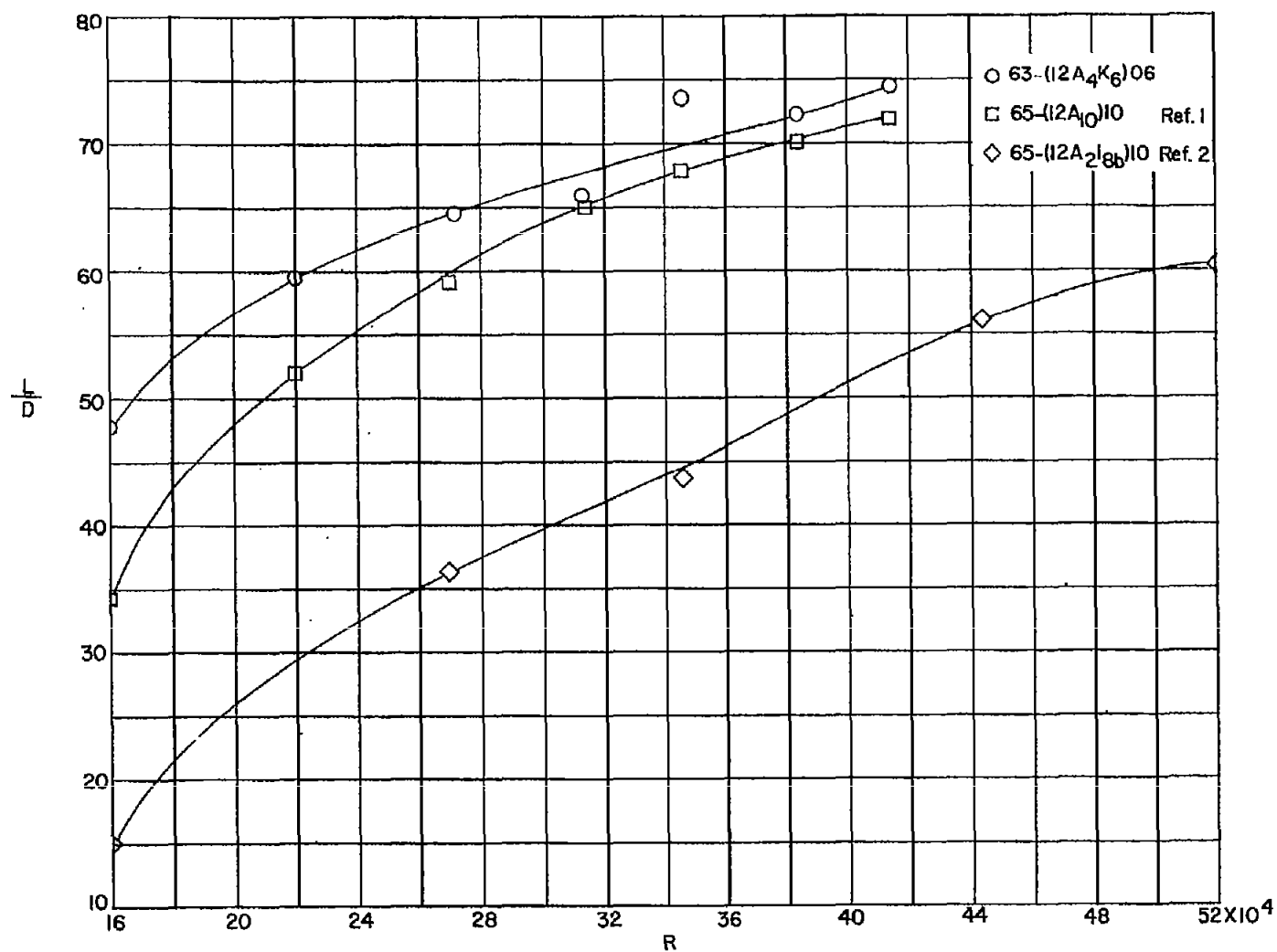


Figure 39.- Variation of L/D with Reynolds number at $\alpha_d; \beta = 60^\circ; \sigma = 1.0$.

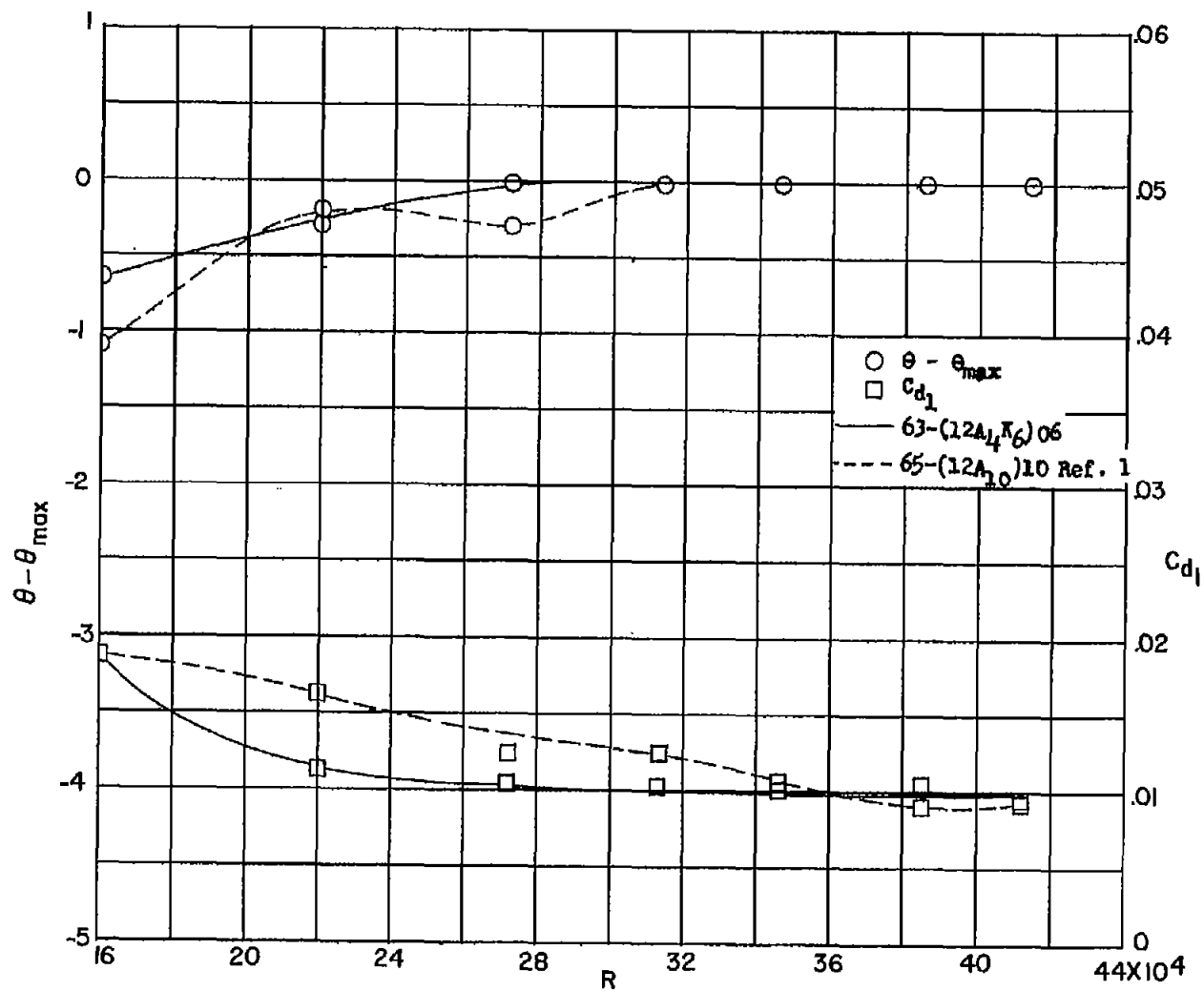


Figure 40.- Variation of $\theta - \theta_{max}$ and C_{d1} with Reynolds number at $\alpha_d; \beta = 45^\circ; \sigma = 1.5$.

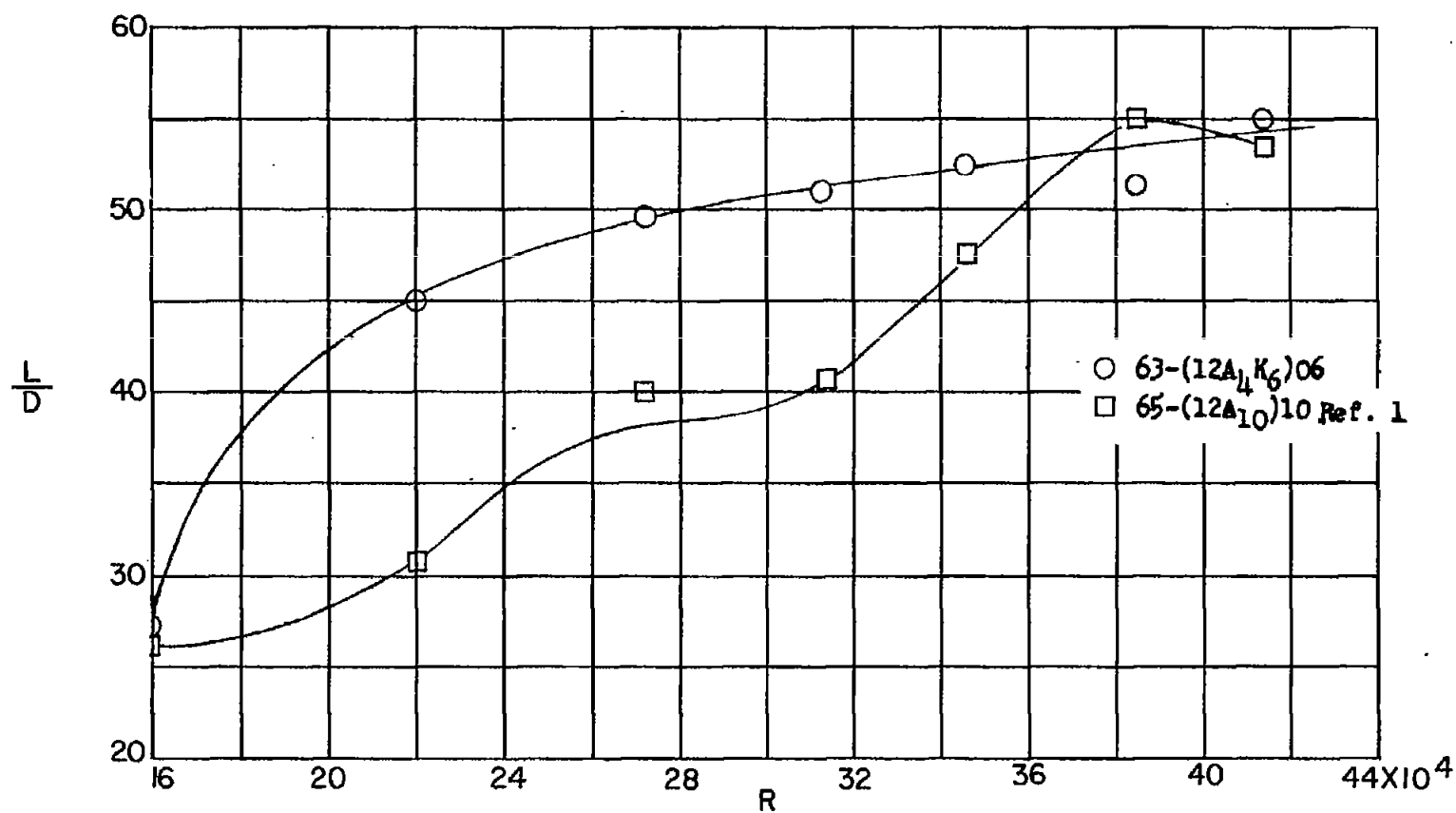


Figure 41.- Variation of L/D with Reynolds number at $\alpha_d; \beta = 45^\circ; \sigma = 1.5$.

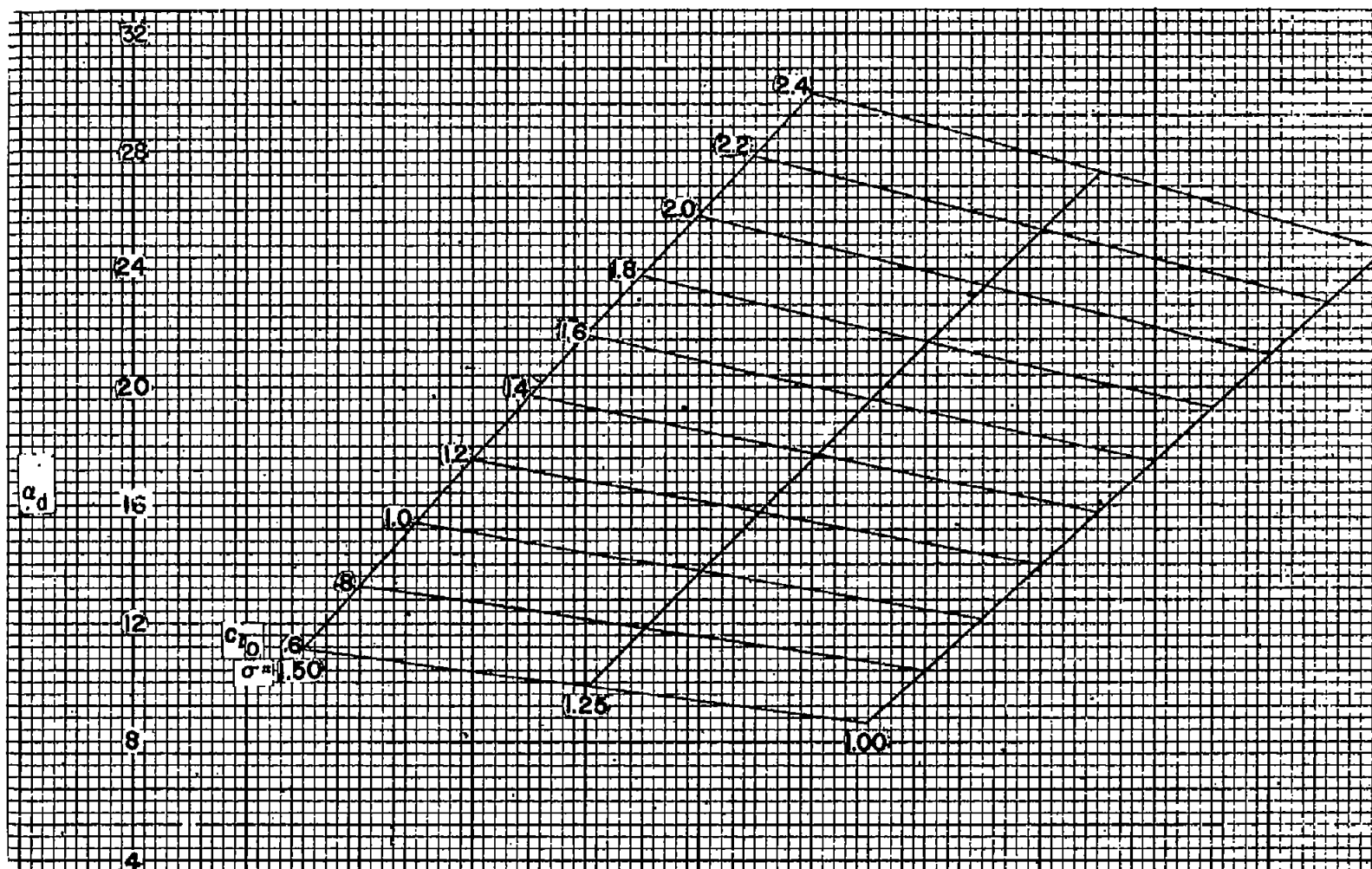


Figure 42.- Design angle-of-attack carpet plot for the NACA 63-(C₁₀A₄K₆)06 compressor-blade sections.

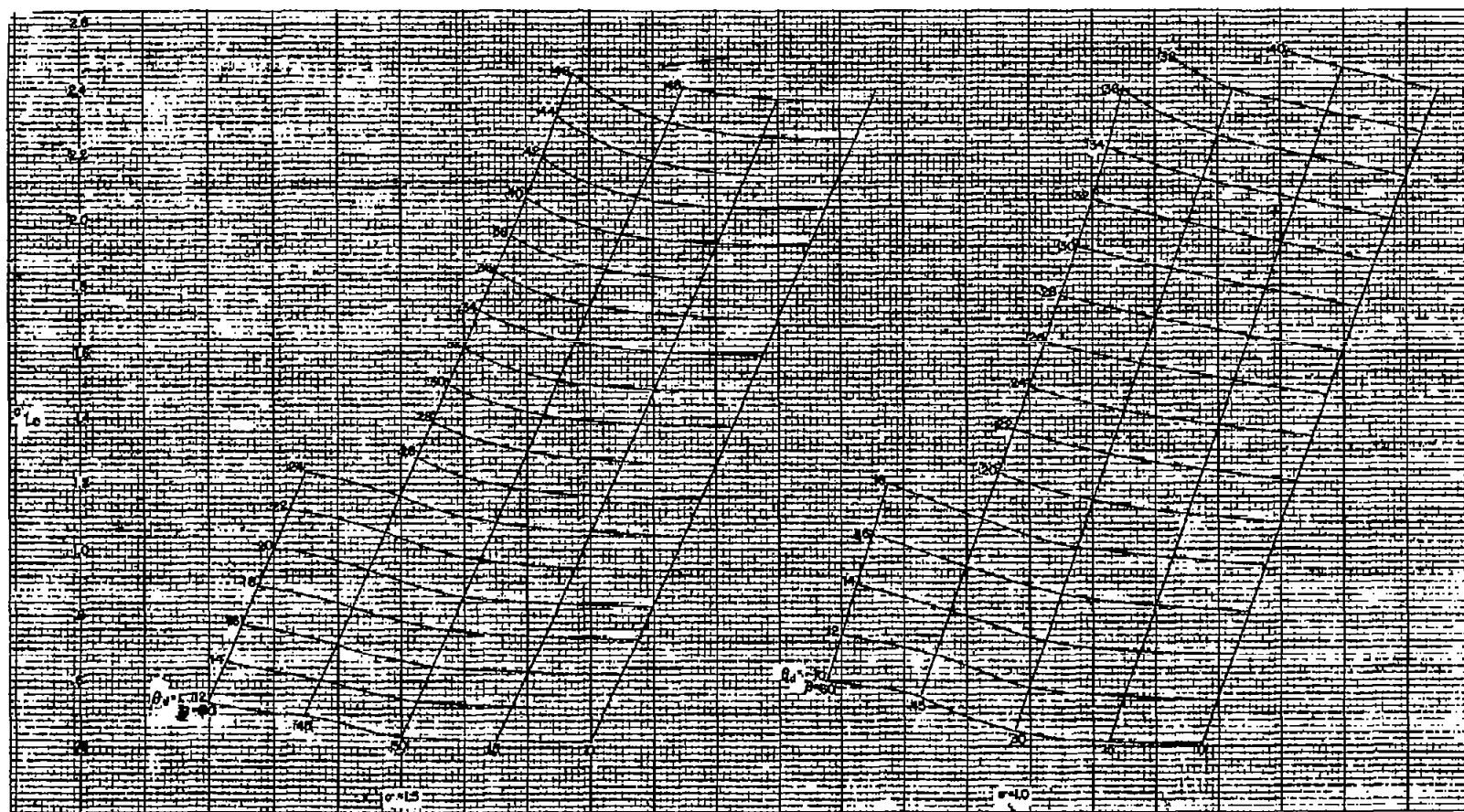


Figure 43.- Design turning-angle carpet plot for the NACA 63-(C₁₀A₁K₆)06 compressor-blade sections.